UNIVERSIDAD
NACIONAL
DE COLOMBIA

Catalizadores de Ni-Ce inmovilizados en monolitos de cordierita para el reformado seco de metano

María Alejandra Osorio Zabala

Universidad Nacional de Colombia
Facultad de Ciencias, Departamento de Química
Bogotá, Colombia

2023

Catalizadores de Ni-Ce inmovilizados en monolitos de cordierita para el reformado seco de metano

María Alejandra Osorio Zabala

Tesis presentada como requisito parcial para optar al título de:

Magister en Ciencias - Química

Director (a):

Carlos Enrique Daza Velásquez, Ph.D.

Línea de Investigación:

Catalizadores para el proceso de reformado de metano

Grupo de Investigación:

Estado Sólido y Catálisis ambiental

Universidad Nacional de Colombia

Facultad de Ciencias, Departamento de Química

Bogotá, Colombia

2023

Resumen

En esta tesis de maestría, catalizadores de Ni-Mg-Al promovidos con Ce (1-6%) tipo óxido mixto inmovilizados y en polvo se obtuvieron mediante el método de coprecipitación y recubrimiento en suspensión con precursores de hidrotalcita. Se estudió el comportamiento de los materiales en el reformado en seco de metano, teniendo en cuenta el papel promotor del Ce y el efecto de inmovilizar los óxidos mixtos en monolitos de cordierita. Los catalizadores se caracterizaron por diversas técnicas analíticas para evaluar su composición química, propiedades térmicas, estructurales, reductivas, básicas y morfológicas. La evaluación catalítica se estudió mediante varias pruebas de estabilidad durante 8h a 700 °C (para catalizadores no reducidos) y a 600 °C (para catalizadores previamente reducidos) con WHSV de 94,680 y 23.670 $mL \cdot g_{Cat}^{-1} \cdot h^{-1}$.

Los resultados mostraron que el aumento en el contenido de Ce influye en la formación de tamaños de cristalitos de Ni más pequeños, promueve la reducción de Ni, aumenta la capacidad de captura de CO_2 a altas temperaturas y favorece la formación de partículas de menor tamaño de Ni0. A su vez, la inmovilización de los óxidos mixtos no significó un cambio en la estructura cristalina de los monolitos de cordierita; y se obtuvo la formación de una capa de óxidos mixtos sobre la superficie de los monolitos, con un espesor promedio de 6,13 μm para monolitos con ~ 25 mg de óxido mixto inmovilizad y un espesor de capa promedio de 9,87 μm para monolitos con ~ 100 mg de óxido mixto inmovilizado.

Los resultados de la evaluación catalítica mostraron que el Ce no influye en la actividad, pero sí mejora la estabilidad. Se pudo establecer que con una cantidad de Ce del 6% se mejora la estabilidad catalítica y se reduce la formación de depósitos carbonosos. La evaluación catalítica para las presentaciones no reducidas de los catalizadores, en polvo o inmovilizado, expuso influencia no negativa al inmovilizar los óxidos mixtos en el estructuras monolíticas, dado que para estas se observó un desempeño catalítico altamente activo en la reacción, donde no hubo variación en la conversión de los reactivos y una ligera disminución de la selectividad de los productos del gas de síntesis, en comparación con el polvo, pero aun así manteniendo relaciones H2/CO cercanas a 1,2 con monolitos utilizados con un WHSV = 94.680 $mL \cdot g_{Cat}^{-1} \cdot h^{-1}$.

La reducción previa y la evaluación de los catalizadores a 600°C dieron como resultado un aumento considerable en la formación de coque. Sin embargo, a diferencia de los catalizadores en polvo que

sufren caídas de presión, los catalizadores monolíticos, a pesar de formar una mayor cantidad de coque, demuestran notable estabilidad y retiene una alta actividad catalítica.

Se evidenció que los catalizadores inmovilizados en monolitos presentan una excelente oportunidad para escalar en la industria, considerando su excelente desempeño después de una primera prueba catalítica, su recuperación y su reutilización en una segunda prueba catalítica.

Palabras clave: Efecto invernadero, gas de síntesis, reformado, metano, óxidos mixtos, cerio, monolito.

UNIVERSIDAD
NACIONAL
DE COLOMBIA

Ni-Ce immobilized catalysts in cordierite monoliths for dry reforming of methane

María Alejandra Osorio Zabala

Advisor:
Carlos Enrique Daza Velásquez, Ph. D.
Associate Professor

Universidad Nacional de Colombia
Facultad de Ciencias
Departamento de Química
Bogotá, Colombia
2023

Ni-Ce immobilized catalysts in cordierite monoliths for dry reforming of methane

María Alejandra Osorio Zabala
Chemist, B. Sc.

Master's thesis presented as a partial requirement to qualify for the title of:
Master in Science – Chemistry

Advisor:
Carlos Enrique Daza Velásquez, Ph. D.
Associate Professor

Research Group:

Universidad Nacional de Colombia
Facultad de Ciencias
Departamento de Química
Bogotá, Colombia
2023

“We keep moving forward, opening new doors and doing new things, because we’re curious and curiosity keeps leading us down new paths”

Walt. Disney

ACKNOWLEDGMENTS

To Professor Carlos Enrique Daza Velasquez, director of this work, who allowed joining the ESCA research group. I especially appreciate his guidance, patience, trust, motivation, and valuable advice during this academic, professional, and personal training.

To Professor Rafael Molina and Professor Sonia Moreno, for their help, willingness, and guidance during my participation in the research group.

Also, I would like to thank my colleagues and friends from the ESCA group, who supported me from day one, offered me their friendship, and always provided me with their knowledge. To the National University of Colombia, where I learned and grew, both academically and personally.

CONTENT

ABSTRACT ..... *VII*

LIST OF FIGURES ..... *VIII*

LIST OF TABLES ..... *X*

LIST OF ABREVIATIONS ..... *XI*

INTRODUCTION ..... *XII*

1.STATE OF ART *14*

1.1. Current environmental scenario **14**

1.2. CO_2 capture, storage, and utilization **16**

1.3. Natural gas, gas to liquid technology, and syngas **18**

1.4. Dry reforming of methane **19**

1.4.1. Thermodynamics 19

1.4.2. Industrial applications 20

1.4.3. Reaction mechanism 21

1.5. Catalysts for DRM **23**

1.5.1. Catalytic active phase 23

1.5.2. Catalytic support 24

1.5.3. Ceria promoted catalysts 26

1.6. Structured catalysts as monoliths **28**

1.6.1. Obtaining structured catalysts in monoliths 30

1.6.2. Immobilized catalysts in monoliths for DRM 32

1.7. Background **35**

2.HYPOTHESIS *40*

3.OBJECTIVES *41*

3.1. General objective **41**

3.2. Specific objectives **41**

4.METHODOLOGY *42*

4.1. Synthesis of catalysts **42**

4.1.1. Chemicals and materials 42

4.1.2. Synthesis of powdered catalysts by co-precipitation 42

4.1.3. Immobilization of mixed oxides in cordierite monoliths by slurry coating 42

4.2. Characterization of the materials **44**

4.2.1. Characterization of the powdered catalysts 44

4.2.2. Characterization of the immobilized mixed oxides 44

4.3. Catalytic test **45**

4.4. Characterization of the spent catalysts **46**

5.RESULTS AND ANALYSIS ***48***

5.1. Characterization of the powdered catalysts **48**

5.2. Characterization of the immobilized mixed oxides **56**

5.3. Catalytic test with powdered catalysts **58**

5.3.1. Test for non-reduced powdered catalysts 58

5.3.2. Test for reduced powdered catalysts 61

5.4. Catalytic test with immobilized mixed oxides **63**

5.4.1. Reactor's catalytic activity 63

5.4.2. Tests for non-reduced immobilized catalysts 64

5.4.3. Reusability test of non-reduced immobilized catalysts 66

5.4.4. Test for non-reduced immobilized catalysts with a higher load of catalyst 68

5.4.5. Tests for reduced immobilized catalysts with a higher load of catalysts 70

5.4.6. Comparative final analysis 72

6.CONCLUSIONS ***74***

7.PERSPECTIVES ***76***

REFERENCES ***77***

SUPPLEMENTARY INFORMATION ***87***

ABSTRACT

In this master's thesis, Ni-Mg-Al powdered and immobilized mixed oxide-type catalysts promoted with Ce (1-6%) were obtained by the method of coprecipitation and slurry coating of hydrotalcite precursors. The promoter role of the Ce and the effect of immobilizing the mixed oxides in cordierite monoliths on the physicochemical properties and the catalytic performance of the materials in the dry reforming of methane were studied. The catalysts were characterized by diverse analytical techniques to evaluate their chemical composition, thermal and structural properties, and reductive, basic, and morphological properties. The catalytic evaluation was studied through several stability tests for 8h at 700 ° C (for non-reduced catalysts) and at 600 °C (for pre-reduced catalysts) with WHSV of 94,680 and 23,670 $mL \cdot g_{Cat}^{-1} \cdot h^{-1}$.

Results showed that the increase in the content of Ce influences the formation of smaller Ni crystallite sizes, promotes the reduction of Ni, increases the ability to capture CO_2 at high temperatures, and favors the formation of smaller particle sizes of Ni^0. In turn, the immobilization of mixed oxides did not mean a change in the crystalline structure of the cordierite monoliths; and the formation of a coat of mixed oxides over the surface of the monoliths, with an average thickness of 6.13μm for monoliths with ~25mg of immobilized mixed oxide and an average layer thickness of 9.87μm for monoliths with ~100mg of immobilized mixed oxide.

The results of the catalytic evaluation showed that Ce does not influence the activity, but it does improve stability. It was possible to establish that with an amount of Ce of 6% the catalytic stability is improved, and the formation of carbonaceous deposits is reduced. The catalytic evaluation for the non-reduced presentations of the catalysts, powder or immobilized, exposed the non-negative influence of immobilizing the mixed oxides in the monolithic structures, given that for these a highly active catalytic performance was observed in the reaction, where there was no variation in the conversion of the reagents and a slight decrease in the selectivity of the synthesis gas products, compared to the powder, but still keeping H_2/CO ratios close to 1.2 with monoliths used with a WHSV = 94,680 $mL \cdot g_{Cat}^{-1} h^{-1}$. The pre-reduction and evaluation of the catalyst at 600°C resulted in a considerable increase in coke formation. However, unlike powdered catalysts that suffer from pressure drops, monolithic catalysts, despite forming a higher amount of coke, demonstrate remarkable stability and retain high catalytic activity.

It was evidenced that the catalysts immobilized in monoliths present an excellent opportunity for scaling in the industry, considering their excellent performance after a first catalytic test, their recovery, and their reuse in a second catalytic test.

Keywords: Greenhouse effect, synthesis gas, dry reforming, methane, mixed oxides, cerium, monolith.

LIST OF FIGURES

Fig. 1. World annual CO_2 emissions (Year Vs CO_2) from fossil fuels (coal, oil, and gas), flaring, cement, steel, and other industrial processes.[38] 14

Fig. 2. World map of 2021 CO_2 emissions from fossil fuels and industry.[38] 16

Fig. 3. Current and future hydrogen demand and production; A) Industrial profiles of hydrogen demand in 2015 and 2050, B) current and projected hydrogen production technologies.[1] 18

Fig. 4. Mechanistic steps for DRM adapted from Abdulrasheed et al.[12] 22

Fig. 5. Two-dimensional volcano-curve of the turnover frequencies (log 10) as a function of O and C adsorption energy. T=500ºC, p=1atm. [8], [69] 23

Fig. 6. Schematic representation of a single square monolith channel A) transversal section with parameters employed to characterize the monolith geometry, B) 3D representation.[106] 29

Fig. 7. Different paths towards obtaining monolithic catalysts.[110] 31

Fig. 8. A) Clean cordierite monoliths, B) cordierite monoliths after slurry coating. 43

Fig. 9. Schematic of the reaction unit for the DRM process. 45

Fig. 10. X-ray diffractograms were recorded for A) mixed oxides, B) mixed oxides reduced at 700ºC-1h and C) mixed oxides reduced at 800ºC-1h. • : Periclase-like structure, ▼ : CeO_2 fluorite structure, ■ : Ni^0 metallic nickel. 49

Fig. 11. H_2-TPR profiles of A) mixed oxides and B) mixed oxides after reduction at 700ºC-1h. 51

Fig. 12. CO_2-TPD for the mixed oxides after reduction at 700ºC-1h. 53

Fig. 13. TEM images of the mixed oxides reduced at 700ºC-1h and the nanoparticle size distribution. A) MO1r, B) MO2r, C) MO3r and D) MO4r. 55

Fig. 14. X-ray diffractograms were recorded for the bare cordierite and the SMOx fresh after calcination at 700ºC-12h and powdered. ▢: Cordierite. 56

Fig. 15. SEM micrographs of the structured mixed oxides A) SMO1, B) SMO2, C) SMO3, D) SMO4. 57

Fig. 16. Histograms derived from measurements of coated layer thickness from the obtained SEM micrographs. A) for 0.025 g and B) for 0.100 g loaded monoliths. 58

Fig. 17. Catalytic A) CH_4, B) CO_2 conversion; catalytic C) H_2, D) CO selectivity and E) H_2/CO vs. TOS for non-reduced powder catalysts. Reaction conditions: 700ºC-8h and 94,680 $mL \cdot g_{Cat}^{-1} \cdot h^{-1}$ 59

Fig. 18. A) TGA and B) DSC profiles for non-reduced powder catalysts. Reaction conditions: 700ºC-8h and 94,680 $mL \cdot g_{Cat}^{-1} \cdot h^{-1}$ 60

Fig. 19. SEM micrographs of A) MO1 and B) MO4 non-reduced powder catalysts after catalytic test at 700ºC-8h, 94,680 $mL \cdot g_{Cat}^{-1} \cdot h^{-1}$ 61

Fig. 20. Catalytic A) CH_4, B) CO_2 conversion; catalytic C) H_2, D) CO selectivity and E) H_2/CO vs. TOS for reduced powder catalysts. Reaction conditions: 600ºC-8h and 94,680 $mL \cdot g_{Cat}^{-1} \cdot h^{-1}$. 62

Fig. 21. A) TGA and B) DSC profiles for reduced powder catalysts. Reaction conditions: 700ºC-8h and 94,680 $mL \cdot g_{Cat}^{-1} \cdot h^{-1}$. 63

Fig. 22. Catalytic A) CH_4 and CO_2 conversion; catalytic C) H_2 and CO selectivity vs. TOS for metallic reactor with bare cordierite monolith. Reaction conditions: 700ºC-8h. 64

Fig. 23. Catalytic A) CH_4, B) CO_2 conversion; catalytic C) H_2, D) CO selectivity and E) H_2/CO vs. TOS for non-reduced catalysts structured in cordierite monoliths. Reaction conditions: 700ºC-8h, 94,680 $mL \cdot g_{Cat}^{-1} \cdot h^{-1}$. 65

Fig. 24. Reusability tests A) CH_4, B) CO_2 conversion; catalytic C) H_2, D) CO selectivity and E) H_2/CO vs. TOS for non-reduced catalysts structured in cordierite monoliths. Reaction conditions: 700ºC-8h, 94,680 $mL \cdot g_{Cat}^{-1} \cdot h^{-1}$. 66

Fig. 25. Carbon production during the first and second catalytic tests on the mixed oxides structured in the cordierite monoliths. 67

Fig. 26. SEM micrographs of the structured MO2 after being used for a DRM at 700ºC-8h, calcinated, and reused for a new reforming reaction. 68

Fig. 27. Catalytic A) CH_4, B) CO_2 conversion; catalytic C) H_2, D) CO selectivity and E) H_2/CO vs. TOS for non-reduced catalysts structured in cordierite monoliths. Reaction conditions: 700ºC-8h WHSV = 23,679 $mL \cdot g_{Cat}^{-1} \cdot h^{-1}$. 69

Fig. 28. Carbon production during catalytic tests on the non-reduced powder mixed oxides and non-reduced catalysts structured in the cordierite monoliths at several WHSV. 70

Fig. 29. Catalytic A) CH_4, B) CO_2 conversion; catalytic C) H_2, D) CO selectivity and E) H_2/CO vs. time on stream. For mixed oxides structured in cordierite monoliths, with the previous reduction with H_2 flow at 700ºC-1h. Reaction conditions: 600ºC-8h, 23679 $mL \cdot gCat^{-1} \cdot h_{rxn}^{-1}$. 71

Fig. 30. Carbon production during catalytic tests on the reduced powder mixed oxides and reduced catalysts structured in the cordierite monoliths. Reaction at 600 °C. 72

LIST OF TABLES

Table 1. Summary of the percent decline in CO_2 emissions from some main emitting countries in the first quarter of 2020.[37] 15

Table 2. Thermodynamic properties, reactant conversions, and product yield for DRM at equilibrium with CO_2/CH_4 ratio of 1 at atmospheric pressure.[9], [59] 20

Table 3. Possible elementary reactions involved in DRM reaction; * is used to represent unoccupied active sites.[61], [65] 21

Table 4. Performance of metals used as catalysts for DRM. 24

Table 5. Ni/Mg/Al HTs-derived mixed oxides promoted with Ce catalysts tested for DRM process. 27

Table 6. Monolith coating methods.[25], [110], [113] 31

Table 7. Main information on obtaining, catalytic evaluation conditions and performance of different monolithic catalysts reported for DRM. AP: active phase, P: promoter, PR: pre-reduction, RC: reaction condition. 35

Table 8. XRF results for elementary chemical analysis of the mixed oxides obtained. 48

Table 9. Brucite-like structure crystallographic parameter and CeO_2 and Ni^0 crystallite sizes. Reducibility of the mixed oxides at 700ºC. TEM Ni^0 particle sizes. 50

Table 10. Basicity of prepared materials. 53

LIST OF ABBREVIATIONS

Symbol	Term
GHG	Greenhouse gases
IPCC	Intergovernmental Panel on Climate Change
WG3	Working Group III
NEAA	Netherlands Environmental Assessment Agency
COP26	Conference of the Parties 26^{th}
NDC	National determined contributions
UNFCCC	United Nations Framework Convention on Climate Change
CCUS	Carbon Capture Utilization and Storage
DRM	Dry reforming of methane
NG	Natural gas
GTL	Gas to Liquid Technology
SRM	Steam reforming of methane
POX	Partial oxidation of methane
RWGS	Reverse water-gas shift
DFT	Density functional theory
HTs	Hydrotalcite-like mixed layered hydroxides
LDHs	Layered double hydroxides
ICOSCAR	International Conference on Structured Catalysts and Reactors
L	Monolith's channel size
w	Monolith's wall thickness
N	Monolith's cell density
OFA	Open frontal area
GSA	Geometric surface area
XRF	X-ray fluorescence
XRD	X-ray powder diffraction
JCPDS	Joint Committee of Powder Diffraction Standards
H_2 – TPR	Temperature-programmed reduction with H_2
TCD	Thermal conductivity detector
CO_2 – TPD	Temperature-programmed desorption with CO_2
TEM	Transmission electron microscopy
EDX	Energy dispersive X-ray spectroscopy
SEM	Scanning electron microscopy
GHSV	Gas hourly space velocity
TGA	Thermogravimetric analysis
DSC	Differential scanning calorimetry
FID	Flame ionization detector
TOS	Time on stream

INTRODUCTION

In the current global energy situation, fossil fuels still represent over 80% of the total energy supply, and as is well known, their extraction, conversion to usable energy, and use have several contributions to global warming greenhouse gases, and some other harmful environmental impacts.[1] However, the development of new energy sources and the different employment methods of fossil fuels are gaining special development thanks to scientific work and technological growth.[2] This is why the role of natural gas as the world's primary energy source is growing fast, given its forecast to outlast oil by a significant margin, and its possibility of conversion to clean burning liquid fuels and chemicals by making use of Gas to Liquid technology.[3] From a pro-environmental point of view, an important incentive for natural gas upgrading is that this gas-to-liquid technology produces natural gas-derived fuels that do not contain sulfur or polynuclear aromatics and produce less CO_2 than petroleum.[4]

In this technology, three processing steps are identified: the generation of syngas (CO/H_2) by reforming or partial oxidation, syngas conversion by Fischer-Tropsch synthesis into n-alkanes, and hydroprocessing by mild hydrocracking of these substances. Focusing on the generation of syngas, it is reported as the key processing step to obtain an economical process for fuel production.[5], [6] Thus, to obtain syngas, sources such as coal, biomass, and natural gas have been explored along with efficient and appropriate methods to generate a gas mixture by reactions with steam, oxygen, or carbon dioxide.[7] In the case of natural gas, which is mainly composed of methane, four processes have been developed to obtain syngas: Steam reforming, partial oxidation, autothermal reforming, and dry reforming (DRM).[8]

DRM, the main focus of this work, is an attractive reaction owing to the possibility of simultaneously converting two greenhouse gases into syngas.[9] It is a reaction in which methane reacts with carbon dioxide in the presence of a Ni (or noble metal) catalyst, obtaining an H_2/CO ratio of 1, which is considered the ideal type of reforming process when it comes to the use of syngas produced as a raw material for the synthesis of important liquid fuels by Fischer-Tropsch technology.[10] Some disadvantages that DRM presents are the costly industrial employment being an endothermic process and the significant production of by-products, especially carbon, which subsequently deposits on the surface of the catalyst affecting its activity and causing drop pressure in the reactors.[11], [12]. The main challenge for the industrial application of DRM is related to the development of active catalytic materials, mainly with a low carbon formation rate, either on the catalysts or in the cold zones of the reactor.[13]

Several types of catalysts have been used to activate the reaction; having an important preference for those that present a good performance, high thermal stability, and high resistance toward deactivation from poisoning, or in concrete terms, the ones that meet good conditions of activity, selectivity, and stability.[13], [14] In this way, different transition metals can be used as catalysts for DRM, and nickel is the most widely used because of its good performance and cheap acquisition, even though nickel catalysts have poor stability due to carbon deposition.[15] Additionally to the active phase, the roles of the catalytic supports have also been recognized as crucial to the processes, and some powder supports, like for

example γ-Al_2O_3 or MgO have been reported on several papers as supports for nickel catalysts for CH_4/CO_2 reforming.[8], [16]

Going further into different catalytic supports, in the last decades, articles that expose the use of precursors such as hydrotalcites or perovskites, and smectites as mainly nickel-catalytic supports have been published.[17]–[21] These articles have reported improvements against coke deposition, sintering, and higher H_2 and CO yields, owing to the properties that these materials offer: high thermal stability, large surface area, and a characteristically basic surface. This opens up a diverse opportunity for the development of more investigations that may drive CO_2 reforming of methane for efficient, economical, and favorable industrial applications.

In addition to the catalytic support, it is vital to recognize the significance of promoter species within the catalytic system. These promoters play a crucial role in augmenting the favorable characteristics of both the active phase and catalytic support. Potential promoter materials include alkali, alkaline earth, transition metals, and rare earth metal oxides.[22] For example, it is reported that in Ni-based catalysts Ce or Pr oxides are implemented.[23], [24]

However, the development of excellent active phases, catalytic supports, and promoters, has been guided mainly in obtaining powder-like catalysts, that still do not present fully evolved characteristics for their wide use in the industry; for this reason, the development of structured catalysts as monoliths have been proposed to obtain a system with better performances, even less coke formation and high H_2/CO ratios, favored by the easy industrial manipulation of the monoliths, their high thermal and structural stability, along with its high thermal conductivity; adding the different benefits of the materials that have the potential to be used as the monolithic base (i.e. cordierite-type).[25]–[27]

This study investigates the impact of immobilizing coprecipitated Ni-Ce catalysts onto cordierite monoliths on their catalytic performance in DRM. The aim was to provide valuable insights into the potential scalability of this process. The catalysts were prepared using the coprecipitation method, which is a well-established technique within our research group known for the synthesis of highly efficient powder catalysts for DRM.[28]

This document presents an updated review of the state of the art, in which environmental problems are addressed and dry reforming of methane is presented as a viable alternative to reduce the concentration of greenhouse gases, with the most relevant thermodynamic and kinetic aspects related to this reaction, along with the possible catalyst's active phase, support, promoters, and monolithic structures that will be employed. Next, based on this review, in the second part, the hypotheses and objectives of this research work were developed are presented. A description of the synthesis of the catalysts and characterization techniques used to elucidate the physicochemical properties of the solids, as well as the details of the experimental setup and protocol for the catalytic evaluation of the materials. As a fundamental part of the text, the analysis and discussion of the results obtained from the characterization of the materials are presented, and the results of the catalytic evaluation are presented in correlation with the physicochemical properties of solids. The text ends with general conclusions and recommendations for further research.

1. STATE OF ART

1.1. Current environmental scenario

Climate change has come to be recognized as today's huge challenge for humanity, since it is an exponential environmental problem of global magnitude, that besides the main long-term threat to all ecosystems and humanity, brings with it social and economic repercussions to societies nowadays.[29] All consequences of the increase in the anthropological activities that produce greenhouse gases (GHG) emissions, characterized by the Intergovernmental Panel on Climate Change (IPCC) Working Group III (WG3) as energy systems, industry, buildings, transport, agriculture, forestry, and other land uses.[30]

Even though there are different uncertainties associated with historical GHG emissions estimates [30], substantive literature complies with global emissions inventories for carbon dioxide (CO_2) [31], [32], methane (CH_4) [33], [34] and other gases like nitrous oxide (N_2O) [35], [36] emissions. The carbon oxidation resulting from fossil fuel combustion is the largest source of CO_2 emission, the primary driver of global climate change, which is directly associated with various processes in power plants, oil refineries, and vast industrial conveniences.[37] Given the growing global population and increasing energy demands, it is highly probable that CO_2 levels will rise (**Fig.1**). Therefore, more stringent actions are mandatory to control and mainly limit the CO_2 emissions into the atmosphere; at the same time as the development of environmentally friendly and economic energy sources with the promise of the cleaner environment in the future are highly desirable.

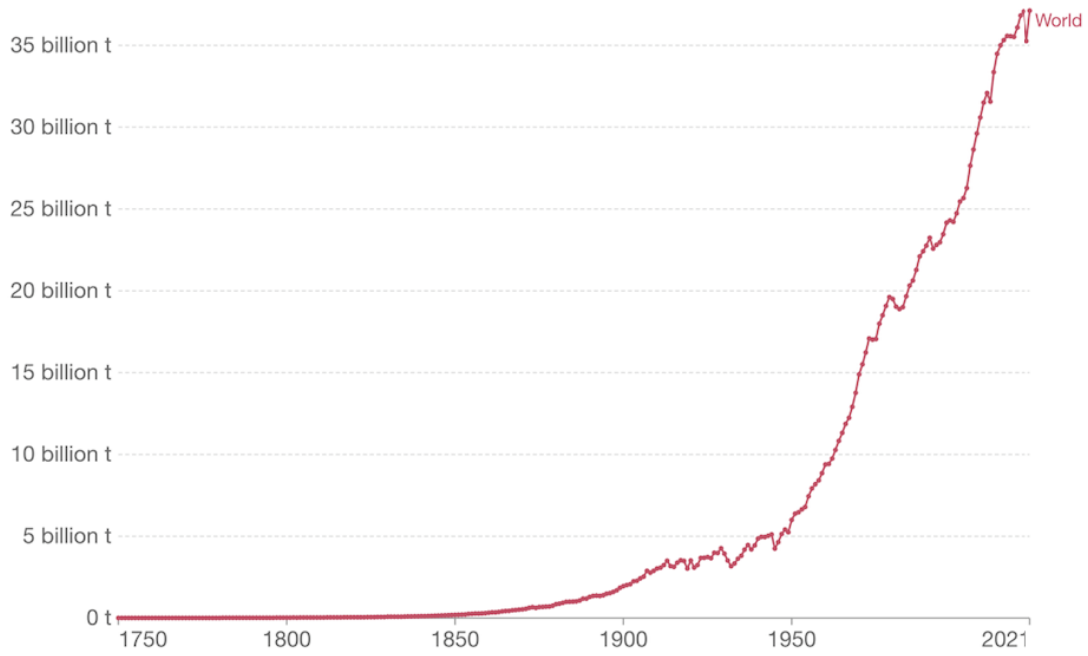

Fig. 1. World annual CO_2 emissions (Year Vs CO_2) from fossil fuels (coal, oil, and gas), flaring, cement, steel, and other industrial processes.[38]

In 2020, a report by the Netherlands Environmental Assessment Agency (NEAA) highlighted global greenhouse gas (GHG) and CO_2 emissions. According to the report, 2019 was the second warmest year on record, witnessing an average temperature increase of 0.95ºC for both land and ocean surfaces over the past 140 years.[39]

During the COVID-19 pandemic, despite seasonal variations, there was a significant reduction in daily CO_2 levels. Where an estimated trend in the global decline of 7.8% in CO_2 emissions was observed during the initial 4 months of 2020 in contrast with the first trimester of 2019.[37] Understanding that the CO_2 reductions were not similar for all countries (see **Table 1.**) and it could be observed that it was greater in April and March 2020 due to the stringent restrictions.

Table 1. Summary of the percent decline in CO_2 emissions from some main emitting countries in the first quarter of 2020.[37]

Country	% Decrease
China	9.3
EU27 & United Kingdom	8.4
United States	4.7
Japan	3.6
India	2.5
Russia	2.1

However, authors like Kumar et al.[37] expose that to improve the economy due to the pandemic, most of the countries may consume more energy than pre-pandemic era increasing CO_2 emissions levels; which anticipates that the pandemic and consequent shut-downs may not impact the emissions over a two-year time zone.

Recognizing the urgent need to address the critical situation of climate change, the United Kingdom hosted the 26th annual United Nations climate change conference (COP26) in Glasgow in November 2021. Summit documented that the first round of commitments of the Paris Agreement, called national determined contributions (NDC), were not ambitious enough to drive global emissions into a pathway of 2ºC or well below 2ºC global average temperature increase by 2100.[40] That is why in the Glasgow COP26 several major emitters have announced new climate neutrality commitments and others revised their NDC; strategies that according to Aleluia et al.[41], if fully implemented, would help close the gap to 2ºC, covering more than 80% of the world's needed emission reductions by 2070. Understanding that the Glasgow pledges would require substantial increases in investment in net-zero transportation and power generation in all major economies.[41], [42]

As can be deduced from **Fig. 2.**, South America is a fairly small emitter: accounting for 4% of global emissions; however, in the context of climate change, Latin America and the Caribbean play significant but underappreciated roles. Given that they are hotspots of vulnerability to floods, heat waves, and other hazards that climate change is projected to exacerbate, in addition to being growing sources of GHG.[38], [43] The countries of Latin America are actors committed to the United Nations Framework Convention on Climate

Change (UNFCCC) and to the negotiation of common points, where their NDC demonstrate their commitment to advancing multilateral climate policies.

For example, Colombia attended the Glasgow meeting with the commitment to reduce GHG emissions by 51% by 2030, reach carbon neutrality by 2050, achieve zero deforestation, and have 30% of its territory protected by 2030. Goals, which are expected, will be developed in collaboration, in terms of generating regulations, climate action, and technology transfer, with a wide range of key parties including the EU, Japan, and China among others.[43], [44]

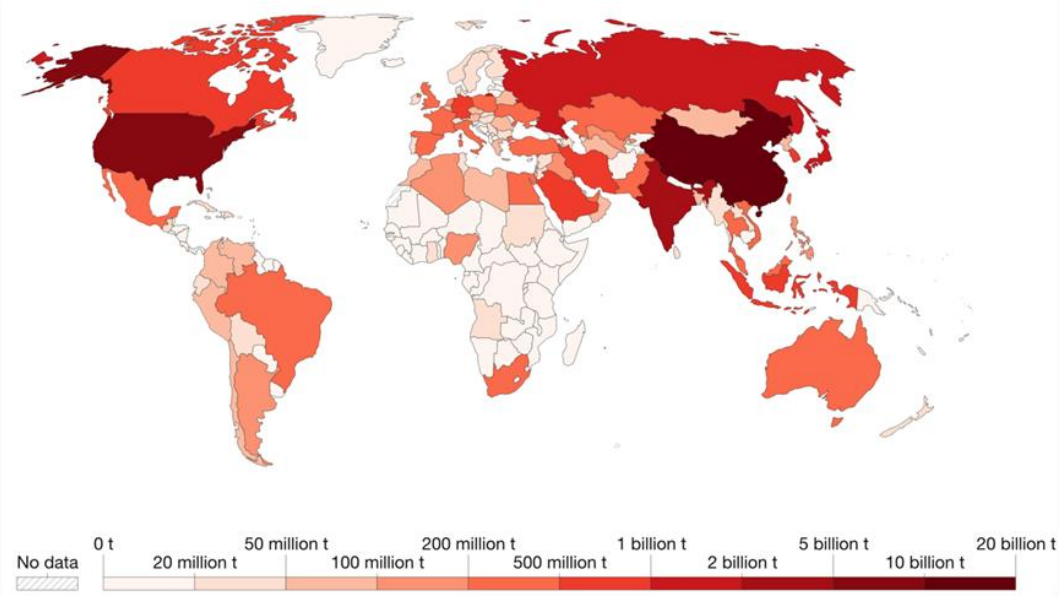

Fig. 2. World map of 2021 CO_2 emissions from fossil fuels and industry.[38]

1.2. CO_2 capture, storage, and utilization

In industrial ecology, a fundamental principle to achieve sustainable development is the approach to ideally closed cycles, on which the materials being evaluated can have uses and transformations that do not generate unusable waste.[45] CO_2 management in terms of carbon capture, utilization, and storage (CCUS) has become an important topic in public discussion and is reflected in efforts, research, and development both in academia and industry during the last two decades.[8]

Industrially, there are three technological routes for capturing CO_2 from industrial sources: pre-combustion, post-combustion, and oxy-fuel capture.[46]–[48] By the pre-combustion route, fuels are converted to H_2 and CO_2, and the CO_2 produced is separated before combustion. In the post-combustion process, the CO_2 is separated from the flue gas produced by fuel combustion, and oxy-fuel combustion consists of the combustion of the fuel in pure oxygen, producing high-purity flue gas steam of CO_2 and H_2O to remove water by condensation.[45], [49]

Specifically, CO_2 capture adsorption methods can be implemented on different materials. Kelektsoglou et al. [49] present a summary of some of these different materials that, due to

adsorption processes to capture the gas, have the potential for use in power plants: carbons, alumina, zeolites, silicas, metal-organic frameworks, hydrotalcite-derived oxides, and polymers. Shimizu et al. [50] mention the Ca-looping process, where CaO is used to remove CO_2 from combustion systems, obtaining $CaCO_3$; then, over 90% of the regeneration of the gas is achieved by the O_2 combustion of the carbonate, all under atmospheric pressure. An advantage of this process is the high purity of the CO_2 obtained since the absorbent does not retain the water produced in conventional air-blow combustors, and it is a considerably affordable process.

On the other hand, different chemical capture methods are also used with species such as amine-based ones: aqueous monoethanolamine, 2-amino-2-methyl-1-propanol, and aqueous piperazine. [45] Nevertheless, the use of these absorbents can be expensive, so publications such as those by Ramezani et al. [51] expose the use of potassium carbonate for the same process with lower costs. As an alternative to CO_2 capture from industrial sources, some methods for capturing directly from the air have also been developed; these processes present great challenges mainly due to the low concentration of CO_2 in the atmosphere compared to the concentration found in the flue gases generated during industrial production,100 – 300 times lower, therefore it demands more energy. Two of the most common methods for this are adsorption with immobilized amines or anion exchange resins.[45], [49]

Delving into CCUS, CO_2 transportation, and storage are reported to be convenient in pipes that can transport them over short distances, which is necessary for temperature and pressure control because the CO_2 must be in a dense phase to avoid problems with its flow through the pipelines. For the same reason, it is important to consider the CO_2 purity or the matrix in which it has been captured because the storage conditions depend on it.[46], [48] Otherwise, one of the advantages of pipeline transportation is the possibility of continuous flow, which accommodates the amount of product obtained in an industrial environment with continuous production. However, for long distances, using pipelines is an expensive process, so in the literature, it is found that to transport the reagent over distances greater than 1500 km, a low-cost solution is the use of cargo ships.[52]

From an industrial point of view, CO_2 is not only a waste product with a harmful environmental footprint, its implementation as raw material into value chains offers certain potentials. A range of processes for the chemical valorization of CO_2 are already well established; two large-scale chemical technologies that rely on CO_2 as feedstock are the methanol production from H_2 and CO_2 and the production of urea from NH_3 and CO_2.[8], [53]

Several processes are intensely studied for the CO_2 conversion reactions, including CO_2 hydrogenation to various products and equally important, the obtaining of hydrogen gas, knowing its growing potential as a future energy source (see **Fig. 3, A**) with numerous advantages. The CO_2 (or dry) reforming of methane (DRM) process, aimed at obtaining a mixture of H_2 and CO, has immense potential as an ally for H_2 production. This potential is further accentuated by the growing prospects of obtaining hydrogen using natural gas as the methane source and implementing CCUS methods, which are projected to see significant growth between 2030 and 2050 (see **Fig. 3, B**).[1], [53], [54]

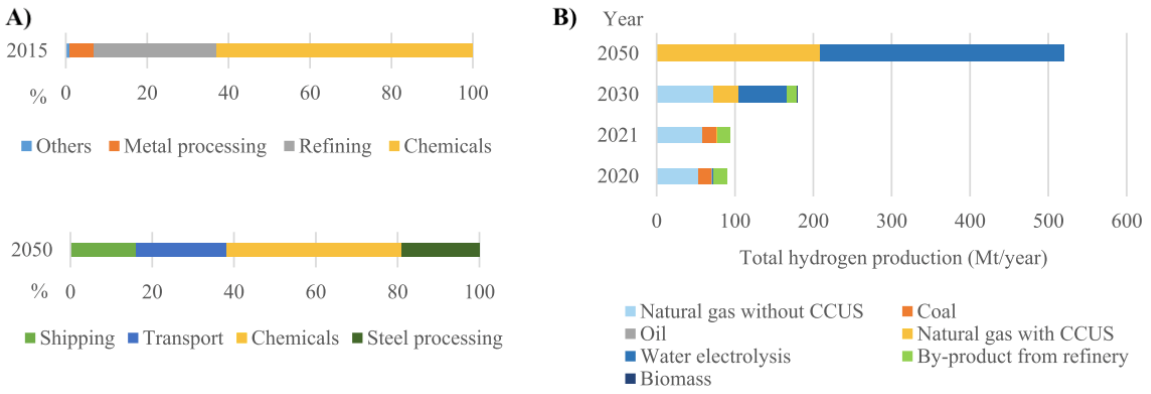

Fig. 3. Current and future hydrogen demand and production; A) Industrial profiles of hydrogen demand in 2015 and 2050, B) current and projected hydrogen production technologies.[1]

1.3. Natural gas, gas to liquid technology, and syngas

In the present global energy situation, fossil fuels (petroleum, coal, and natural gas) still represent over 80% of the total energy supplies, and as already mentioned, their extraction, conversion to usable energy, and uses have several contributions to global warming, GHG and some other environmental impacts. But the road toward new energy sources and different employment ways for fossil fuels is getting special development thanks to scientific work and technological growth.[2]

The role of natural gas (NG) as the world's primary energy source is growing fast, given its forecast to outlast oil by a significant margin and its possibility of conversion to clean-burning liquid fuels and chemicals by making use of Gas to Liquid Technology (GTL).[2] The important incentive for NG upgrading is that this GTL technology produces NG-derived fuels that do not contain sulfur or polynuclear aromatics with lower CO_2 generation than petroleum.[4] In the GTL technology, three processing steps are identified: generation of syngas (H_2/CO) by reforming or partial oxidation; syngas conversion by Fischer-Tropsch synthesis into n-alkanes; and hydroprocessing by mild hydrocracking of these compounds.[3]

Focusing on the generation of syngas, it is reported as the key processing step to obtain an economical process for fuel production. The syngas production stage consumes about 60% of the capital investment.[4] Thus, to obtain syngas, some sources like coal, biomass, and natural gas have been explored, along with efficient and appropriate methods to generate the gas mixture by reactions with steam, oxygen, or carbon dioxide.[5], [6] In the case of NG, which is mainly composed of methane (percentage depending on the source of the gas), four processes have been developed to obtain syngas.

The steam reforming of methane (SRM) is the most common process for hydrogen generation providing 50% of the global demand and producing a hydrogen-rich gas mixture with significant CO content (**Eq. 1**). SRM requires temperatures between 800 – 1000ºC and nickel-based catalysts.[55] Advantages of SRM include low carbon formation on catalysts,

suitability for high-pressure processes, and easy product separation. However, there are associated problems such as a high H_2/CO ratio, the need to separate products for follow-up Fischer-Tropsch synthesis, and its energy-intensive characteristics.[56]

$$CH_4+H_2O \leftrightarrow CO+3H_2, \Delta H_{298}=206\ kJ.mol^{-1} \quad (1)$$

The exothermic partial oxidation of methane reaction (POX), or oxy-reforming (**Eq. 2**), is possible with Ni, Co o Fe catalysts and works under temperatures of 455 – 898ºC, ending up with an H_2/CO ratio of 2, good ratio for downstream processes. Some pros of this reaction are its mild exothermic reaction and its energy-saving virtues.[57]

$$CH_4+1/2O_2 \leftrightarrow CO+2H_2, \Delta H_{298}=-35.6\ kJ.mol^{-1} \quad (2)$$

The autothermal reforming of methane could be described as a combination of both steam reforming and partial oxidation [13] This method was designed to save energy, as the thermal energy required by the SRM is generated in POX. The value obtained for the H_2/CO ratio from this process is a function of the gaseous reactant fractions introduced in the development of the method.[13]

Finally, DRM (**Eq. 3**), is an attractive reaction thanks to the possibility of simultaneously converting two GHG into syngas; for this reason, its contribution in the cycles of capture, storage, and use/valorization of CO_2, previously mentioned is considered.[58] DRM is a reaction where CH_4 reacts with CO_2 in the presence of catalysts, resulting in an H_2/CO ratio of 1. This specific ratio makes the process an ideal reforming method for utilizing the syngas produced as a raw material in the synthesis of essential liquid fuels through Fischer-Tropsch.[8]

$$CH_4+CO_2 \leftrightarrow 2CO+2H_2, \Delta H_{298}=247.3\ kJ.mol^{-1} \quad (3)$$

1.4. Dry reforming of methane

1.4.1. Thermodynamics

DRM is a highly endothermic process that has an exergonic nature at temperatures above 645ºC. Catalytic conversions can be achieved at temperatures below 600ºC, generally not directly attributed to the reforming reaction but to some possible side reactions.[9] As shown in **Table 2**, the highest conversion and yield percentages for the DRM reaction are reached at temperatures between 700 and 800ºC, exposing the high amount of energy that must be applied to the system to obtain the syngas.

Table 2. Thermodynamic properties, reactant conversions, and product yield for DRM at equilibrium with CO_2/CH_4 ratio of 1 at atmospheric pressure.[9], [59]

T (ºC)	ΔH (kJ.mol^{-1})	ΔG (kJ.mol^{-1})	Conversion CH_4 (%)	Conversion CO_2 (%)	Yield H_2 (%)	Yield CO (%)
500	258.9	40.4	70.9	45.9	28.5	3.5
600	259.6	12.4	82.3	47.2	52.5	17.4
700	259.9	-16.3	91.5	66.3	75.9	50.8
800	259.9	-44.7	96.3	88.6	90.6	82.9

DRM is an equilibrium reaction that can be influenced by some collateral reactions favored under temperature conditions. One of the principal reactions is the reverse water-gas shift (RWGS), in which H_2 is consumed and CO is generated (**Eq. 4**), thus affecting the H_2/CO ratio, making it less than unity. The RWGS reaction can have a special influence on the reforming reaction when temperature conditions reach 800ºC or more since the Gibbs free energy for it gets to negative values at this temperature.[59]–[61]

$$CO_2+H_2 \leftrightarrow CO+H_2O,\ \Delta H_{298}=41\ kJ.mol^{-1} \quad (4)$$

Another side reaction of DRM is the methane cracking reaction (**Eq. 5**), which is mainly responsible for carbon deposition, along with Boudouard reaction (**Eq. 6**). These two reactions, with the relative contribution of each depending on the reforming process conditions, are among the biggest obstacles to the implementation of DRM in an industrial context, considering that inactive carbon deposition is the main reason for the deactivation of the catalysts used in the process to obtain syngas.[8] However, as Bradford et al. [62] mention, the carbon formation still depends on different parameters: the metal used as the active phase of the catalysts, the metal crystalline structure, the particle size, the metal-support interactions, the support acidity or basicity and the implementation of some promoter metals on the catalysts.

$$CH_4 \leftrightarrow C+2H_2,\ \Delta H_{298}=74.9\ kJ.mol^{-1} \quad (5)$$
$$2CO \leftrightarrow C+CO_2,\ \Delta H_{298}=-172.4\ kJ.mol^{-1} \quad (6)$$

One of the pros of the RWGS reaction is that the steam produced by it enables steam/carbon gasification[61], helping with the carbon deposition problem. This is one of the reasons why SRM exhibits less carbon formation than DRM and is widely used in industry.[8] However, this method still presents an H_2/CO rate greater than unity, as shown above, and is not easily employed in areas with little water availability.

1.4.2. Industrial applications

DRM process does not count with a large or very developed industry, since, the high production of carbon during the process is responsible for poisoning and disabling the catalysts used, which generates high costs and continual losses of the catalytic material.

The two processes that expose the application closely related to DRM in the industry are the CALCOR process and the SPARG process, both developed to prevent carbon building under drastic reforming conditions. The design of the first, the CALCOR process, aims mainly at the production of syngas with a preference for obtaining highly pure CO (H_2/CO=0.42).[8], [63] The SPARG process aims at the production of syngas with a 1/1 H_2/CO ratio that can be produced by combining SRM and DRM. Carbon formation is prevented by carrying out an S-poisoning of the catalysts, with approximately 0.7% of the catalyst coverage with sulfur, directly affecting the total catalytic decomposition of methane capacity.[60] However, as Wittich et al. [8] mention, these two processes are only feasible in certain scenarios and lack wide applicability.

1.4.3. Reaction mechanism

The initial reaction mechanism for DRM was proposed by Bodrov and Apel'baum in 1967.[62] Most recent research for the reaction mechanism is based on the *Langmuir Hinshelwood-Hougen Watson* method referred from the extensive stages published by Xu & Froment [64] in their study on Ni/MgAlO catalyst for SRM reactions.

Table 3 shows the simulated elementary steps involved in the DRM reaction calculated using density functional theory (DFT) by Zhu et al.[65] complementing the reaction mechanism proposed by different authors [66]–[68]

Table 3. Possible elementary reactions involved in DRM reaction; * is used to represent unoccupied active sites.[61], [65]

Step	Reaction Pathway
$CH_{2(g)}+*\leftrightarrow CH_4*$	CH_4 adsorption
$CH_4*\leftrightarrow CH_3*+H*$	CH_4 dissociation on metal
$CH_3*\leftrightarrow CH_2*+H*$	
$CH_2*\leftrightarrow CH*+H*$	
$CH*\leftrightarrow C*+H*$	
$H*+H*\leftrightarrow H_2*$	Desorption of H_2
$H_2*\leftrightarrow H_{2(g)}$	
$CO_{2(g)}+*\leftrightarrow CO_2*$	CO_2 adsorption
$CO_2*\leftrightarrow CO*+O*$	CO_2 direct dissociation
$CO_2*+H*\leftrightarrow COOH*$	H-assisted CO_2 activation and dissociation
$COOH*\leftrightarrow CO*+OH*$	Surface OH groups involved oxidation of adsorbed CH_x fragments and subsequent decomposition
$O*+H*\leftrightarrow OH*$	
$CH_3*+OH*\leftrightarrow CH_3OH*$	
$CH_3OH*\leftrightarrow CH_2OH*+H*$	
$CH_2*+OH*\leftrightarrow CH_2OH*$	
$CH_2OH*\leftrightarrow CHOH*+H*$	

$CH^*+OH^* \leftrightarrow CHOH^*$	
$CHOH^* \leftrightarrow COH^*+H^*$	
$C^*+OH^* \leftrightarrow COH^*$	Surface carbon hydroxylation and subsequent decomposition
$COH^* \leftrightarrow CO^*+H^*$	
$CH_3^*+O^* \leftrightarrow CH_3O^*$	Surface O atom oxidation of adsorbed CH_x fragments and subsequent decomposition
$CH_3O^* \leftrightarrow CH_2O^*+H^*$	
$CH_2^*+O^* \leftrightarrow CH_2O^*$	
$CH_2O^* \leftrightarrow CHO^*+H^*$	
$CH^*+O^* \leftrightarrow CHO^*$	
$CHO^* \leftrightarrow CO^*+H^*$	
$C^*+O^* \leftrightarrow CO^*$	
$CO^* \leftrightarrow CO_{(g)}$	Desorption of CO
$OH^*+H^* \leftrightarrow H_2O^*$	Desorption of H_2O
$H_2O^* \leftrightarrow H_2O_{(g)}$	

DRM reaction mechanism, with Ni catalysts, involves I. Adsorption of methane on active metal sites in a dissociative form to produce hydrogen and hydro-carbonate species CH_x ($0<x<4$); step typically regarded as a slow kinetic step. II. Adsorption of CO_2 on either metal Ni sites or a basic support surface to form carbonate/bicarbonate species, followed by direct CO_2 dissociation which may produce OH groups or H-assisted decomposition. III. The surface OH groups on the support react with adsorbed CH_x intermediates to yield a formate-type intermediate, which decomposes to yield H_2 and CO. The support may serve as a sink for surface hydroxyl groups, such that the active site for the formation and subsequent decomposition of CH_xO may be at the metal-support interface. IV. The CH_xO species can also be obtained by the reaction of adsorbed CH_x intermediates with O, which originates from CO_2 direct dissociation or the cleavage of OH groups; another rate-determining step.[12], [61] Although some authors disagree with the mechanism described above or with the rate-determining steps, the inconsistencies can originate from the nature of the catalysts, like particle size on Ni^0, the properties of the support, and the interaction between the metal and the support; as well from the reaction conditions applied.[61]

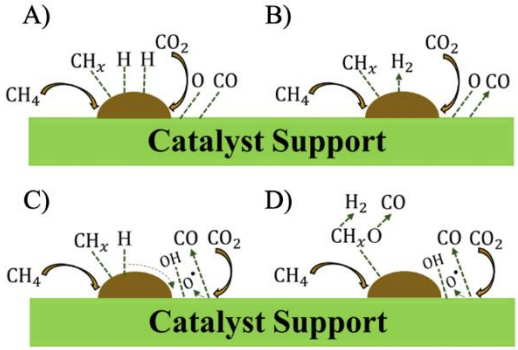

Fig. 4. Mechanistic steps for DRM adapted from Abdulrasheed et al.[12]

Fig. 4 shows a schematic of the DRM mechanism involving: A) Chemisorption and dissociation of CH_4 and CO_2, B) H_2 and CO desorption, C) hydrogen and oxygen forming surface hydroxyls, D) oxidation of hydrogen-depleted CH_x species by surface hydroxyls and oxygen groups to produce H_2 and CO.[12]

1.5. Catalysts for DRM

1.5.1. Catalytic active phase

The totality of transition metals (noble and non-noble) have been evaluated as catalysts for the DRM over critical properties like activity, stability, and selectivity; so far, it has been found that Ru, Rh, Pd, Ir, Pt, Co, and Ni are adequate metals for this process.[14] Nonetheless, these metals, according to their characteristics, present different performances, and some authors have classified some according to their activity and especially according to their susceptibility to the formation of carbon on their surfaces.

Zhao et al. [69] expose works carried out in the kinetic analysis of reforming of methane, capable of being extrapolated to the DRM process, over more than 10 transition-metal surfaces by applying a linear scaling relationship between the binding energies of selected molecular fragments, and the binding energies of intermediates as well as of transition states that occur in the reforming process; the reaction rate can be mapped to a two-dimensional curve, defined by the binding energy of C and O in the study.[8], [69] As shown in **Fig. 5.**, the theoretical calculations predict that the reforming activity decreases in the sequence Ru > Rh > Ni > Ir > Pt ≈ Pd.

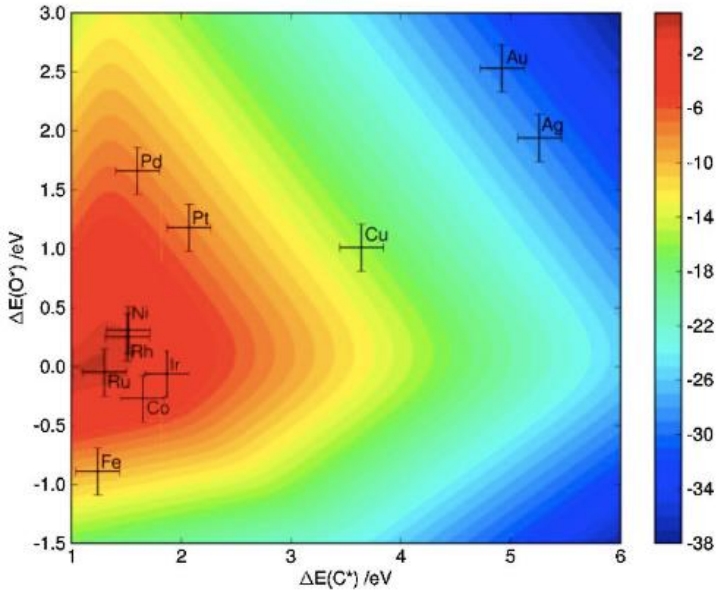

Fig. 5. Two-dimensional volcano-curve of the turnover frequencies (log 10) as a function of O and C adsorption energy. T=500ºC, p=1atm. [8], [69]

Table 4. shows how some metals have been sequenced according to their experimental catalytic activity, where Ru, Rh, and Ni are metals that stand out because of their high performance as active phases it is reported that comparing the dissociation of methane over several metals, the lowest dissociation enthalpies are obtained using these three elements.[70], [71] Aramouni et al. [72] argued that the differences between noble and non-noble metals rest in the ability of noble metals to disperse on surfaces and retain a small particle size; a desirable feature that prevents carbon formation.[73]

However, evaluating costs and materials availability, it is more economical to use Ni as the active phase, even though Ni is one of the metals that has the greatest susceptibility to carbon formation (see **Table 3.**).[58] Thus, some publications seek to present the use of bimetallic active phases that add a noble metal to a main metallic active phase, creating an alloy that provides the advantages of noble metals and also reduces costs.[74]

Table 4. Performance of metals used as catalysts for DRM.

A sequence of activities (from highest to lowest activity)	**Ni**>Ru>Rh>Pt>Pd	[14]
	Ru>Rh & **Ni** >Ir>Pt>Pd	[75]
Carbon deposition (from highest to lowest)	**Ni**>>Rh>Ir=Ru>Pt≅Pd	
	Ni>Pd=Rh>Ir>Pt>>Ru	[14]

On the other hand, the metal used in the reaction has a characteristic activity not only because of its chemical characteristics but also because of other characteristics like the crystal structure. Beebe et al. [76] expose that the activity of the Ni (110) is greater than the activity of Ni (100), and in turn, the activity of the former is greater than the Ni (111) activity for the CH_4 decomposition. To explain this influence of the metal structure on the activity, Bradford et al. [62] state that it may be a consequence of the geometric size distribution of each of the structures on the metal surface, based on theoretical studies that expose that CH_x species are preferably located on the metallic surface that completes their tetravalence.

1.5.2. Catalytic support

The metal is embedded in different materials to obtain supported metal catalysts, on which the support plays an important role in dispersing active phases, promoting, stabilizing, and in some cases, becoming part of active sites. For the specific case of the DRM process, the support used must meet the following characteristics: I) A high Lewis basicity, which increases the ability of the catalyst to chemisorb CO_2, making it available for the reforming reaction and its possible reaction with deposited carbon; II) a strong metal-support interaction, which prevents sintering of the metal and, for example, hinders the reduction of Ni^{2+} to Ni^0, resulting in small metal particles on the catalyst surface; a very important aspect given that carbon absorbed on the smaller metal particles diffuses with more difficulty than on the large particles. Finally, III) a high porosity/surface area to ensure high dispersion of the active phase. [10], [12], [14]

Wang & Ruckenstein [71] studied the catalytic activity of Rh catalysts (0,5 wt%) supported on different materials: reducible oxides (CeO_2, Nb_2O_5, Ta_2O_5, TiO_2, and ZrO_2), and non-reducible oxides (Al_2O_3, La_2O_3, MgO, SiO_2 and Y_2O_3), under the reaction conditions

(catalyst: 20,0mg; flow rate: 20mL·min^{-1}; CH_4/CO_2=1/1; space velocity: 60000 mL·h^{-1}·g^{-1}, T = 800ºC); the conversion rates of CH_4 and CO_2 were dependent on the support employed. Further, the authors were able to determine that the catalysts supported by non-reducible oxides (γ-$Al_2O_3 \approx MgO > Y_2O_3 > SiO_2 \approx La_2O_3$; ordered from higher conversion rates to lowest) generally led to higher conversion rate and H_2/CO ratio than their reducible counterparts.

Alumina and magnesia are two of the most studied supports for nickel catalysts.[8], [12], [16] Alumina is relatively cheap, offers a high specific surface area, and possesses high thermal stability. Magnesia has a high Lewis basicity, a beneficial effect since CO_2 adsorption is enhanced on basic supports, and lies in the possibility of forming a NiO-MgO solid solution at any molar ratio due to the similar ionic radii of Mg and Ni cations and particular lattice parameters, resulting in increased metal-support interaction.[77] Reasons why, MgO-Al_2O_3 materials are promising supports for the preparation of Ni catalysts for DRM.[78]

These Mg(Al)O mixed oxides can be obtained through the thermal decomposition of hydrotalcite-like mixed layered hydroxides (HTs) or also called layered double hydroxides (LDHs); a large group of naturally obtained minerals and synthetic materials that possess the typical layered structure of hydrotalcite, which general formula can be represented as **Eq. 7**:

$$[{M^{2+}}_{1-x}{M^{3+}}_{x}(OH)_2][\left({A^{n-}}_{\frac{x}{n}}\right) \cdot mH_2O] \qquad (7)$$

Where M^{2+}, M^{3+} are di- and tri-valent cations; A are interlayer anions; and the x-mole fraction of trivalent cations. The $[{M^{2+}}_{1-x}{M^{3+}}_{x}(OH)_2]$ describes the composition of brucite-like layers and $[\left({A^{n-}}_{\frac{x}{n}}\right) \cdot mH_2O]$ describes the composition of interlayered spaces.[77], [79], [80]

For these kinds of systems, Ni can be incorporated by different means. However, the most commonly applied procedure for the preparation of Ni-containing HTs-derived materials is the co-precipitation, with controlled pH, of the different cations present in a solution of their corresponding nitrates, obtaining a mixed hydroxide structure where Ni has been introduced in the brucite-like layers.[81] Additionally, other known methods consist in the incorporation of Ni (or even various catalytic promoters) into the interlayer space of the HTs structure by the reconstruction method, through memory effect, or via ion exchange.[20], [77], [82], [83] For synthesis planning, publications like Debek et al. [84] expose that in Ni-Mg/Al HTs-derived type catalysts for DRM, the amount of active phase affects the catalytic performance, and with loads between 2.79 and 58.66% the greatest performance was obtained with catalysts of a nominal Ni wt. % close to 25%; thanks to its high content of possible active sites, moderate Ni^0 crystal size, and stability. Although some authors suggest a higher coke production during DRM with catalysts with Ni wt.% load greater than 15 or 20%. [23], [80], [85]

Regarding the Ni/Mg and M^{II}/M^{III} ratios, their influence is reflected in the activity and stability of the HTs-derived catalysts. For this reason, compendiums of scientific research are taken into account, where results from authors indicate the high catalytic efficiency of materials with 1 to 5 Ni/Mg ratios and M^{II}/M^{III} ratios of 2 and 3.[58], [83] Since these are

primary stable materials, that exhibit reduction temperatures close to the suggested temperatures for catalytic testing (700ºC) and have a high content of basic sites.

Besides, the catalytic performance of the mixed oxides obtained from the calcination of the HTs precursors depends on a great variety of factors, not only the already mentioned methods of synthesis of the precursors, the added load of Ni (active phase), and the M^{II}/M^{III} ratios; but the promoter load if it is employed or not, the temperature for thermal decomposition to obtain the mixed oxides and others.[12]

1.5.3. Ceria promoted catalysts

The function of the chemical promoters is to present new, supplementary active sites or to reinforce the chemical properties relating to the reactivity of the catalyst such as basicity and redox properties. The addition of promoters can aid in the reduction of carbon deposition and sintering, as well as the oxidation of carbonaceous species, resulting in an improved catalyst.[86]

Cerium is a versatile and important rare earth element that has been involved in many areas of heterogeneous catalysis for several years, given that is the most reactive element of the lanthanide series. Its oxide, CeO_2, named ceria, has a fluorite structure, FCC, where each Ce cation is surrounded by eight oxygen atoms and the coordination number of the oxygen atom is four.[86]–[88] CeO_2 promotes metal dispersion in comparison with conventional supports such as Al_2O_3.[89] In addition, ceria has a wide technological application in the field of catalysis because of its environmental friendliness, surface defects, excellent redox ability, remarkable oxygen storage capacity, and release ability.[23], [86], [90], [91]

The ability of ceria to release oxygen under a reducing environment and store oxygen under oxidizing atmosphere causes the formation and filling of oxygen vacancies; this stability and diffusivity of O-vacancies play a crucial role in the physical and chemical properties of the catalyst.[15] In DRM catalysts the presence of oxygen vacancies serves as sites for CO_2 activation and C-O bond cleavage, thereby increasing the pool of O atoms on the catalysts surface; and mobile oxygen species also reduce the chance of catalyst deactivation due to carbon accumulation by oxidizing surface carbon to CO.[12]

Authors like Shamskar et al.[92] explored the effect of CeO_2 loading in Ni/Al_2O_3; where the formation of carbon and the sintering of active sites were diminished using different CeO_2 contents (1, 3, and 5 wt.%), introduced to Ni 25 wt.%/Al_2O_3 by ultrasonic co-precipitation technique. The results disclosed that a small amount of CeO_2 (1 wt.%) enhanced the performance of the catalyst due to Ni^0 dispersion improvement; however, the 3 and 5 wt.% CeO_2 content covered the active sites and reduce the catalyst's performance. In contrast, Chein & Fung [93]reported the effects of 5, 10, and 15 wt.% of CeO_2 loading added to 10wt.% Ni/Al_2O_3 by wetness impregnation, and it was reported that for a DRM process, the optimal addition was 5 wt.% CeO_2, which increased the catalytic performance due to uniform Ni dispersion and the formation of $CeAlO_3$, enhancing the ability to resist carbon deposition during the reaction.

For Ni/MgO catalysts Khajenoori et al.[94] explored a 7 wt.% CeO_2-promoted catalyst synthesized by subsequent impregnation of Ni (5, 7, 10, and 15 wt.%)/MgO catalysts with cerium nitrate. The Ni 10wt.% - CeO_2 7 wt.% /MgO catalyst exhibited superior DRM performance and high resistance to coke formation, attributed to the effective exchange of oxygen species and dispersion of active sites.

Taking into account the performance of Ni catalysts on Al_2O_3 and MgO supports promoted with Ce, authors like Daza et al. [95]–[98], Ren et al. [88] and Dębek et al. [91], [99] have published the use of Ni/Mg/Al catalysts derived from HTs promoted with Ce for the DRM process, synthesized by different methods such as co-precipitation in the presence of complexes like $[Ni(EDTA)]^{2-}$ and $[Ce(EDTA)]^{-}$, reconstruction again in the presence of $[Ce(EDTA)]^{-}$, and impregnation of the promotor after obtaining the HTs, among others. However, the simplest and most widely used method to obtain Ni/Mg/Al HTs-derived catalysts is still the co-precipitation method, with which the promoter can also be added.

Table 5. shows a short compendium of Ce-promoted Ni/Mg/Al catalysts, derived from HTs, obtained by co-precipitation only at constant pH, designed and exposed to the DRM process. From these references, in general, the amount of Ce introduced did not have much significant influence on CH_4 and CO_2 conversions and H_2/CO molar ratio; nonetheless, it influenced the formation of carbon deposits. Recognizing that their performance may depend on the amount of Ce loaded and the method of introducing the promoter.

Table 5. Ni/Mg/Al HTs-derived mixed oxides promoted with Ce catalysts tested for DRM process.

HTs Synthesis	Ce Introduction Method	Ni content	Ce content	Calcination Conditions	Catalytic Test	Ref.
Co-precipitation at pH = 10.5	At the co-precipitation stage in the form of Ce^{3+} cations	48.03wt% NiO	14.90 wt.% (CeO_2)	500ºC – 16h	700ºC , GHSV = 48,000ml·g^{-1}·h^{-1}, CH_4/CO_2/He 20/20/60, 1h of previous reduction H_2	[95]
Co-precipitation at pH = 10.5	At the co-precipitation stage in the form of Ce^{3+} cations	~ 2 Mg/Ni	26.90 – 9.40 – 4.29 – 1.78 (Al/Ce)	500ºC – 16h	500-700ºC, GHSV = 30-40L·g^{-1}·h^{-1}, CH_4/CO_2/Ar 5/5/40, 1h of previous reduction H_2 at 700ºC	[28]
Co-precipitatio	At the co-precipitati	20 wt.%	0.1 – 0.2 –	650ºC – 4h	750ºC, GHSV =	[88]

n at pH = 8-9	on stage in the form of Ce^{3+} cations		0.3 – 0.5 (Ce/Al)		53,200ml·g^{-1}·h^{-1}, CH_4/CO_2 1/1, 2.5h of previous reduction H_2 at 700ºC	
Co-precipitation	At the co-precipitation stage in the form of Ce^{3+} cations	10 – 25 wt.%	5 wt.% (CeO_2)	650ºC – 5h	650ºC, CH_4/CO_2 1,5/1, 1h of previous reduction H_2 at 750ºC	[23]
Co-precipitation at pH = 9	At the co-precipitation stage in the form of Ce^{3+} cations	12 – 20 –40 wt.%	4.7 – 8.8 – 4.2 wt.%	600ºC – 6h	500 – 800ºC, GHSV = 144,000ml·g^{-1}·h^{-1}, 6h of previous reduction H_2/N_2 at 600ºC	[85]

1.6. Structured catalysts as monoliths

Process intensification has garnered growing research interest in recent decades. By employing advanced reactor designs and/or combining them with separation techniques, reaction engineering, which is fundamental to most chemical production processes, has the potential to revolutionize the chemical and energy sector.[100], [101] The idea of structured reactors and catalysts started its foundation in 1995 at the pioneering seminar on monolithic catalysts in St. Petersburg, and then it was developed through a successive conference called International Conference on Structured Catalysts and Reactors (ICOSCAR).[100]

The term monolith is applied mostly as a support of a catalytically active component or as a catalyst if the catalytic component is an integral part of the monolith structure.[101] The monolithic supports are uni-body structures composed of interconnected repeating cells or channels and are most commonly composed of ceramic, metal, or silica material for reforming processes.[102]–[105] However, many inorganic catalysts support materials used today in conventional chemical and refining applications can be extruded into a monolith form, and this has ignited interest in monolith reactors as potential replacements for fixed bed and slurry reactors.[26]

Monolith catalysts or monolith reactors have some common features in most of the applications they are used for I) low-pressure drop under high fluid throughputs, II) elimination of external mass transfer and internal diffusion limitations, III) low axial dispersion and back mixing, IV) larger external surface, V) uniform distribution of flow (gas

phase), VI) elimination of fouling and plugging, meaning extended catalyst lifetime, and VII) easy scale-up.[26], [106]

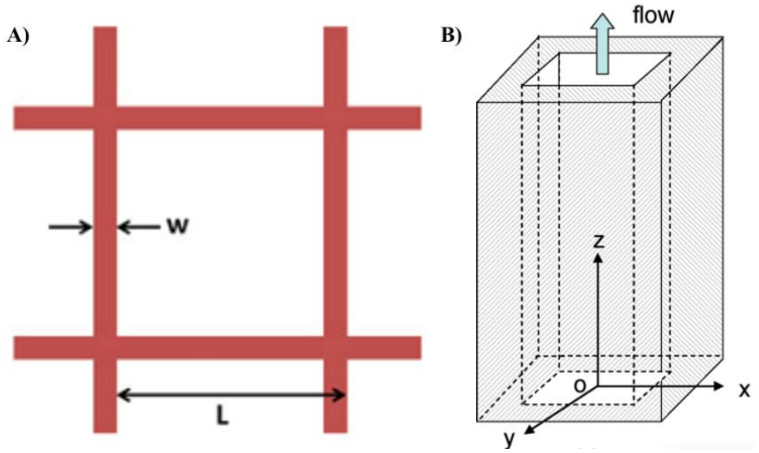

Fig. 6. Schematic representation of a single square monolith channel A) transversal section with parameters employed to characterize the monolith geometry, B) 3D representation.[106]

Honeycomb monoliths are distinguished by channels, which can have various geometries and can be of two types: wall-flow, where the channels alternately close and the stream is compelled to flow through the porous wall, or flow-through, in which every channel is open on both sides.[100] Monolith channels or cells may be hexagonal, rectangular, or square, the most commonly used cells.[101] In the case of the square-channel monoliths, the monolith geometry is fully defined by two parameters (**Fig. 6.**): the channel size or repeat distance (L), and either the wall thickness (w) or cell density (N, **Eq. 8**), which is defined as the number of cells per square inch (cpsi).[26] Parameters that in return allow the calculation of the open frontal area (OFA, **Eq. 9**) and the geometric surface area (GSA, **Eq. 10**); the sum of the areas of all the channel walls upon which the catalyst is deposited. Where the first mentioned, exposes one of the most important advantages of the monoliths, given that the generally large OFA obtained by these structures, leads to very little resistance to flow, low back pressure on the system, and hence low-pressure drop, meaning lower energy loss.[102]

$$\mathrm{N\ (cpsi)} = \frac{1}{L^2} \quad (8)$$

$$\mathrm{OFA} = \frac{(L-w)^2}{L^2} \quad (9)$$

$$\mathrm{GSA} = \frac{4*(L-w)}{L^2} \quad (10)$$

$$\mathrm{D} = 4\frac{OFA}{\mathrm{GSA}} \quad (11)$$

The pressure drop across the monolith depends linearly on flow velocity and length [26], [102]. In **Eq. 12.** f is the friction factor, dimensionless; G is the gravitational constant; D is

the hydraulic diameter of the honeycomb channel (cm) defined in **Eq. 11.**; l this e monolith length (cm); v the velocity in the channel ($cm \cdot s^{-1}$); and ρ the gas density ($g \cdot cm^{-3}$):

$$\Delta P = \frac{2 f l \rho v^2}{G D} \quad (12)$$

Fig. 6. Shows the 3D structure of a square channel with *x* and *y* coordinates representing the cross-sectional direction and *z*-axis representing the fluid flow direction. When the monolith has a catalyst-wash coated wall, only a very thin layer is catalytically active, and in these cases, the reaction is considered to be occurring only at the monolith wall surface without any internal molecular diffusion effect.[106] The wash coat thickness (⌜) represents the channel configuration.

Chen et al.[106] and Cornejo et al.[107] explain that monolith channels involve only mass, heat, and momentum transport, excluding homogeneous reactions. Due to the narrowness of the channel, laminar gas flow is common. Reactant molecules diffuse from the channel to the monolith wall or wash coat layer for reactions, while product molecules diffuse in the opposite direction. Exothermic processes transfer heat from the wash coat layer to the gas through conduction and radiation at high temperatures, while endothermic reactions transfer heat from the gas to the monolith wall.

Understanding the complexity of the interactions between different physical and chemical processes taking place within monolith channels and in the channels, walls can be aided by detailed modeling and simulation. Authors have proposed and discussed studies on modeling and simulation of gas phase/monolith reactors with a focus on mass and heat transfer, dynamic modeling, gas flow uniformity, and chemical kinetics effects on monolithic performance.[106]–[109]

1.6.1. Obtaining structured catalysts in monoliths

Fig. 7. Shows a schematic representation of the different paths leading to monolithic catalysts, the route that should be taken toward the preparation of the system strongly depend on the application and the catalyst.[110]

One path is when the catalyst has sufficient mechanical strength and can be extruded with some binder materials in a monolithic shape, recommended for applications in which the catalyst efficiency is less important and a large number of catalysts is preferred; another path involves the coating of a bare monolithic structure with a catalyst support material (alumina, silica or carbon), a procedure commonly called wash coating, followed by the application of the catalytic active phase with different strategies: impregnation, ion exchange, deposition-precipitation, among others.[25], [111], [112] The last path to obtain monolithic catalysts depends on ready-made catalysts or pre-catalysts systems that do not need specific support, such as zeolites or hydrotalcites, and can be coated or synthesized directly on a monolith body.[110]

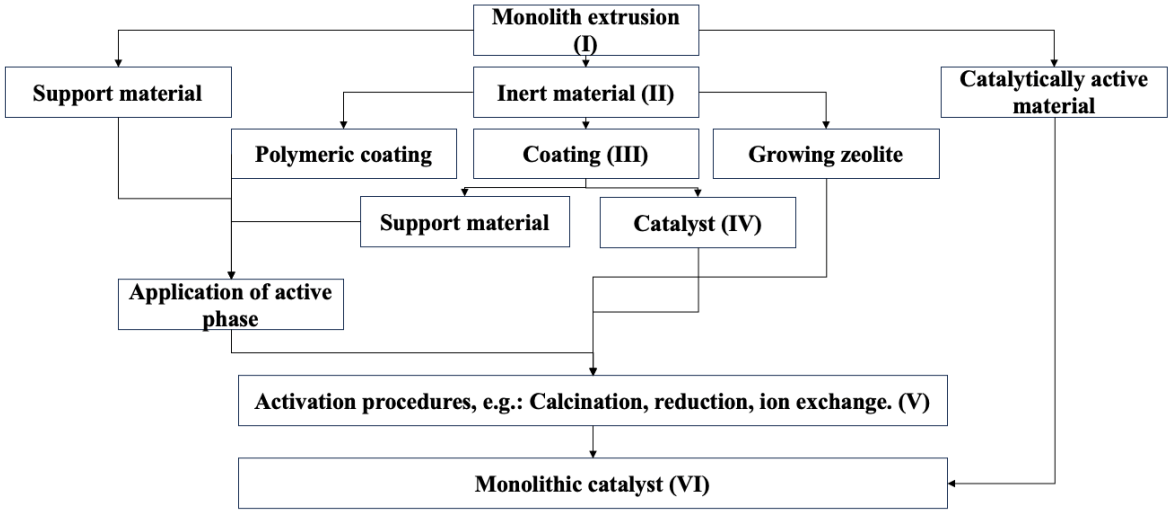

Fig. 7. Different paths towards obtaining monolithic catalysts.[110]

In the wash coating method (Fig. 7, steps I to VI), the catalytic system is coated onto the monolith and activated before catalytic testing. The monolith serves as a secondary support, anchoring the active phase-catalytic support structure. The main support offers increased interaction, stabilizing and dispersing the active phase. Both the synthesis and monolith coating processes hold equal importance due to the significance of the catalytic system and monolithic structure.[25]

Various catalyst application methods impact the surface characteristics of the resulting material, including coating layer thickness, homogeneity, and other factors, directly influencing the final solid's catalytic performance.[110] Consider the base material for coating with the active phase support. Common methods for ceramic monoliths include colloidal coating, sol-gel, and slurry coating (**Table 6**). Metallic monoliths need modified approaches due to their low porosity, necessitating higher metal oxide concentrations or pre-coating chemical-physical treatment.[110], [112]

Table 6. Monolith coating methods.[25], [110], [113]

Method	Characteristics
Colloidal coating	It is a pore-filling technique using nanoparticles that can be obtained by different processes. This method is recommended for highly active catalysts, and it can cause a small decrease in the open front area.
Sol-gel coating	Sol-gel involves a dispersed form of colloidal solution, formed by interlinked particles during gelation. The process includes preparing a sol, coating the monolith, and calcining it, resulting in improved pore filling compared to traditional colloidal coating
Slurry coating	The procedure entails dipping the monolith in a catalyst solution (slurry), removing excess liquid with compressed air, and then drying and calcining. This method reduces the open frontal area, allows high loading, and works well for low-activity catalysts.

1.6.2. Immobilized catalysts in monoliths for DRM

Despite the different improvements that are proposed for DRM catalysts, such as the study of different metals as active phase, the use of supports with the appropriate characteristics, the application of promoters that improve the catalytic performance and do achieve greater stability against sintering and coke deposition; still the need to propose more tools to achieve catalytic systems efficient enough to scale the reforming method to an industrial environment mentioned in publications.[12], [15], [114], [115]

For this reason, and having in mind the disadvantages of the powdered (for fix bed reactor) catalysts such as high-pressure drops during the process, poor heat transfer, and difficult operational management.[116] Special attention has been paid to the development and evaluation of monoliths for their implementation in DRM catalytic systems since different monolithic structures have been successfully used in recent years for reactions that include catalytic combustion for power generation, the selective oxidation of alkanes, and even CO_2 methanation.[12], [117] All thanks to the properties that monolithic structures offer, mentioned above. To discuss some of the publications on DRM, it may be convenient to classify the monoliths reported according to their material type. Among the research, different monoliths built of aluminum, stainless steel, silicon carbide, silica, and cordierite ceramic material were found.

1.6.2.1. Metallic monoliths

The use of metallic monoliths is appreciated because these materials have a low-pressure drop, high cell density, and great heat transfer. These monoliths can be obtained from iron, stainless steel, nickel, chromium, and aluminum, among others; and the structures are commonly obtained by corrugation, although later a method of laser sintering (3D printing) is presented.[101]

Aiming to obtain a catalyst resistant to the sintering of the active phase and the deposition of carbon, Du et al.[118] synthesized a unique monolithic Ni-catalyst using in situ hydrotalcite nanolayers on aluminum wires. This catalyst features porous nanosheets that prevent coke deposition and sintering, chemical bonds between mixed oxide support and aluminum substrate for stability, high Ni nanoparticle dispersion, and strong basic sites. The monolithic catalyst displayed stronger metal-support interaction and higher basicity than the traditional powdered Ni-MgO-Al_2O_3 catalyst. These characteristics resulted in good catalytic activity with less active phase, high stability, and three times less coke formation on the surface.

Agueniou et al.[104] evaluated a Ni/CeO_2-ZrO_2 catalyst in a stainless-steel honeycomb monolith obtained by 3D printing. The structured catalyst achieved nearly 100% CO_2 conversion at 900ºC, with no significant deactivation and high heat transfer. Compared to a cordierite monolith with the same active phase and support [119], the stainless-steel catalyst showed better performance at 900ºC, surpassing CH_4 and CO_2 conversion and achieving an H_2/CO ratio greater than 0.90. The authors emphasized the option of future projects in which the implementation of the active phase is involved in the construction of the monolith, since

its synthesis by 3D printing allows the modification and mixing of different metals, however, the load of Ni in the monolith must be optimal to avoid high carbon formations.

1.6.2.2. Silicon carbide and silica monoliths

Silicon carbide monoliths offer thermal and mechanical properties suitable for harsh reaction conditions. Their chemical inertness and high surface area can be easily prepared commercially with good physicochemical properties at a reasonable cost.[120]

Liu et al.[105], considering the excellent performances of Ni as active phase and SiC as support, synthesized and evaluated the activity of Ni catalysts supported on monolithic SiC foam and the effect of different Ni charges (1, 3, 5, 7, 9, and 11wt%). They exposed as a result that the catalyst that contained a Ni 7wt% (surface area = 4.4 m^2 / g) presents the best catalytic efficiency, giving CH_4 and CO_2 conversions of 93% and 95% respectively with low amounts of deposited carbon; values that were stable during 100h of catalytic performance.

Gao et al.[121] designed a silicon carbide foam monolith coated with carbon nanofibers (CNFs) as support for Ni-based catalysts. The Ni/CNFs-SiC catalyst showed highly dispersed Ni particles and excellent stability under DRM conditions at 750ºC for 100 hours. It outperformed a Ni/SiC "comparison" catalyst, indicating the potential to prevent sintering and coke formation, making it a promising DRM catalyst.

Daoura et al.[122] designed a stable Ni-silica (Ni @ SBA15) catalyst using the sol-gel one-pot method and compared it with a Ni/SBA15 catalyst prepared by impregnation. The Ni@SBA15 catalyst showed higher activity and selectivity, along with superior stability even at 923K with 0% conversions of CH_4 and CO_2 after 4h of DRM exposure. The excellent distribution of 3nm nickel nanoparticles and their strong interaction with silica contributed to the catalyst's stability and limited coke formation and sintering.

1.6.2.3. Cordierite monoliths

In the industry, synthetic cordierite ceramic monoliths find importance for exhaust gas treatment in internal combustion engines and catalytic converters.[25], [123] Cordierite offers: I) thermal shock resistance from low thermal expansion, II) suitable porosity and pore size distribution for wash coat application and adherence, III) sufficient refractoriness (melting point over 1450ºC), IV) enough strength for harsh environments, and V) compatibility with mixed oxide wash coat and catalysts.[26]

Some authors such as Luisetto et al.[103] implemented this material for DRM using a catalyst where the active phase is Ni and Ru as promoter supported on γ-Al_2O_3. This catalytic system presented higher conversions than those obtained by an unstructured catalyst, and presented low formation of carbon filaments, the authors concluded that a better coating of the monolithic structure would further increase the operating time of the system.

Leba & Yildrim [115] studied catalytic activity in DRM using different Ni-Co catalyst forms: Ni-Co impregnated in MgO, MgO-covered monoliths, MgO nanorods in monolithic structure, and $Ni0.5Co_{2.5}O_4$ nanowires in monoliths. The best results were achieved with 8wt% Ni and 2wt% Co on MgO-covered cordierite monolith, showing high activity, low carbon formation, and stable performance for 48h. Comparing structured catalyst (83% CH_4 and 89% CO_2 conversion) with unstructured particulate catalyst (70% CH_4 and 80% CO_2 conversion), the superiority of the structured catalyst on cordierite was evident, with an H_2/CO ratio of 0.95, close to the ideal value.

Agueniou et al. [119] compared $Ni/CeO_2/ZrO_2$ catalysts on honeycomb cordierite vs unsupported catalysts. The structured catalysts achieved over 90% CO_2 and close to 90% CH4 conversion at 750ºC, nearing thermodynamic limits [124]. In contrast, the powdered catalysts showed lower conversions at 1023K, with CH_4 at 40% and CO_2 at 53%.

1.7. Background

Table 7. summarized different relevant reports of Ni-based catalysts immobilized in cordierite monoliths employed for the DRM process.

Table 7. Main information on obtaining, catalytic evaluation conditions and performance of different monolithic catalysts reported for DRM. AP: active phase, P: promoter, PR: pre-reduction, RC: reaction condition.

Active phase/ Promoter	Catalytic support	Structured catalyst obtention method	DRM conditions	CH_4 conversion (%)	CO_2 conversion (%)	H_2/CO	Carbon deposition	Ref.
AP: Ni P: K_2O, Na_2O, Li_2O, La_2O_3	Al_2O_3	Slurry coating/Impregnation (Monolith specific surface: 0.45 $m^2 \cdot g^{-1}$)	PR: H_2-700ºC, 2h. RC: CH_4/CO_2/Ar, 100-750ºC, 6000 GHSV (h^{-1}),	80% with 8.2%Ni/11.2%Al_2O_3 at 480ºC, 3.8%Ni/11.2%Al_2O_3 at 492ºC and 1.0%Ni/2%Al_2O_3 at 533ºC. At 700ºC Ni/Al_2O_3/K_2O: >80%, Ni/Al_2O_3/Na_2O:85%, Ni/Al_2O_3/Li_2O:65%, Ni/Al_2O_3/La_2O_3:80-90%.	_	_	_	[125]
AP: Ni ~10wt.%	Al_2O_3-MgO	Sol-gel coating	PR: H_2-600ºC, 10h. RC: 60mL/min flow $CH_4/CO_2/N_2$, 600ºC, 40h.	45-17% if calcinated at 450ºC. 64-40% if calcinated at 650ºC.	_	1.1-2.7 if calcinated at 450ºC. 1.1-1.4 if calcinated at 650ºC	_	[126]

AP: Ni 10.1 or 12.0 wt.% P: Ru 0,6 wt.%	Al_2O_3	Washcoating/Impregnation	PR: H_2-800ºC, 1h. RC: 134 or 169 GHSV ($cm^3 \cdot g^{-1} \cdot h^{-1}$), $CH_4/CO_2/N_2$:45/45/10 vol.%, 800ºC, 70h.	25-60% for Ni/Al_2O_3. 78-60% for $Ni-Ru/Al_2O_3$.	40-70% for Ni/Al_2O_3. 85-75% for $Ni-Ru/Al_2O_3$.	0.6-0.9 for Ni/Al_2O_3. 0.9 for $Ni-Ru/Al_2O_3$.	Ni/Al_2O_3 : 86.04 wt% of carbon content in the final monolith. $Ni-Ru/Al_2O_3$: 32.82 wt% of carbon content in final monolith	[103]
AP: Ni 19.1 wt.%	20% CeO_2-80% ZrO_2	Slurry coating (Monolith with 230 cpsi)	PR: H_2-600ºC, 2h. RC: 115, 231, or 346 WHSV ($L \cdot g^{-1} \cdot h^{-1}$), CH_4/CO_2:1/1, 750-900ºC, 20-40h.	At 750ºC WHSV 115: 80-90% WHSV 230: 85-90% WHSV 345: 85%	At 750ºC WHSV 115: ~90% WHSV 230: >90% WHSV 345: 90%	For all 0.85-0.89.	_	[119]
AP: Ni 4.5 wt.%	CeO_2-ZrO_2 18/82 molar ratio	Slurry coating (Monoliths whit 230 and 400 cpsi)	PR: H_2-600ºC, 2h. RC: 115, 231, or 346 WHSV ($L \cdot g^{-1} \cdot h^{-1}$), CH_4/CO_2:1/1, 750-900ºC, 20-40h.	At 700ºC, Monolith with 230 cpsi: WHSV 115: 77% At 750ºC, Monolith with 230 cpsi: WHSV 115: 89% after 43h. WHSV 231: 90% after 48h. WHSV 346: 85% stable.	At 700ºC, Monolith with 230 cpsi: WHSV 115: 84% At 750ºC, Monolith with 230 cpsi: WHSV 115: 93% after 43h. WHSV 231: 94% after 48h.	For all 0.78-0.94.	_	[127]

				At 800ºC, Monolith with 230 cpsi: WHSV 115: 89% At 900ºC, Monolith with 230 cpsi: WHSV 115: 94% At 700ºC, Monolith with 400 cpsi: WHSV 115: 73% At 750ºC, Monolith with 400 cpsi: WHSV 115: 83% after 48h. At 800ºC, Monolith with 400 cpsi: WHSV 115:93% At 900ºC, Monolith with 400 cpsi: WHSV 115: 98%	WHSV 346: 90% stable. At 800ºC, Monolith with 230 cpsi: WHSV 115: 93% At 900ºC, Monolith with 230 cpsi: WHSV 115: 96% At 700ºC, Monolith with 400 cpsi: WHSV 115: 81% At 750ºC, Monolith with 400 cpsi: WHSV 115: 89% after 48h. At 800ºC, Monolith with 400 cpsi: WHSV 115: 96% At 900ºC, Monolith with 400 cpsi: WHSV 115: 99%			
AP: Ni 8wt.% - 2wt.% Co	MgO	Washcoating/Drop by drop impregnation	PR: H_2-800ºC, 1h. RC: 84000 WHSV ($mL \cdot g^{-1} \cdot h^{-1}$),	At 600ºC: 45% At 650ºC: 60% At 700ºC: 75% At 750ºC: 90% At 800ºC: 95% At 750ºC for 8h: 85%	At 600ºC: 55% At 650ºC: 70% At 700ºC: 85% At 750ºC: 95% At 800ºC: close to 100%	At 600ºC: 0.8 At 650ºC: 0.85 At 700ºC: 0.9	_	[115]

			CH_4/CO_2:1/1, 600-800ºC and 750ºC for 8h. 3% feed O_2 addition	At 750ºC for 47h, 3% feed O_2 addition: close to 90%	At 750ºC for 8h: 89% At 750ºC for 47h, 3% feed O_2 addition: close to 85%	At 750ºC: >0.9 At 800ºC: >0.9 At 750ºC for 8h: 0,95 At 750ºC for 47h, 3% feed O_2 addition: 0.97		
AP: Ni	Al_2O_3	Sol-gel washcoating/Impregnation (Systems calcinated at 800ºC for 4, 10, and 20h)	PR: H_2-800ºC, 13h. RC: 102857 GHSV ($mL \cdot g^{-1} \cdot h^{-1}$), CH_4/CO_2: 1, 1.5, 2, 800ºC, 40h.	For CH_4/CO_2 ratio of 1: All systems: >90% For CH_4/CO_2 ratio of 1.5: Systems calcinated 4 and 10h: 60-50% Systems calcinated 20h: 69% For CH_4/CO_2 ratio of 2: Systems calcinated 4 and 10h: 40% Systems calcinated 20h: close to 45%	For CH_4/CO_2 ratio of 1: All systems: 99-80% For CH_4/CO_2 ratio of 1.5: Systems calcinated 10 and 20h: 90-80% Systems calcinated 4h: 70% For CH_4/CO_2 ratio of 2: Systems calcinated 4 and 10h: 99-70% Systems calcinated 20h: 90-85%	For CH_4/CO_2 ratio of 1: All systems: 0.85-0.95 For CH_4/CO_2 ratio of 1.5: Systems calcinated 10 and 20h: 0.9-0.95 Systems calcinated 4h: 1-1.1 For CH_4/CO_2 ratio of 2:	Deposition of carbon defective/amorphous filamentous, low amount of graphitic carbon.	[128]

						Systems calcinated 4 and 10h: 0.95-1.1 Systems calcinated 20h: 0.9		
AP: Ni	10wt.% CeO_2-90wt.% Al_2O_3	Sol-gel washcoating/Impregnation	PR: H_2-800ºC, 13h. RC: CH_4/CO_2: 1, 1.5, 2, 800ºC, 40h.	For CH_4/CO_2 ratio of 1: 90% For CH_4/CO_2 ratio of 1.5: 80-60% For CH_4/CO_2 ratio of 2: 50-45%	For a CH_4/CO_2 ratio of 1: 90-60% For CH_4/CO_2 ratio of 1.5: 100-70% For CH_4/CO_2 ratio of 2: 100-75%	For CH_4/CO_2 ratio of 1: 0.8-1.1 For CH_4/CO_2 ratio of 1.5: 0.9-1.1 For CH_4/CO_2 ratio of 2: 0.9-1.2	Formation of carbon nanotubes	[129]

2. HYPOTHESIS

The use of Ce-promoted mixed oxides as catalysts for DRM is a promising option because of their physicochemical characteristics, especially stability against deactivation by carbon formation. These mixed oxides can be obtained from synthesized hydrotalcites by simple methods, such as co-precipitation, which ensures good dispersion of the active phase and easy addition of the chosen promoter.

Monolithic systems, belonging to the so-called structured systems, have been proposed as alternatives to granulated catalysts. The immobilization of mixed oxides promoted by Ce, designed for DRM, on cordierite monoliths can be a favorable strategy for the same reforming process, taking advantage of the qualities of the monolithic structures and translating into a possible improvement in catalytic performance and stability.

Owing to their ease of handling and thermal stability, mixed oxides immobilized in monolithic cordierite structures can represent catalytic structures with reuse potential when used in the DRM process, subsequent calcification for removal of carbon formed during reforming, and their use in a new DRM process.

3. OBJECTIVES

3.1. General Objective

To study the performance of Ni-Ce/Mg-Al catalysts immobilized in monoliths for dry reforming of methane.

3.2. Specific Objectives

3.2.1. To study the effect of different Ce loads in the catalyst.
3.2.2. To compare the activity, selectivity, and stability of the powder catalysts with the catalysts structured in cordierite monoliths.
3.2.3. establish possible scaling of structured catalysts by determining their reusability.

4. METHODOLOGY

4.1. Synthesis of catalysts

4.1.1. Chemicals and materials

Mixed oxide precursors: aluminum nitrate ($Al(NO_3)_3 \cdot 9H_2O$, 95% purity), nickel nitrate ($Ni(NO_3)_2 \cdot 6H_2O$, 99% purity), magnesium nitrate ($Mg(NO_3)_2 \cdot 6H_2O$), cerium nitrate ($Ce(NO_3)_3 \cdot 6H_2O$) and sodium carbonate (Na_2CO_3) were purchased from Panreac S.A.U©., sodium hydroxide (NaOH) and hydrochloric acid (HCl) from Mol labs *LTDA*©. All reagents were used without prior purification. All aqueous solutions were prepared with deionized water.

All gases and the CH_4:CO_2:N_2 1:1:2 mixture for the DRM catalytic test were purchased from Messer Colombia S.A© as high-purity gases.

Commercial honeycomb cordierite monoliths were bought from PingXiang CS Ceramic Co. Ltd.©; with a chemical composition of Al_2O_3 35.1±1.6%, MgO 13.5±1.5%, SiO_2 50.0±1.8%.

4.1.2. Synthesis of powdered catalysts by co-precipitation

LDHs route is chosen for synthesis, co-precipitating metal cations with carbonate counterion at basic pH, a method found in various publications.[23], [28], [81], [88], [95]

The synthesis begins by preparing a solution of Ni^{2+}, Mg^{2+}, Al^{3+}, and Ce^{3+} nitrates with nominal molar ratios of Ni/Mg=1,5 and (Ni+Mg)/Al=2. The nominal loads of Ce added were 0, 2, 4, and 7wt. % which were selected according to the work of Daza et al. [28] The nitrate solution is added dropwise to an excess Na_2CO_3 solution with vigorous stirring at pH=10,5 and a temperature of 60ºC, to later stop stirring and allow maturation for 24h at the same temperature. Next, the gel obtained was washed with deionized water and subsequently dried in an oven at 100ºC for 24h. The dried LDH material is pulverized and separated through an ASM 120 mesh. The mixed oxides were obtained after heat treatment of the LDH precursor at 700ºC, with a heating ramp of $10ºC \cdot min^{-1}$, for 12h. [128]

The synthesized mixed oxides were called MOX, where X is a number between 1 and 4 that increases with the increase in the Ce load.

4.1.3. Immobilization of mixed oxides in cordierite monoliths by slurry coating

Commercial cordierite monoliths employed have channel size L=0.0461 in (0.12 cm), a wall thickness w=0.0085 in (0.0216 cm), and a cell density N=470 cpsi. According to **Eq. 8-11**, the monoliths have OFA=0.676, GSA=70.8 and D=0.038.

Cordierite monoliths were laser-cut into 2.5cm cylinders, washed with distilled water, HNO_3 10%, NaOH 10%, and distilled water in an ultrasonic bath, then dried at 100ºC for 24h. Mixed oxides were obtained through wet impregnation, dipping the monolith in a hydrotalcite slurry for 3 minutes, blowing out the excess, drying at 100ºC for 24h, and finally calcining at 700ºC with a heating ramp of $10ºC \cdot min^{-1}$ for 12h.[25], [130], [131] **Fig. 8** shows the appearance of the monolith before and after slurry coating.

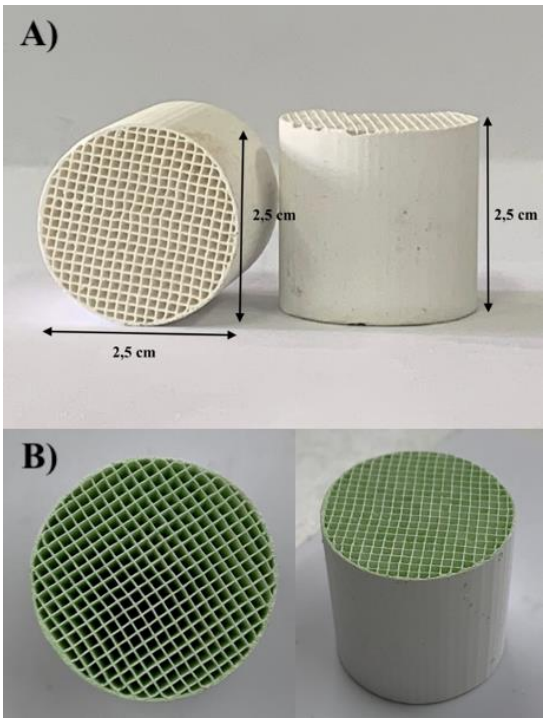

Fig. 8. A) Clean cordierite monoliths, B) cordierite monoliths after slurry coating.

Zhu et al. [132], conducted a study to optimize the characteristics of HT-type precursor slurry for coating cordierite monoliths in catalytic experiments. Factors such as slurry viscosity and particle size distribution were found to be influenced by pH, solid content, and additives used in the slurry. This study, one of the first references for hydrotalcite coating optimization, served as a basis for the design of the current work.

To produce structured mixed oxides with 0.0250 ± 0.0013 g of mixed oxide, the monoliths underwent one cycle of submersion in the slurry. For structured mixed oxides with approximately 0.100 ± 0.0098 g of mixed oxide, all monoliths were submerged in the slurry and blown four cycles before calcination. Several monoliths were prepared for each catalyst, ensuring the reproducibility of the method, the amount of immobilized catalyst, and the homogeneous coating of each material.

The materials were named following the nomenclature for powdered catalysts that include an S representing “structured”, with 1SMOX representing monoliths obtained from one immersion cycle and 4SMOX representing monoliths obtained from four immersion cycles.

4.2. Characterization of the materials

4.2.1. Characterization of the powdered catalysts

The elemental chemical analysis of the mixed oxides was carried out by X-ray fluorescence (XRF) in a Shimadzu© XRF-1800 sequential X-Ray fluorescence spectrometer.

The crystalline structure of the solids, before and after reduction at 700 and 800ºC, was studied by X-ray powder diffraction (XRD) on a Panalytical© XPert PRO MPD using a Cu anode (K_α=0.15418nm). The Ni^0 crystal size was calculated from the Scherrer equation.[24] The diffraction lines were identified by comparison with the JCPDS (Joint Committee of Powder Diffraction) standards.

The reductive properties were determined by temperature-programmed reduction with H_2 (H_2-TPR) using a Chembet 3000 Quantachrome© instrument with a thermal conductivity detector (TCD). The solids were degassed at 400ºC for 1h under Ar flow and then cooled to 25ºC. The reduction protocol includes a heating ramp of $10ºC \cdot min^{-1}$, using H_2/Ar at 10% v/v.[18], [28], [96]–[98], [133]

The total basicity and the CO_2 desorption profiles were determined by temperature-programmed desorption with CO_2 (CO_2-TPD) in a Chembet 3000 Quantachrome© instrument with a TCD. The powder materials were previously reduced at 700ºC, 1h, with H_2 flow, and cooled down to 50ºC. CO_2 adsorption was allowed with pure CO_2 (99%) until saturation. The desorbed CO_2 was measured in He flows with a heating ramp of $10ºC \cdot min^{-1}$. The interpretation of the H_2-TPR and CO_2-TPD results and evaluation of areas was developed using the OriginPro© software.[24], [28], [95], [97]

To determine the average size distribution of Ni^0, 200 particles were measured from images obtained by transmission electron microscopy (TEM) of the catalysts, pre-reduced at 700ºC for 1h with pure H_2. For the high-resolution TEM observations, a drop of the materials dispersed in EtOH was deposited on a cooper grid with a reticular amorphous carbon film and allowed to dry. The samples were analyzed by HR-TEM and energy-dispersive X-ray (EDX) with the scanning mode using a 200 kV FEI Talos F200S microscope. Multiframe TEM-EDX spectrum images were acquired over various particles using the Thermo Fischer Scientific Velox software (pixel size of 0,12nm, dwell time of 100 µs, about a few seconds per frame, about 250 frames). Hemispherical particle counting and measurement were done with ImageJ© software, and average diameter calculations were done using OriginPro© software to create histograms.

4.2.2. Characterization of the immobilized mixed oxides

Impregnated monoliths were previously cut and pulverized without any pretreatment. Then the crystalline structure was studied by X-ray powder diffraction (XRD).

Morphological analysis used SEM with a VEGA 3 SB TESCAN microscope, equipped with a W filament and high vacuum. Samples were cut longitudinally, deposited on graphite tape, and observed in inner and corner channels to check coated wall morphology. Micrographs were taken between 5mm and 1µm. The coated layer thickness was measured with ImageJ© software, and the average thickness was calculated using OriginPro© software to create histograms.

4.3. Catalytic test

A laboratory-scale DRM setup was used in this study, as shown in **Fig. 9**. Prior experiments were conducted to ensure that the catalytic tests were free from mass- or energy-transport limitations. Temperature measurements were performed using a digital thermocouple that was in direct contact with the catalytic bed.

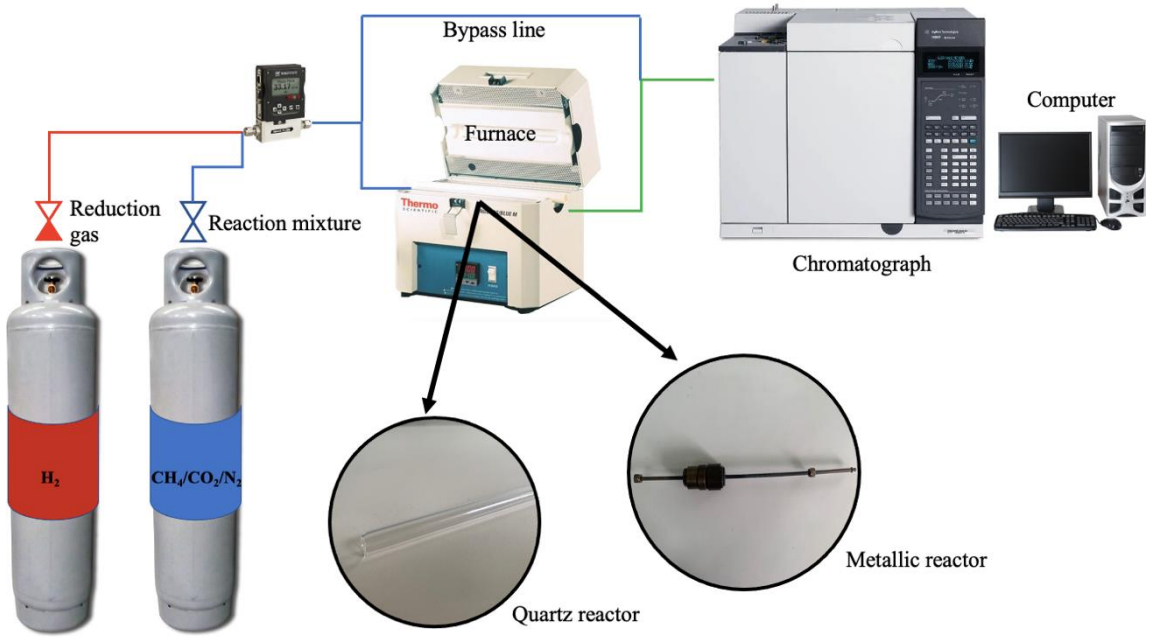

Fig. 9. Schematic of the reaction unit for the DRM process.

In this study, catalytic stability tests were conducted isothermally for 8 hours, under atmospheric pressure and a ratio of $CH_4/CO_2/N_2$ 1/1/2 for the reagents. For the powdered catalysts a fixed bed quartz reactor with a diameter of 6mm was used, it was loaded with 0,025g of the mixed oxide diluted in SiC. The total flow of the reactant's mixture was 50mL/min (GHSV = 94680 $mL \cdot g^{-1} \cdot h^{-1}$).

For the structured mixed oxides, a Fecralloy reactor was used, in which the entire monoliths with the dimension described above can fit. The total flow of the reactant's mixture was 50mL/min for both, the monoliths with a load of 0,0250g of mixed oxide (GHSV = 94680 $mL \cdot g^{-1} \cdot h^{-1}$) and the monoliths with a load of 0.1000g of mixed oxide (GHSV = 23670 $mL \cdot g^{-1} \cdot h^{-1}$).

Several experiments were performed, some were conducted with the catalyst unreduced, while others involved prior reduction under an H_2 atmosphere. For the unreduced tests, the temperature was raised to 700°C in an N_2 atmosphere before injecting the reaction mixture. In contrast, the catalysts in the prior reduction experiments were reduced at 700°C with H_2 flow for 1 hour, left to cool overnight, and then the reactions were carried out at a constant temperature of 600°C while maintaining the other mentioned conditions.

During the reaction, the gases were analyzed by gas chromatography in an Agilent 7890A chromatograph with an HP-PLOT/U column (L = 30m; D = 0,530mm; F = 20,0µm) in series with a HP-MOLESIEVE column (L = 30m; D = 0,530mm; F = 50,0µm); the system employs a coupled TCD and a flame ionization detector (FID). The detailed chromatography method is presented in **Supplementary Material**.

The conversion of CH_4 and CO_2, and the H_2/CO ratio of the reaction, were calculated using **Eq. 13-15**:

$$CH_4\ conversion\ (\%) = \frac{(CH_4)_{in} - (CH_4)_{out}}{(CH_4)_{in}} \quad (13)$$

$$CO_2\ conversion\ (\%) = \frac{(CO_2)_{in} - (CO_2)_{out}}{(CO_2)_{in}} \quad (14)$$

$$H_2/CO\ ratio = \frac{(H_2)_{produced}}{(CO)_{produced}} \quad (15)$$

4.4. Characterization of the spent catalysts

The thermal behavior of the powdered materials after the catalytic test was studied by thermogravimetric analysis (TGA) using a TA SDT Q 600 thermal analysis equipment with simultaneous differential scanning calorimetry (DSC). A heating ramp of $10^{o}C \cdot min^{-1}$ in an air atmosphere was used.

To identify the mass quantity of coke obtained by the immobilized catalysts, their initial weight before the catalytic test and the final weight of the monolith after the catalytic test were compared; the increase in mass of the materials was attributed to the deposited carbon during the reaction period.

The amount of carbon obtained by the catalysts was exposed using **Eq. 16**:

$$carbon = \frac{g_C}{g_{Cat} \cdot h_{rxn}} \quad (16)$$

Where g_C is the gram of carbon obtained, g_{Cat} is the grams of catalyst used in the reaction, and h_{rxn} is the reaction time in hours.

The morphological analysis of the powdered and monolith spent catalysts was performed by scanning electron microscopy (SEM) technique using a VEGA 3 SB TESCAN microscope, equipped with a W filament and high vacuum. The samples, collected after the catalytic test, were deposited on a graphite tape and placed in a sample holder. The materials were observed to identify carbon structures formed during the reaction. Micrographs were taken between 5mm and 1μm.

5. RESULTS AND ANALYSIS

5.1. Characterization of the powdered catalysts

The chemical compositions of the different HT-derived materials (mixed oxides) without promoter and promoted with Ce were determined to clarify their influence on the activity, selectivity, and stability of these catalysts. **Table 8.** shows the composition of the materials determined by XRF along with their empirical formula.

A Ni content between 22.07 and 23.75% was measured for all the obtained mixed oxides, values close to the nominal amount of 25% for each one. Regarding the Ni/Mg and M^{II}/M^{III} molar ratios obtained in the mixed oxides, the first varies between 1.33 and 1.25, while the second varies between 1.63 and 1.59. It is evident from the data that the molar ratios were below their nominal values, primarily because the observed amount of Ni was less than expected. This discrepancy can be attributed to the pH-induced increase effect, which occurred because of the acidic nature of Ni. Consequently, the precipitated metal hydroxide is likely to undergo re-dissolution, resulting in an approximate 1.5% loss.[84]

The difference between the Ce nominal values and the values obtained can be attributed to the fact that Ce^{3+} species are not included in the hydrotalcite structure because of their different ionic sizes. Furthermore, the impact of pH fluctuations is noteworthy, because Ce behaves as an acidic metal. The authors exposed this behavior by analyzing the XRD results of the material obtained by co-precipitation, where the diffractograms of hydrotalcites and their derived mixed oxides presented the peaks of CeO_2 species, appearing as a segregated phase in the material [23], [85]. For this reason, during the washing process of the hydrotalcite, the lixiviation of Ce species may cause a lower wt.% Ce value in the final mixed oxides.

Table 8. XRF results for elementary chemical analysis of the mixed oxides obtained.

Mixed oxide	Ce [a] (wt. %)	Ni [b] (wt. %)	Ni/Mg [c]	(Ni+Mg)/Al [d]	Empirical formula of the mixed oxide
MO1	-	23.48	1.25	1.63	$Ni_{0.343}Mg_{0.275}Al_{0.380}O_{1+x}$
MO2	1.97	23.35	1.26	1.63	$Ni_{0.340}Mg_{0.271}Al_{0.375}Ce_{0.012}O_{1+x}$
MO3	3.28	23.75	1.33	1.63	$Ni_{0.346}Mg_{0.260}Al_{0.373}Ce_{0.020}O_{1+x}$
MO4	6.52	22.07	1.30	1.59	$Ni_{0.333}Mg_{0.255}Al_{0.370}Ce_{0.041}O_{1+x}$

[a] Nominal wt.% Ce (MO1= 0, MO2=2, MO3=4, MO4=7), [b] Nominal wt. % Ni= 25, [c] Nominal Ni/Mg = 1.5, [d] Nominal M^{2+}/M^{3+} = 2 for all mixed oxides.

The process of synthesis by co-precipitation at constant pH with Ni^{2+}, $Mg^{2+,}$ and Al^{3+}, is simple and highly effective for obtaining lamellar structures [83]. With the formerly mentioned precursors, these materials have a unique layered structure where the 2+ and 3+ metal cations are randomly distributed; therefore, Ni ions can be dispersed in the layered structure benefiting from the insulation of Mg and Al ions, minimizing nickel aggregation.[58]

After thermal treatment, the lamellar HT-like structure collapses, and then mixed oxides are formed after calcination, where the dispersion of the cations is maintained.[54], [83] In **Fig. 10 - A**. it can be observed from the diffractogram of the mixed oxides obtained with different Ce loads that the heat treatment destroyed the HT structure because no characteristic peaks were detected. The reflections at 37.0, 43.0°, and 62.4º2θ that are ascribed to periclase-like structures of MgO (º2θ= 36.9°, 43.0 – JCPDS nº45-0946), NiMgO (º2θ= 37.09, 62.78 – JCPDS nº24-0712), or NiO (º2θ= 43.03 – JCPDS nº44-1159), which may support the synthesis of isomorphic substitutions of Mg^{2+}, Ni^{2+}, and even Al^{3+} ions to obtain HT, leading to NiMgAlO mixed oxide solid solutions after thermal activation.[83], [85], [90] In addition, the diffractograms do not show peaks corresponding to crystalline phases of segregated aluminum oxides.

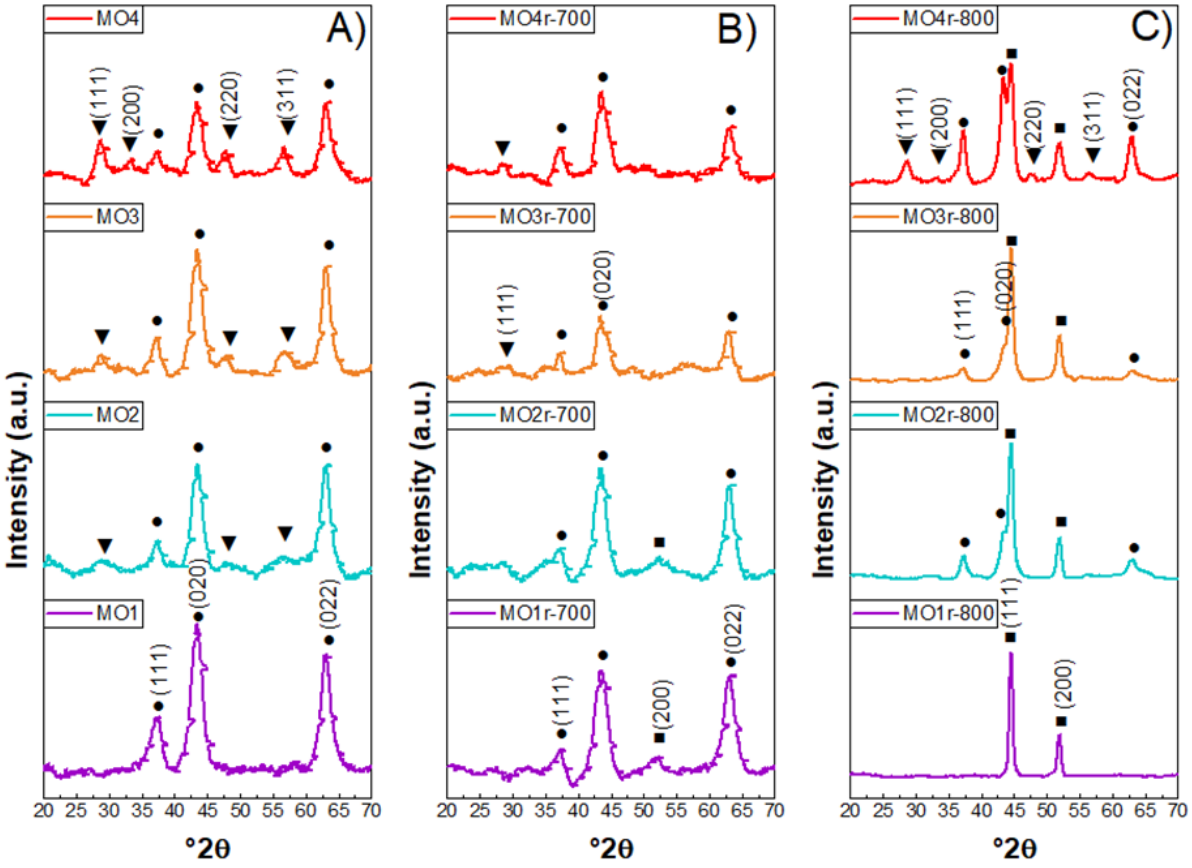

Fig. 10. X-ray diffractograms were recorded for A) mixed oxides, B) mixed oxides reduced at 700ºC-1h and C) mixed oxides reduced at 800ºC-1h. • : Periclase-like structure, ▼ : CeO_2 fluorite structure, ■ : Ni^0 metallic nickel.

When examining the ionic sizes of cations (Mg^{2+}=0.65Å, Al^{3+}=0.55Å, Ni^{2+}=0.69Å, and Ce^{3+}=1.15Å) for the Hume-Rothery analysis, it becomes clear that Ce^{3+} is not compatible with the Ni-Mg-Al lattice due to its size, which is nearly twice as large as the others. Therefore, the Ce-containing materials are a mixture of two types of crystalline phases: the aforementioned periclase-like solid solution and segregated CeO_2 fluorite (JCPDS nº34-

0394); indicating that there was no effective inclusion of Ce^{3+} ions in the brucite-like layers of the HT precursor. [28], [83], [85], [88], [90]

As exposed in **Table 9.** the crystallographic parameter *a*, calculated from the XRD results is close to the value reported for the periclase structure (JCPDS nº45-0946), another indicator that Ce was not included in the Ni-Mg-Al crystal lattice. **Table 9.** displays the crystallite sizes smaller than 7 nm for the CeO_2 fluorite structure. Increasing the nominal amount of the promoter added to the catalyst also resulted in larger crystallite sizes. This characteristic can lead to a diminution in the surface area of a mixed solid. [134]

The XRD patterns for the reduced catalysts (700ºC-1h, H_2 flow) are presented in **Fig. 10 - B.** The temperature of 700°C was chosen for the DRM catalytic experiments in this study, as it is a common and suitable temperature for such investigations. The signals of the periclase-type phase are clear, demonstrating the stability of the structure. Also, in the MO1 and MO2 catalysts, the reflection at 51.9º 2θ can be identified and attributed to the Ni^0 (JCPDS nº65-0380) structure [20], [90], [135] However, the reflection at 44.8 º 2θ (111) is not identified because of possible overlap with other signals.

Due to weak signals and lack of Ni^0 signals in catalysts with high Ce load, the crystallite size of Ni obtained at 700ºC couldn't be calculated. Instead, **Fig. 10 - C** shows the fully reduced mixed oxides at 800ºC, where the signals of periclase-like structure and CeO_2 fluorite structure are identified, along with the Ni^0 signals (44.8 º 2θ (111), 51.9º 2θ (200)), enabling the determination of metallic Ni crystallite sizes (**Table 9**). The values showed a correlation with the Ce load, with the mixed oxide having the highest Ce content and exhibiting the smallest particle size. This phenomenon has been explained by some authors, including Meng et al. [136], who attributed it to the effect of Ce addition on the dispersion of Ni within the structure.

Table 9. Brucite-like structure crystallographic parameter and CeO_2 and Ni^0 crystallite sizes. Reducibility of the mixed oxides at 700ºC. TEM Ni^0 particle sizes.

Mixed oxide	$a_{Periclase}$ (nm) [a]	$\tau\ CeO_2$ (nm) [b]	$\tau\ Ni^0$ (nm) [b]	***Reducibility*** (% at 700ºC)	***Ni^0 Particle size*** (nm) [c]
MO1	0.446	-	13.3	61.5	7.32 ± 1.60
MO2	0.447	N.D.	10.5	95.5	6.97 ± 1.51
MO3	0.449	3.1	10.6	97.3	7.70 ± 2.95
MO4	0.447	6.7	8.9	98.0	5.20 ± 3.16

[a] Crystallographic parameter of periclase phase, [b] Crystal size calculated by Scherer's method.[17] N.D. = Not determined due to low signal intensity, [c] particle size determined by TEM.

Fig. 11. shows the H_2-TPR profiles of the mixed oxides, which have one wide asymmetric reduction peak with maximums between 790 and 745ºC, corresponding to the reduction of surface and bulk NiO in the periclase structure to metallic nickel.[23] In contrast to pure bulk NiO, the reduction peaks are shifted to higher values [19], indicating stronger interactions between NiO and the other metallic species, forming the stable NiO/MgO-Al_2O_3 solid solution.[137] The peaks represent a combination of components as observed in the

deconvolution curves of the H_2-TPR profiles (**Fig. 11–A**); at lower temperatures, the reduction of Ni^{2+} in the surface mixed oxide phase is observed. However, at higher temperatures, the component that experiences Ni^{2+} reduction is the NiO mixed oxide bulk. [19].

On the other hand, when comparing the mixed oxide without Ce to the Ce-promoted mixed oxides, shifts towards lower reduction temperatures were observed. The reduction peak for solid MO1 occurred at 790ºC, while the peaks for MO2, MO3, and MO4 were observed at 765ºC, 750ºC, and 745ºC, respectively. Different publications by Dębek et al. [84], [91], [99] indicated that Ni catalysts derived from hydrotalcites and promoted with Ce present a similar result to the one exposed in this work. The promoting effect is attributed to the presence of Ce^{3+}/Ce^{4+} redox pairs, facilitating electron transfer and reducing nearby Ni-oxide species.[138]

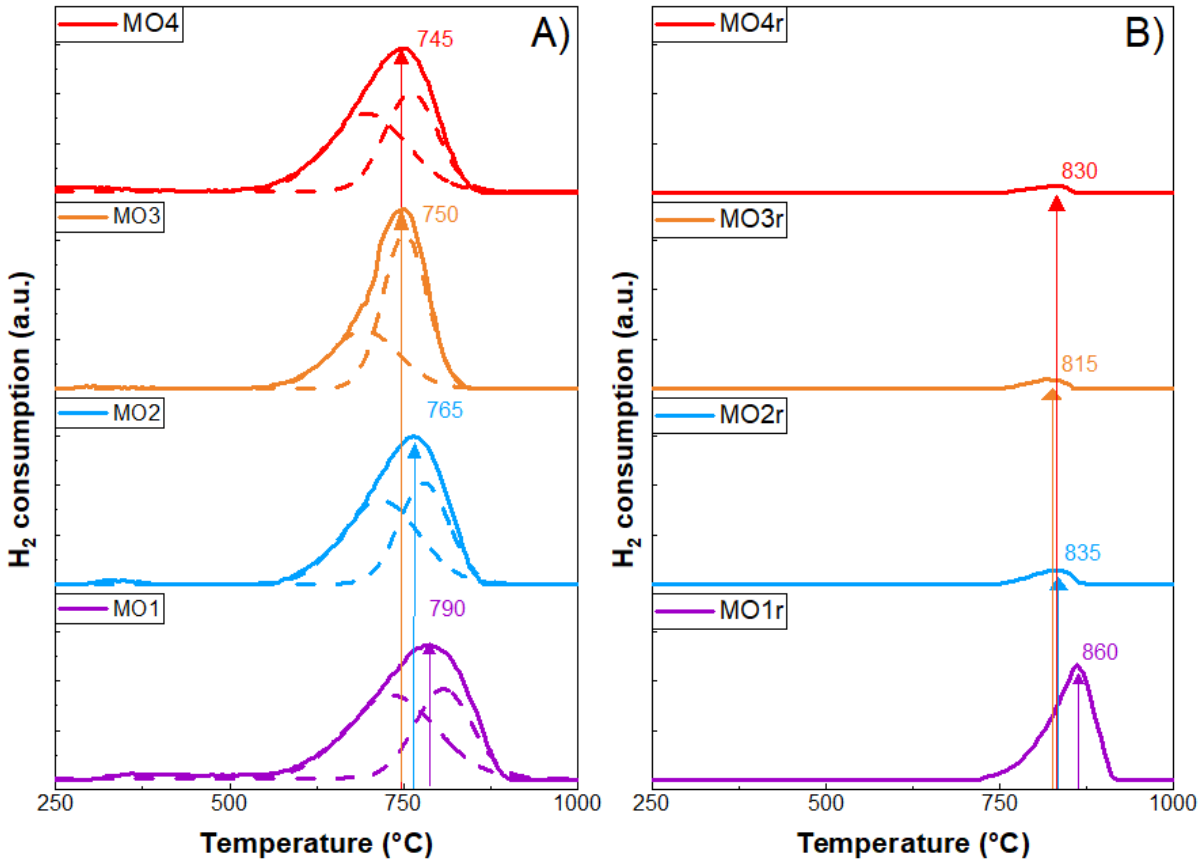

Fig. 11. H_2-TPR profiles of A) mixed oxides and B) mixed oxides after reduction at 700ºC-1h.

As the reduction temperature for the oxides exceeded 700°C, the catalysts were likely only partially reduced during the DRM reaction performance tests. [11], [77] Hence, it is essential to semi-quantitatively assess the degree of catalyst reduction. To achieve this, the catalysts were reduced at 700°C with pure H_2, and an additional TPR was conducted to determine the

consumption of hydrogen by the remaining reducible species; the results are presented in **Table 9**. It can be seen that all the catalysts present a partial reduction of Ni, with reducibility percentages of 61.5% for MO1 and 95.5, 97.3, and 98.0% for MO2, MO3 and MO4 at 700ºC, indicating that much of the reducible nickel in the materials will be active in the reaction at this temperature.

A promoting effect of Ce on reducibility can be observed since the reduction percentages of the catalysts increased when this metal was present in the solids, a higher Ce load exposed a higher reducibility percentage. Authors such as [87], [138], [139] also report the benefits of incorporating Ce into catalysts comparing the higher reducibility of Ni species, and it is even mentioned that the easy reducibility of CeO_2 promotes the reduction of nickel phases through a spillover mechanism between oxygen vacancies of ceria.

In addition, TPD with a probe molecule is usually applied to determine the strength and density of basic sites in mixed oxides. CO_2 as a probe molecule has enough acidity to probe all the basic sites, besides being one of the two reagents for the DRM that must be activated by the catalytic system.[90] Therefore, its use is more than adequate to characterize the obtained materials. As reported in the literature, the basicity of the mixed oxides depends on the composition of the catalyst's precursors, the presence of promoters, and special treatments, among others.[12], [53], [87]

Fig. 12. shows the CO_2 – TPD catalysts desorption profiles, while the quantitation of the catalyst's basicity is summarized in **Table 10.** After the reduction of the catalysts, a curve with three CO_2 desorption asymmetric peaks can be observed; from literature, HTs-derived material exhibits these typical peaks, which are classified according to their basic strength related to CO_2 temperature desorption: I) the first desorption peak observed at 100-120ºC can be attributed to the desorption of CO_2 from weak Brønsted OH groups, II) the peak observed at 200-220 ºC is because of the formation of bidentate carbonates formed on metal-oxygen pairs; weak and moderate basic sites, that according to Rached et al.[90], in Ni-Ce/Mg-Al mixed oxides are due to the presence of nickel and cerium. And the final peak, III) the strong basic site observed at 280-300ºC, originated from the desorption of CO_2 bonded with low-coordination oxygen anions; is due to the magnesium content.[20], [99]

This classification and identification of species in basic sites, mentioned above, have been proposed by different authors as Cosimo et al.[140], based on data obtained by IR spectroscopy and CO_2–TPD derived from mainly Mg/Al mixed oxides.

All the mixed oxides presented the three representative peaks, whereas the weak and medium basicity peaks do not present significant variation. However, the introduction of ceria resulted in the formation of more basic sites, mostly in terms of low coordinated oxygen species, result that agrees with that obtained by Dębek et al.[97] In the mixed oxides, the Ce may favor the adsorption of CO_2 due to the presence of the redox pair Ce^{+4}/Ce^{+3}, which is recognized for its oxygen storage.[20] Because the redox pair maintains the fluorite structure, oxygen vacancies can trap an oxygen atom of CO_2, thereby increasing the number of surface carbonates that can form.[141]

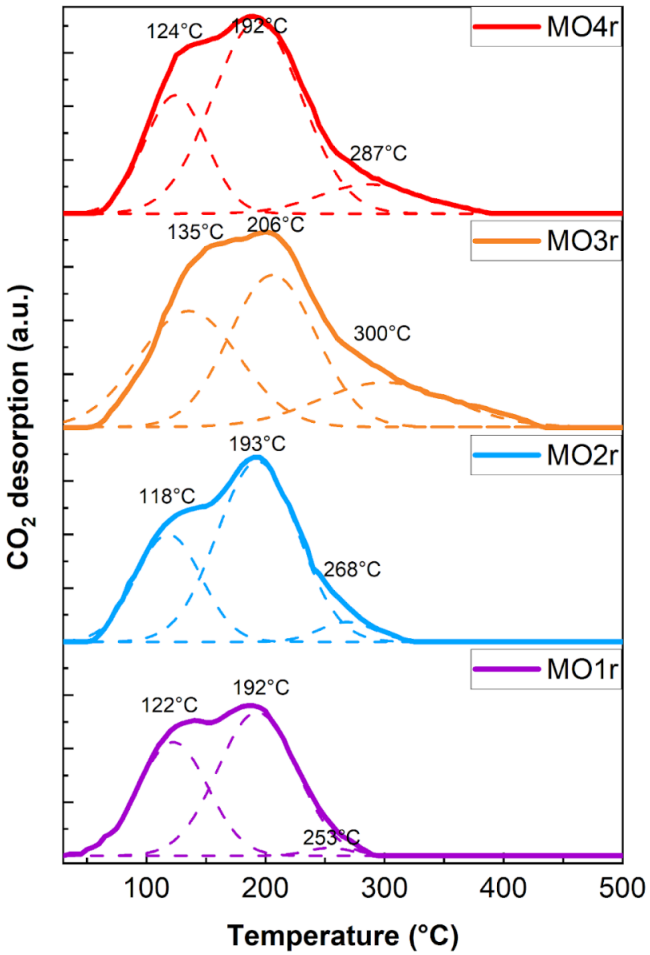

Fig. 12. CO_2-TPD for the mixed oxides after reduction at 700ºC-1h.

Regarding this issue, Daza et al.[98] argue that in this kind of material, the Ce shows a beneficial effect on the basic properties, such as indicated by the measurements of the total basicity, increasing the capacity of CO_2 adsorption; even though CeO_2 bulk shows very low basic properties, by which the authors suggest that the obtained effect is synergetic with the present Mg. By enhancing the adsorption and activation capacity of CO_2 in the materials, this phenomenon facilitates easier carbon gasification through the reverse Boudouard reaction, which is a desirable characteristic of the DRM process.[12], [49]

Table 10. Basicity of prepared materials.

Mixed oxide	Desorption peaks (area %)[a]			Adsorbed CO_2 ($\mu mol \cdot g^{-1}$)
	l.t.p.	m.t.p.	h.t.p.	
MO1r	40.4	57.8	1.8	4.21
MO2r	31.0	64.1	4.9	4.78
MO3r	37.8	43.0	19.1	6.63
MO4r	26.6	62.6	10.8	5.81

[a]l.t.p. = low-temperature peak; m.t.p. = middle-temperature peak; h.t.p. = high-temperature peak.

Traditionally, nickel-based catalysts used in reforming technologies are cheap and active, however, as mentioned before, these are prone to deactivation by sintering and carbon deposition.[8] Carbon layers that grow from nuclei on step sites on the nickel particle are stable above 80 atoms in diameter (approximately 6nm), meaning that larger particles are more likely to yield carbon.[73]

Understanding the particle size of the synthesized materials is crucial, TEM was employed to determine the particle size after reduction at 700ºC – 1h. Micrographs were obtained before measuring the size, morphology, and chemical identity of the particles. In **Fig. 13.** TEM images for the mixed oxides can be seen (in **Supplementary material**, it can be found the EDX analysis). The images show the formation of well-distributed hemispherical aggregates which mostly contain Ni according to EDX; it is assumed that these particles are mostly Ni^0 nanoparticles. [85], [87], [88], [135]

Fig. 13. also evidences the Ni^0 particle size distribution for the reduced catalysts and the average particle sizes for the catalysts, counted from about 200 particles (see **Table 9.**) The particle size did not vary significantly with the addition of Ce and the different loads, as expected [58], [72], [87]. Similar results have been reported with Ni particles remaining small even at loadings as high as 77 wt.% for HTs-derived Ni catalysts.[142] **Table 9.**, as mentioned, records the Ni^0 crystallite size and the TEM average particle sizes, where it can be seen that the obtained values present a similar trend.

Aramouni et al.[73] studied the effect of catalyst particle size on the thermodynamic equilibrium of DRM and carbon formation through the Gibbs free energy minimization method, from which they have been able to highlight the need for active metal particle size to be less than 5-6nm to minimize coke formation. Particle sizes are not far from the sizes obtained on average by the catalysts of this work.

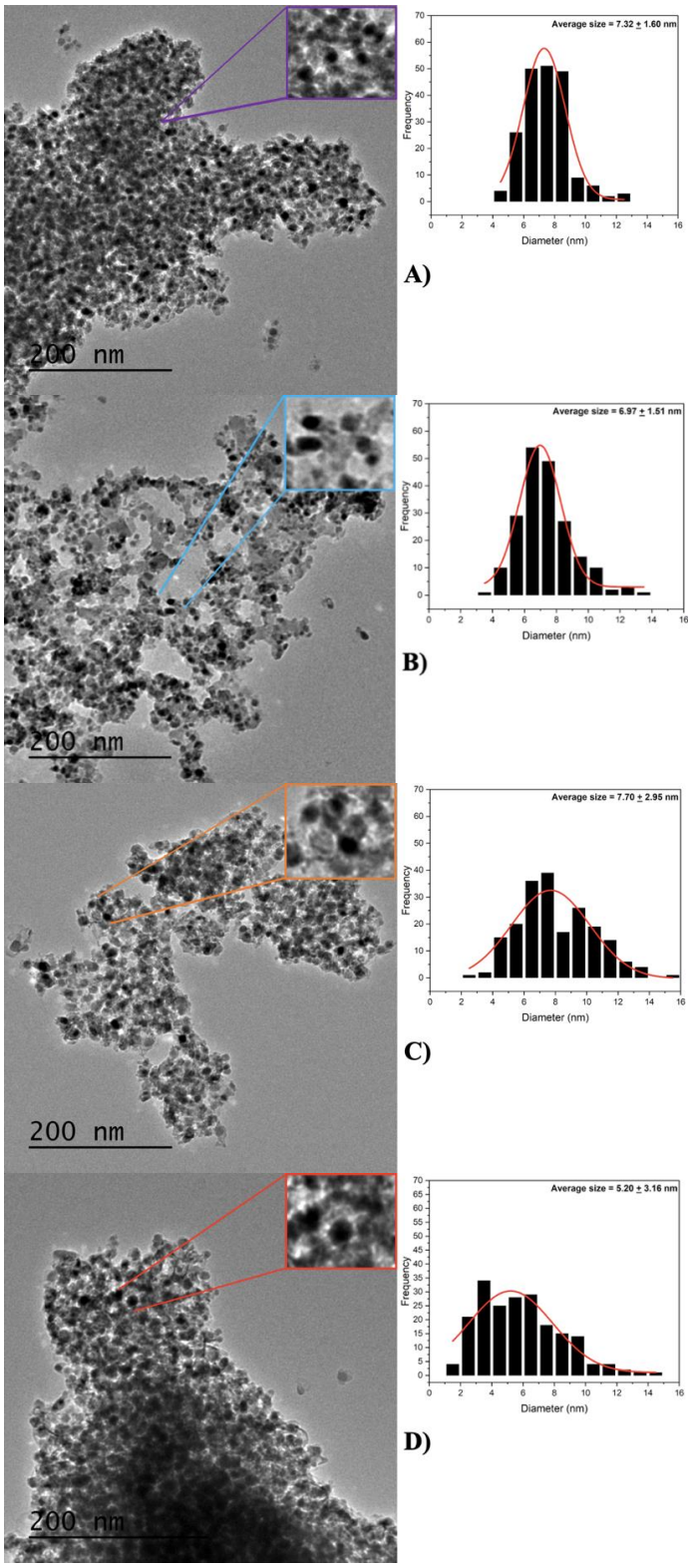

Fig. 13. TEM images of the mixed oxides reduced at 700ºC-1h and the nanoparticle size distribution. A) MO1r, B) MO2r, C) MO3r and D) MO4r.

5.2. Characterization of the immobilized mixed oxides

The XRD patterns of the bare cordierite monoliths and all the immobilized mixed oxide (see **Fig. 14.**) show the main peaks at º2θ= 21.66, 26.30, 28.38, 29.36, 33.81, and 54.22 correspond to the cordierite phase (JCPDS 85-1722).[143] Owing to the small amount of mixed oxide impregnated in the entire monolithic structure (mixed oxides is ~0,4wt.% of the total structure), it is not possible to identify the peaks corresponding to the crystallographic planes of the species already elucidated in the XRD of the powder mixed oxides. However, the high stability of the cordierite structure is evident even after resisting the slurry coating, followed by a temperature treatment for 12h at 700ºC for the calcination period.

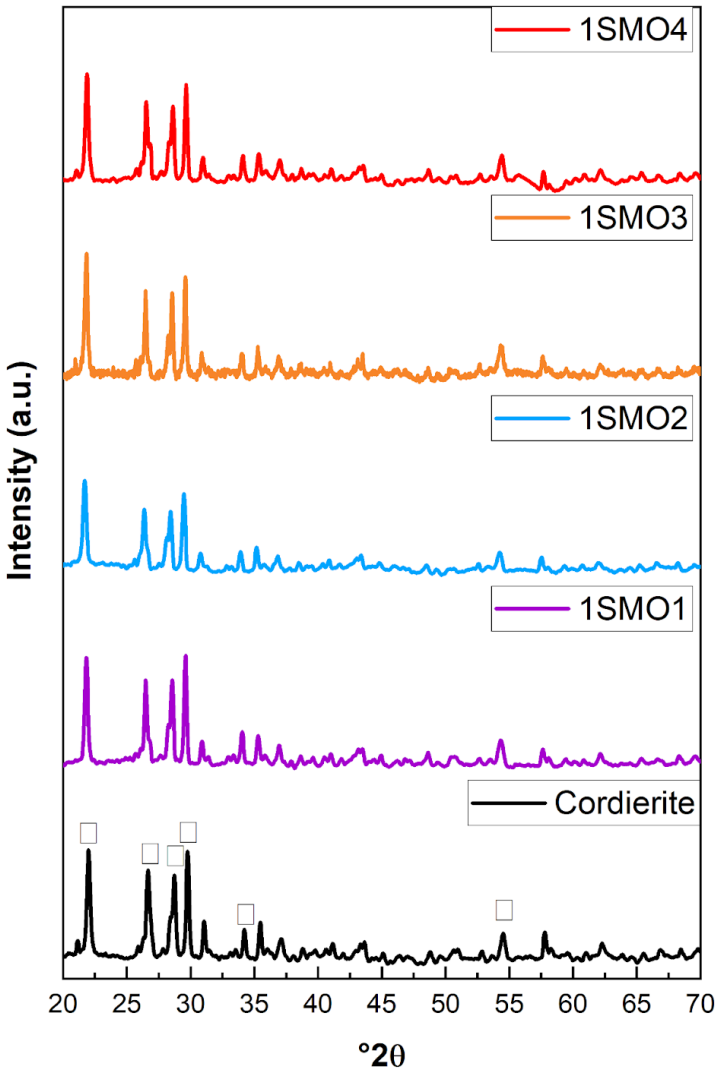

Fig. 14. X-ray diffractograms were recorded for the bare cordierite and the SMOx fresh after calcination at 700ºC-12h and powdered. □: Cordierite.

SEM examination of the coated monoliths with 0.100 g of mixed oxides after calcination at 700ºC (see **Fig. 15**) reveals a homogeneous coverage of the entire monolithic surface. However, accumulation at the edges of the monolith and cracks can be observed throughout

the entire surface, resulting in the formation of a layer of mixed oxides composed of flakes of different sizes on top of the monolith. This can occur because water droplets, due to surface tension, may accumulate and fail to enter the interior of the monolith channel, leading to material agglomeration at the channel entrance. Despite a noticeable greater accumulation of the coating material on the edges of the monolith channels, it was confirmed that none of the monolith's channels were clogged by the catalytic material layer.

Similar results were obtained by Villegas et al. [113], who washcoated the monoliths with alumina. They found that the formation of cracks was not caused by the calcination process, but rather during the initial drying step at 100ºC, when the temperature was increased from room temperature up to 800ºC, a procedure like that applied in this study.

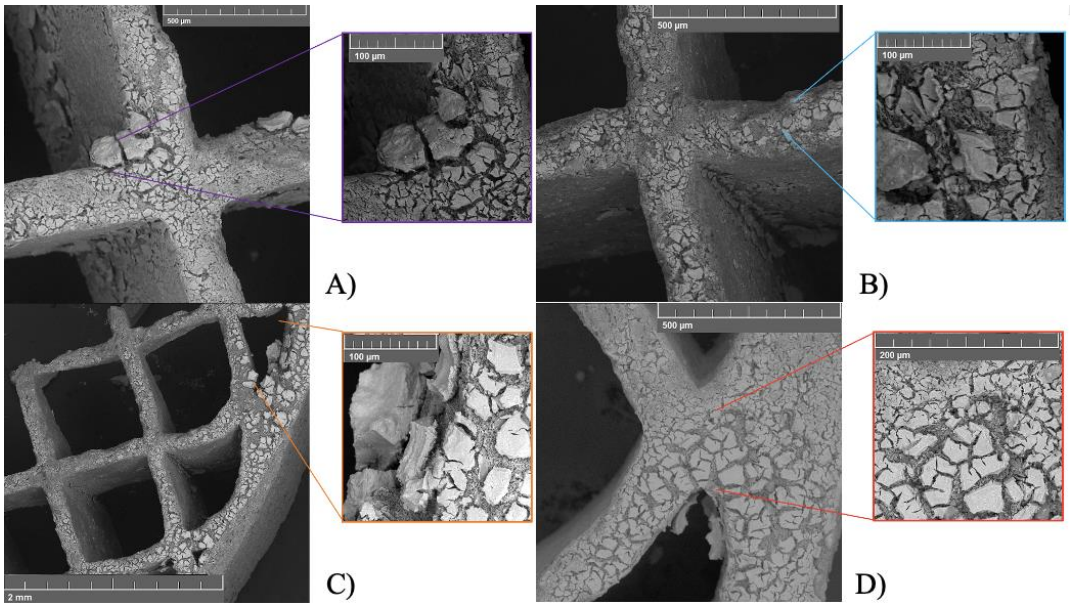

Fig. 15. SEM micrographs of the structured mixed oxides A) SMO1, B) SMO2, C) SMO3, D) SMO4.

The thickness of the coated layer was determined, measuring more than 100 points on the surfaces of the monoliths. **Fig. 16.** shows the histograms obtained by the combined thickness measurements, where for the monoliths with a load of 0.025g in general, an average layer thickness of 6.13 ± 1.97µm was obtained; and for the monoliths with a load of 0.100g an average coat thickness of 9.87 ± 4.25µm is found. As expected, increasing the coated mixed-oxide load increased the width of the layer, but despite quadrupling the mass, the increment was not proportional.

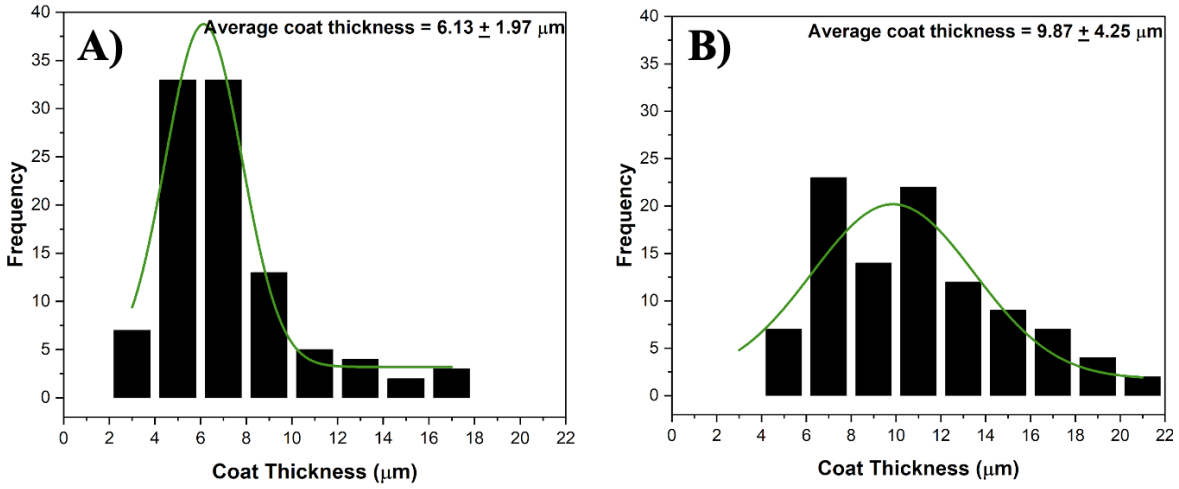

Fig. 16. Histograms derived from measurements of coated layer thickness from the obtained SEM micrographs. A) for 0.025 g and B) for 0.100 g loaded monoliths.

5.3. Catalytic test with powdered catalysts

In this study, we evaluated the performance and stability of mixed oxides synthesized using the DRM process. The chosen conditions for the evaluation have been previously detailed in the methodology. To have an approach to the method, studies were carried out in triplicate for the reactions; an example of triplicate is shown in **Supplementary Material**, with which deviations of less than 5.5% were found respect to the identification of reagents conversion, and deviations under 2.5% to the assessment of the products (H_2 or CO) yield.

5.3.1. Test for non-reduced powdered catalysts

The DRM performance of the different mixed oxides was evaluated under severe conditions of $CH_4/CO_2 = 1$, T = 700ºC, and a WHSV = 94,680 $mL \cdot g_{Cat}^{-1} \cdot h^{-1}$ for 8h. Considering that the reaction mixture can promote a reductive medium, where high temperatures can promote the obtaining of Ni^0 by the dissociation of CH_4 [98], [144], it was decided not to carry out a reduction of the materials before reaction; which can translate into energy, reagents, and time savings. The reagents conversions, the products yield, and the H_2/CO vs. time on stream (TOS) are given in **Fig. 17.** For comparison, the thermodynamic equilibrium conversions and yields reported by Jensen et al.[145] and Nikoo et al.[59] are included.

Fig. 17 - A. shows the catalytic conversion of CH_4, exposing that all mixed oxides have a conversion higher than 70% and, even though the thermodynamic conversion was not reached, evidence of obtaining highly active Ni-based materials at 700 °C under reactants reduction. In the case of MO1, the initial conversion decreases less than 3% when reaching 8h of reaction, showing stability even under the severe reaction conditions; in comparison, from the Ce-containing materials, MO2 presented the higher conversion of CH_4 during the whole catalytic test, sharing an attempt of a promoting effect of Ce on catalytic activity.

Meanwhile, it is observed that by increasing the Ce load in the mixed oxides, the catalytic conversion of the material does not increase, but on the contrary, they exhibit a lower methane conversion; however, the activities of the solids MO3 and MO4 were stable with time under the reaction condition. Daza et al.[28] and Ren et al.[88], present similar results and explain that when the load of Ce increases, the activity reduces due to the reduction in the superficial area of the material. Lino et al.[23] stated that the inclusion of Ce in Ni/MgAl materials reduced the surface area due to ceria's low porosity. They also noted that Ce appeared to alter the pore size distribution, narrowing it, implying a greater presence of smaller pores in the promoted catalysts suggesting that CeO_2 partially blocks the pores.

All materials "exceed" the thermodynamic equilibrium values (**Fig. 17 - B.**) for CO_2 conversion, probably because of side reactions where CO_2 is consumed or stable carbonate formation.[95] In all cases, the mixed oxides exhibit stable conversions during the catalytic test. However, an increase in the load of Ce does not necessarily imply a beneficial effect on the catalytic activity.

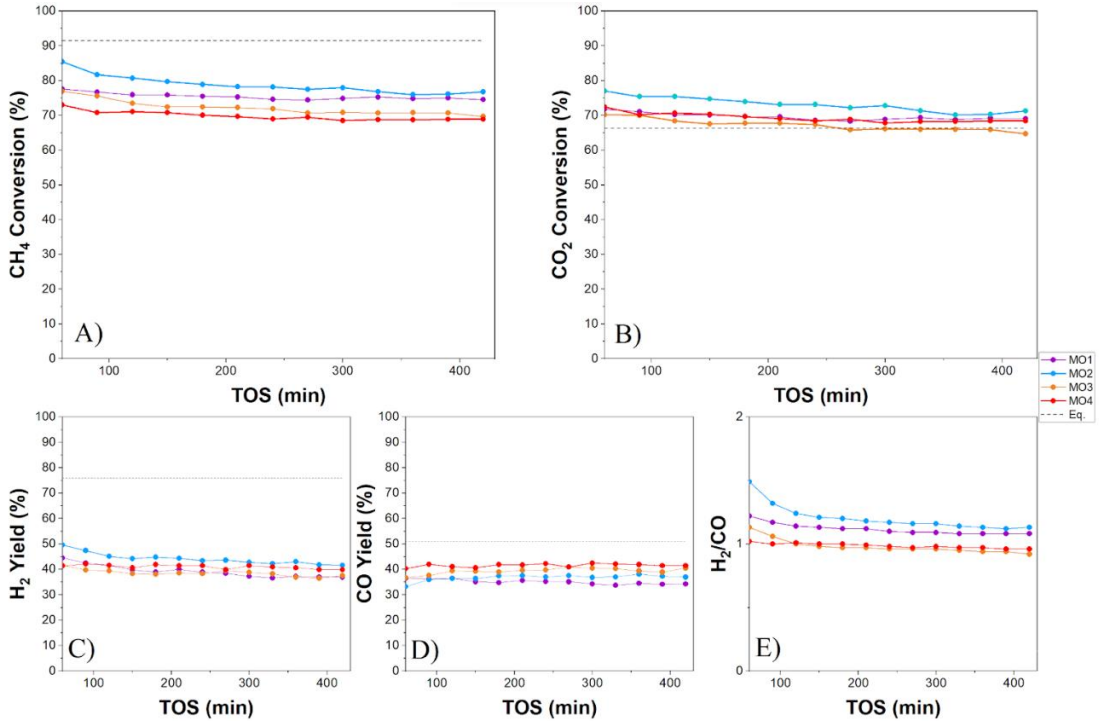

Fig. 17. Catalytic A) CH_4, B) CO_2 conversion; catalytic C) H_2, D) CO selectivity and E) H_2/CO vs. TOS for non-reduced powder catalysts. Reaction conditions: 700ºC-8h and 94,680 $mL \cdot g_{Cat}^{-1} \cdot h^{-1}$.

Fig. 17 – C, D, and **E** display product yields and H_2/CO ratios, revealing the catalytic selectivity of the mixed oxides. MO2 exhibited higher selectivity towards H_2, while MO3 and MO4 showed the highest selectivity towards CO. The yield percentages of H_2 during the first hour of TOS are higher than those obtained in the last hours of the reaction. This higher production of H_2 may be due to the initial in situ Ni^{2+} reduction process until the maximum amount of Ni^0 is obtained.[144] However, yield values for all samples are very similar once stability is attained with time, laying between 36% and 41% toward H_2.

The higher CO yield % in materials with more Ce can be explained by their basic properties, promoting CO_2 adsorption on basic centers and dissociation on Ce_2O_3, generating CO and CeO_2; the CeO_2 reacts with the carbon produced from CH_4 decomposition, producing CO, Ce_2O_3 and Ni^0 particles free of carbon. [23] In the previous characterization, MO3 and MO4 showed the highest CO_2 adsorption, supporting this explanation.

The H_2/CO ratios show initial values from 1.0 to 1.5 for the catalysts, which slightly decreased during the 8h on stream. A H_2/CO ratio larger than 1 ratifies that the CH_4 decomposition reaction, which produces H_2, was intense at the beginning. The highest H_2/CO ratio was observed on the MO2 material, for which the conversions and yield percentages variation are the greatest. Kalai et al.[85] also obtained a similar behavior with solids that had a Ce load of 4.5 wt.% in HT-derived materials with a Ni load of 20 wt.%.

To get close to the identification of the carbon formed in the catalytic tests, TGA profiles were obtained for the catalysts after the reactions (**Fig. 18.**). Thermal events in TGA profiles are well-known and have been mentioned in the literature. [146], [147]; highlighting that carbon nanotubes, nanofibers, and other structures resembling whiskers are examples of reactive carbon deposits that are oxidized at temperatures between 480 and 600ºC; while graphitic carbon, a non-reactive, highly deactivating species, burns at temperatures above 700 °C.

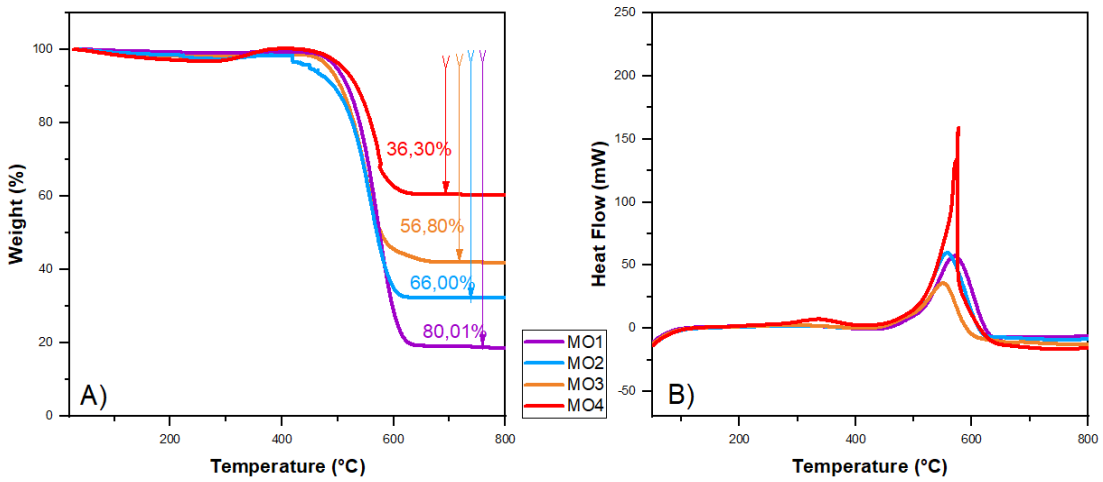

Fig. 18. A) TGA and B) DSC profiles for non-reduced powder catalysts. Reaction conditions: 700ºC-8h and 94,680 $mL \cdot g_{Cat}^{-1} \cdot h^{-1}$.

The TGA profiles of all the catalysts showed a mass loss event between 480 and 610ºC, which then corresponds to reactive carbon deposits. Where it is possible to see a progressive increase in mass loss, in the order MO1>MO2>MO3>MO4, evidencing the important decrease in the formation of carbon in the Ce-promoted catalysts. The amount of carbon formed was calculated obtaining values of 0.1000, 0.0825, 0.0710 and 0.0453 $g_C \cdot g_{Cat}^{-1} \cdot h^{-1}$ for the materials MO1, MO2, MO3, and MO4, respectively. Therefore, while the Ce load did not significantly enhance the catalytic activity, it demonstrated its impact on the catalyst stability against carbon formation. With increasing Ce loading, less carbon was produced at the end of the catalytic test.

Additionally, from **Fig. 18 – B.** the DSC profiles confirmed the combustion temperature ranges of the carbon species; however, for the MO4 an exothermic event close to 350ºC was also observed, which is due to the oxidation of amorphous carbon species.[148]

Delving a little deeper into the study of the carbonaceous structures obtained on the materials, **Fig. 19.** shows the SEM micrographs obtained for a post-reaction sample of the mixed oxides MO1 and MO4, in which whisker-like carbon structures stand out, supporting what was deduced from the TGA reports; and revealing that the structures of the carbon species obtained do not vary if the catalyst is promoted. Ren et al.[88] mention that small variations in the TGA-DSC patterns over these types of catalysts can be explained by the different extents of the crystallinity and disorders of the deposited carbon.

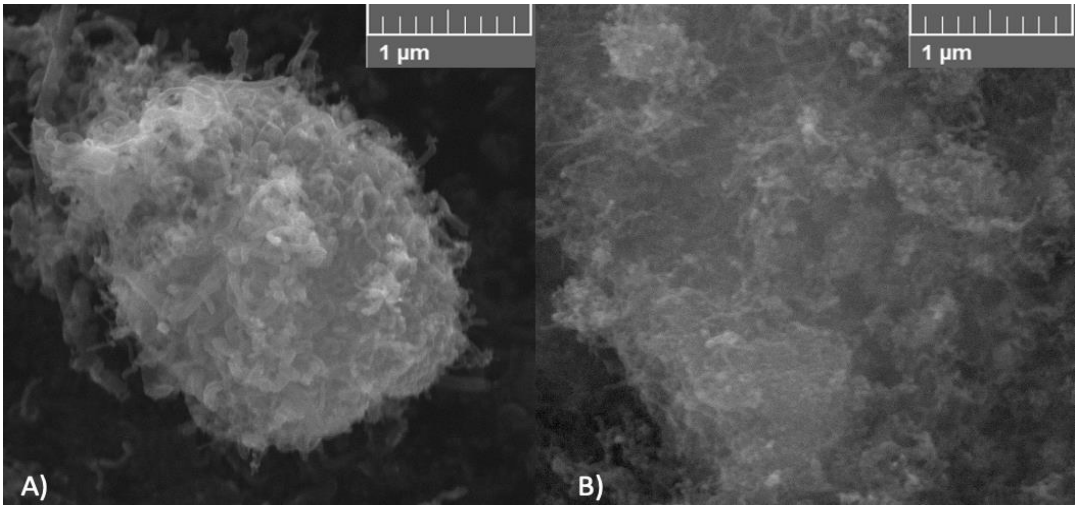

Fig. 19. SEM micrographs of A) MO1 and B) MO4 non-reduced powder catalysts after catalytic test at 700ºC-8h, 94,680 $mL \cdot g_{Cat}^{-1} \cdot h^{-1}$.

5.3.2. Test for reduced powdered catalysts.

Fig. 20. shows the DRM performance under the conditions of $CH_4/CO_2 = 1$, T = 600ºC, and a WHSV= 94,680 $mL \cdot g_{Cat}^{-1} \cdot h^{-1}$ for 8h. All the catalysts were previously reduced with a flow of H_2 at 700ºC for 1h. As seen in the characterization analysis, after a reductive treatment the materials present a reducibility at 700ºC greater than 60% or even reducibility greater than 90% for materials with Ce.

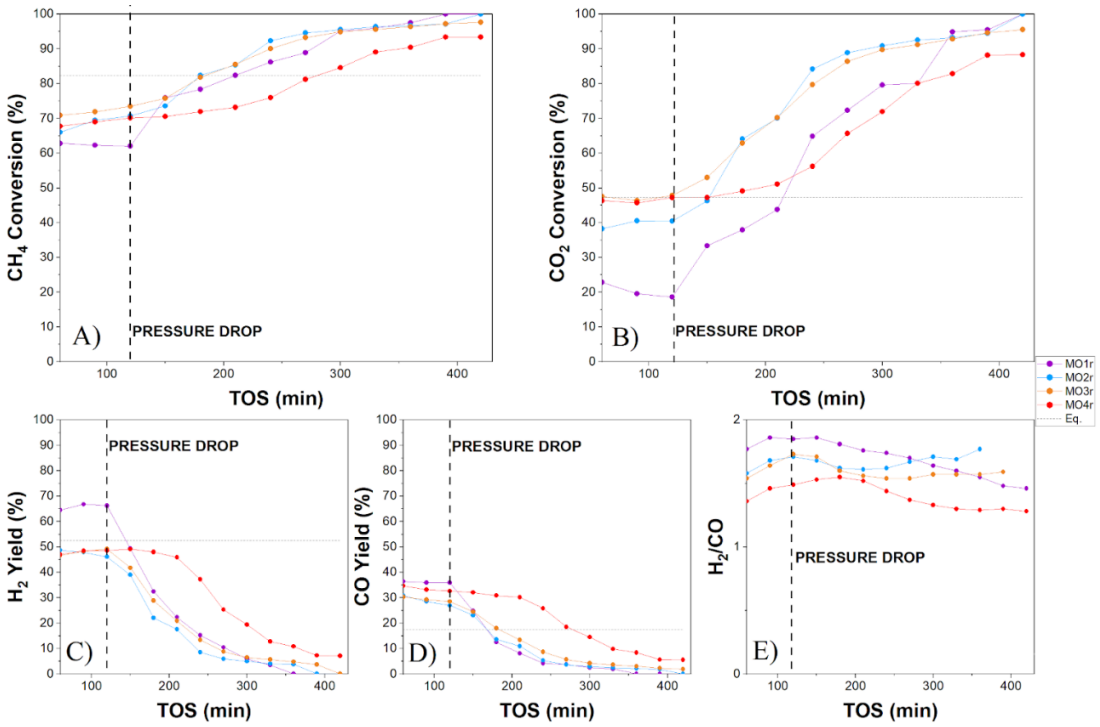

Fig. 20. Catalytic A) CH_4, B) CO_2 conversion; catalytic C) H_2, D) CO selectivity and E) H_2/CO vs. TOS for reduced powder catalysts. Reaction conditions: 600ºC-8h and 94,680 $mL \cdot g_{Cat}^{-1} \cdot h^{-1}$.

At the outset, the tests were intended to assess catalytic performance at 700°C. However, additional tests indicated that the catalysts reached thermodynamic equilibrium, making the differentiation challenging. To address this, 600°C was chosen to avoid equilibrium. Furthermore, at this temperature, the DRM conditions became more severe, promoting carbon-forming reactions and kinetically discouraging the DRM.[59], [145]

In the first 2 h of the reaction, MO1 and MO2 presented lower catalytic activity, which was attributed to the working temperature and high carbon production since the beginning of the reaction. In contrast, MO3 and MO4 presented the highest CH_4 and CO_2 conversions, indicating the stability of Ce against the accumulation of carbon in the catalyst owing to its synergetic effect with the basic sites. High H_2 production was observed with the MO1 catalyst, while the CO percentages for all catalysts remained in close ranges. During the first 2 h of the reaction, the H_2/CO ratio exceeded 1.4, indicating the strong occurrence of methane cracking at 600°C.[145]

After 2 hours, a progressive pressure drop was noticed owing to carbon formation, leading to erroneous conversion calculations with higher values and lower selectivity. This indicates reactor blockage, rather than deactivation. It is evident that the favored occurrence of methane cracking at 600°C was responsible for the carbon formation observed under the evaluated conditions.

The TGA and DSC results (**Fig. 21 – A and B**) show a significant and exothermic mass loss between 480 and 610 ºC, corresponding to the gasification of whiskers of carbon formed during the reaction. This confirms the reason for the pressure drop.

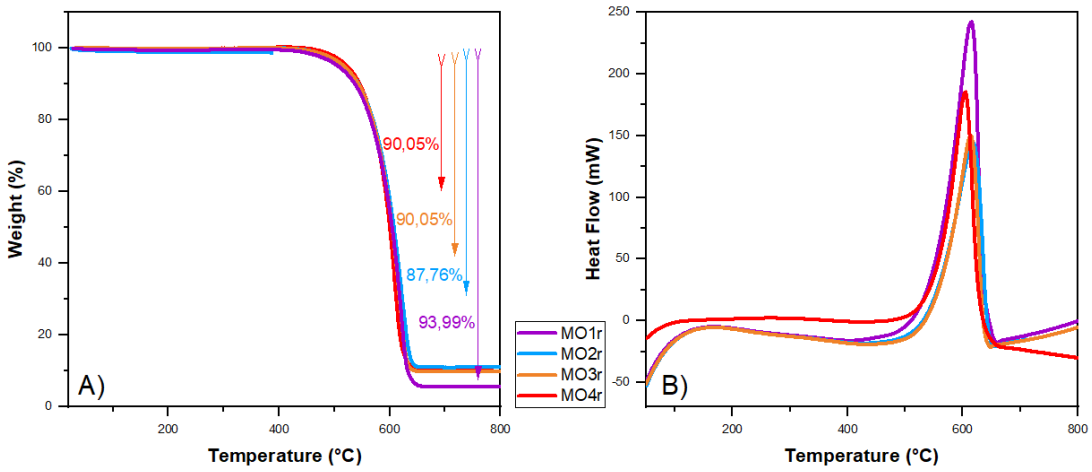

Fig. 21. A) TGA and B) DSC profiles for reduced powder catalysts. Reaction conditions: 700ºC-8h and 94,680 $mL \cdot g_{Cat}^{-1} \cdot h^{-1}$.

The previously reduced MO1 catalyst presented a slightly higher coke production of 0,1175 $g_C \cdot g_{Cat}^{-1} \cdot h^{-1}$, while there is no major difference in the coke production for the Ce-containing materials MO2, MO3, and MO4, previously reduced, obtaining 0.1097, 0.1125, and 0.1126 $g_C \cdot g_{Cat}^{-1} \cdot h^{-1}$, respectively. Thus, under these pretreatment and reaction conditions, no difference is evident between the catalysts obtained due to their high susceptibility to coke formation.

5.4. Catalytic test with immobilized mixed oxides

The activity, selectivity, and stability of the mixed oxides immobilized in cordierite monoliths are presented to compare their performance with that of powdered solids. Additionally, we will discuss the reusability of the structured mixed oxides.

5.4.1. Reactor's catalytic activity

In a variety of publications [149]–[153] authors have used FeCr alloy steel and cordierite material as structural supports or even reactors, in which null or very low activity is presumed. In the present work, this material has been chosen for reactor design due to its resistance against thermal and mechanical stresses, high thermal conductivity, and relatively low cost. To assess the potential influence of the FeCr alloy reactor and cordierite monolith on the catalytic test with structured mixed oxides, a bare cordierite monolith was loaded into the reactor and subjected to the same reaction conditions (CH_4/CO_2 = 1, 700°C for 8 h) as the immobilized mixed oxides.

As a result, in **Fig. 22 - A.**, the conversion values do not exceed 5% for CH_4 and 3 and 15% for CO_2. **Fig. 22 - B.** shows a null identification of H_2 and yield percentages for CO between 10 and 35%. The potential influence of the reactor material during the catalytic tests is negligible. The very low conversions observed are attributed to the consumption of CH_4 through the decomposition reaction, the RWGS reaction [154], in which CO_2 is consumed along with the possible H_2 formed during methane cracking. Furthermore, the absence of coke inside the reactor or the monolith after the test suggests the possibility of coke gasification by CO_2, which explains the increase in CO formation.

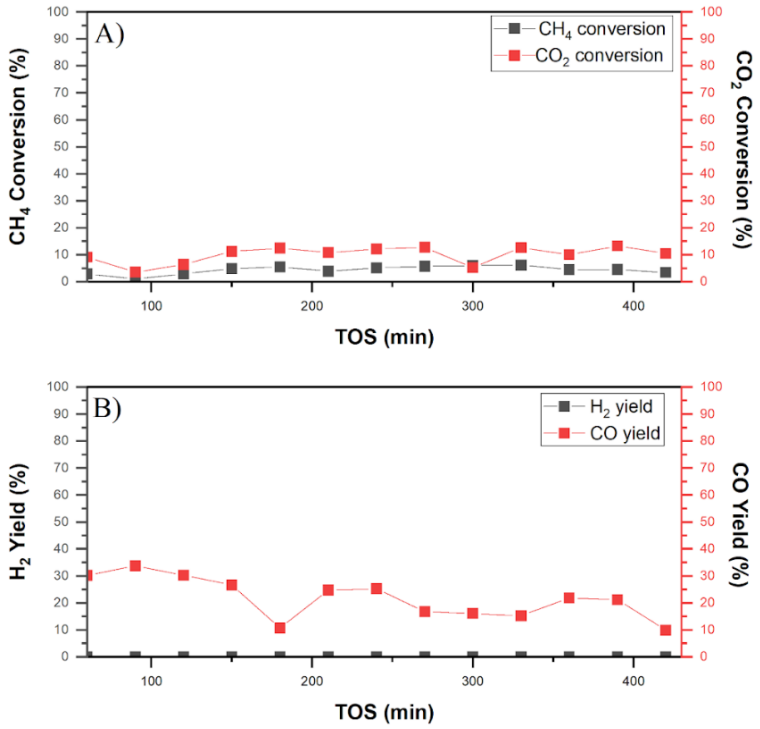

Fig. 22. Catalytic A) CH_4 and CO_2 conversion; catalytic C) H_2 and CO selectivity vs. TOS for metallic reactor with bare cordierite monolith. Reaction conditions: 700ºC-8h.

5.4.2. Tests for non-reduced immobilized catalysts

The catalytic performance for DRM of the different immobilized mixed oxides was evaluated under the same severe conditions used with the powdered mixed oxides (CH_4/CO_2 = 1, T = 700ºC, 8h). To compare the results more closely, despite the differences in the bed-catalytic volume, the amount of immobilized mixed oxide very close (0.025 g) to that used in the fixed-bed catalytic tests of the powders was sought, with which a WHSV of 94,680 $mL \cdot g_{Cat}^{-1} \cdot h^{-1}$ was achieved.

The results are shown in **Fig. 23.**, where is observed that the conversion of CH_4 is identical for all the immobilized catalysts, considering that the differences between the results are only between 2 and 3% after 8 h of reaction, with which the variations of Ce load that the catalysts have did not show a significant effect. Additionally, compared with the values obtained by the powder catalysts, an increase in the catalytic activity was observed for the conversion of

CH_4, with increases that varied between 8 and 18% for the final conversions after 8h of reaction.

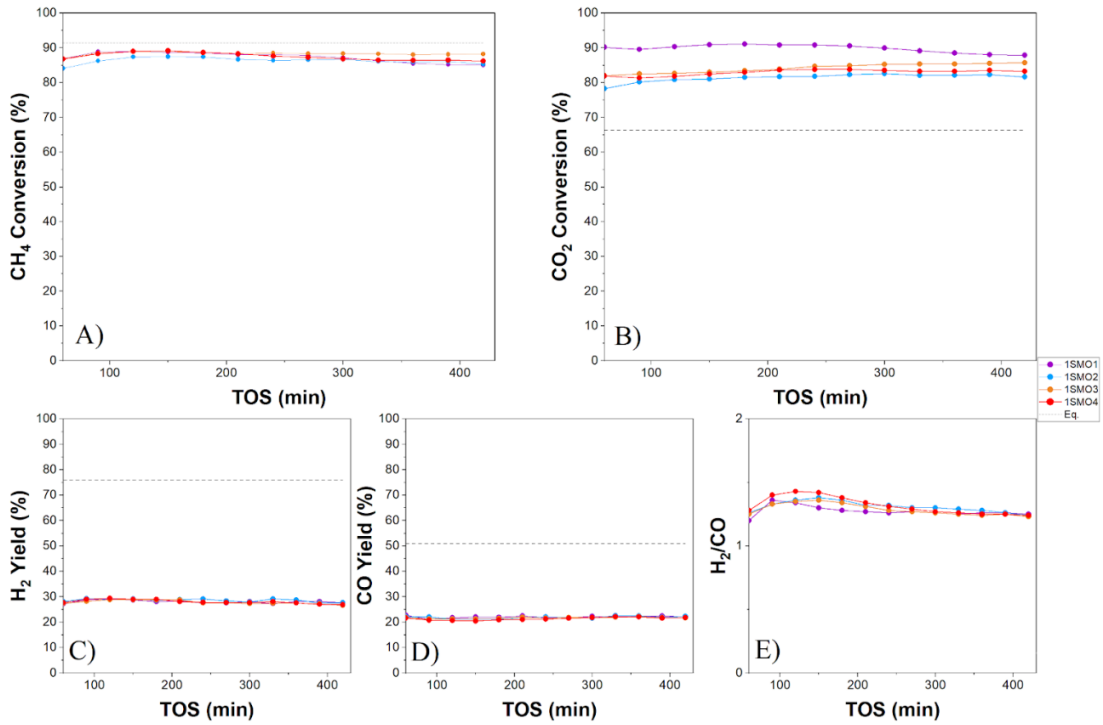

Fig. 23. Catalytic A) CH_4, B) CO_2 conversion; catalytic C) H_2, D) CO selectivity and E) H_2/CO vs. TOS for non-reduced catalysts structured in cordierite monoliths. Reaction conditions: 700ºC-8h, 94,680 $mL \cdot g_{Cat}^{-1} \cdot h^{-1}$.

Apropos of the CO_2 conversion (**Fig. 23 – B.**), all materials exceeded the values of the thermodynamic equilibrium because of side reactions or carbonate fixation.[59], [61] The immobilized mixed oxide that presented the highest conversion was the non-promoted material; however, no significant differences were observed. When comparing the results of the two presentations of the catalyst, it was observed that each catalyst tended to exhibit conversion stability during the 8h of reaction; however, the CO_2 conversion values obtained by the immobilized catalysts were higher, presenting an increase of between 10 and 20% after the 8h. Leba et al.[115] compared the performance of powder vs. catalysts immobilized in cordierite monoliths to determine the most efficient structural form for Ni-Co catalysts, showing results in which, the particulate catalysts immobilized in monoliths deliver higher conversions of CH_4 and CO_2. Luisetto et al.[103] contrasted powder catalysts with the same ones immobilized in monoliths, the last presented higher reagent conversions, attributing the result to a possible longer contact time of the reagents with the catalytic material allowed by the monolithic structure.

Fig. 23 – C, D, and **E.** show the yields of the desired products and H_2/CO ratio. All samples presented H_2 yield percentages between 27 and 28%, as well as CO, yield percentages between 21 and 22%, resulting in H_2/CO ratios of 1.2 throughout the catalytic test. The findings demonstrate that despite the higher conversions achieved by the monoliths compared to the powders, the yields were approximately 15% lower. This suggests a greater

occurrence of side reactions, particularly those forming carbon, such as methane cracking, which contribute to syngas with a ratio greater than 1. In addition, the RWGS reaction consumes part of the hydrogen formed during cracking.[15], [59], [145], [155]

The carbon content was determined by gravimetry, which confirmed the higher occurrence of carbon-forming reactions, in agreement with the measured yields. The non-promoted catalyst showed a higher final carbon content, which is consistent with the results obtained for the powdered catalysts. Carbon formation followed the order 1SMO1>1SMO2>1SMO3≈1SMO4, producing 0.4620, 0.4330, 0.3494, and 0.3556 $g_C \cdot g_{Cat}^{-1} \cdot h^{-1}$, respectively. These values were approximately four times higher than those of the powders. This indicates that the increased exposure of the catalyst on the monolith surface makes them more active but also more susceptible to carbon formation.

5.4.3. Reusability test of non-reduced immobilized catalysts

Considering the thermal stability of the synthesized mixed oxides and the cordierite monolithic structures, the potential for reusing the monolithic catalysts was explored. After new calcination at 700ºC - 1h in an air atmosphere to remove the carbon obtained from the previous test, the possibility of reusing the monoliths was assessed. The chosen calcination temperature ensured the removal of carbon without exceeding the temperature at which the mixed oxides were obtained.[60]

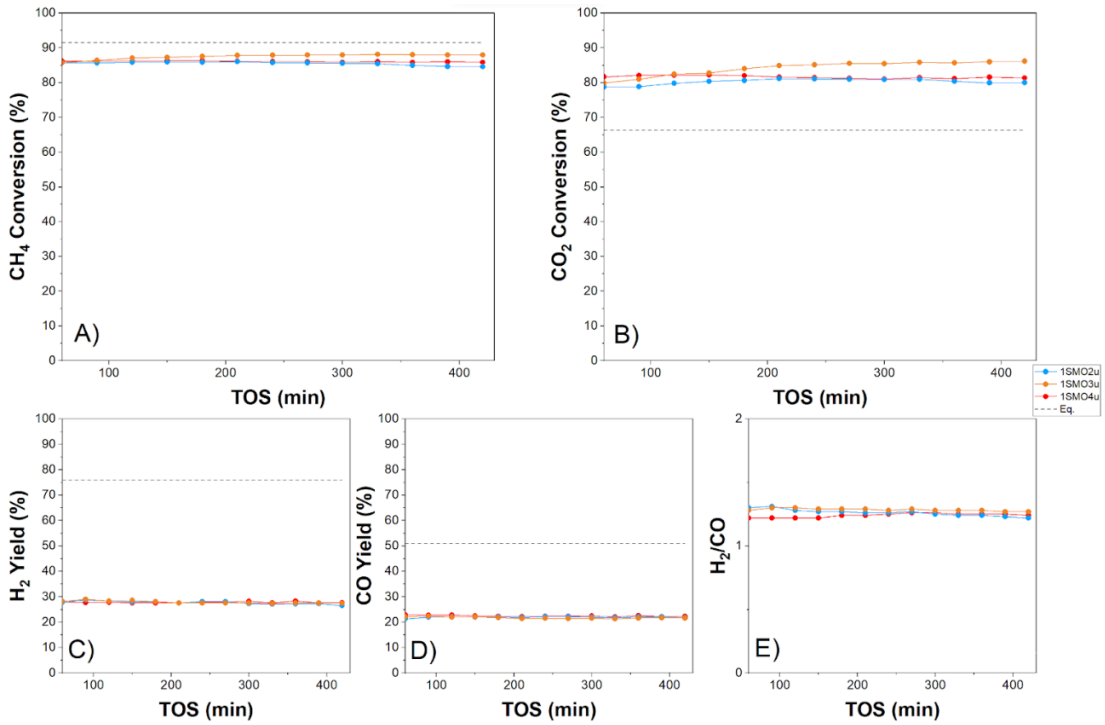

Fig. 24. Reusability tests A) CH_4, B) CO_2 conversion; catalytic C) H_2, D) CO selectivity and E) H_2/CO vs. TOS for non-reduced catalysts structured in cordierite monoliths. Reaction conditions: 700ºC-8h, 94,680 $mL \cdot g_{Cat}^{-1} \cdot h^{-1}$.

Fig. 24. shows the reusability test results for the Ce-promoted mixed oxides structured in the monoliths. The catalytic tests were carried out under the same conditions as those used in the previous reactions. As previously stated, the non-promoted catalyst was not subjected to this evaluation because the maximum amount of coke was obtained in the first catalytic test.

As a result, the high catalytic activity exhibited by the materials with respect to the conversion of CH_4 and CO_2 stands out, where all the reused materials reached conversions practically equal to those obtained in the first catalytic test. Similarly, the selectivity percentages for H_2 and CO obtained in the second catalytic test were highly like those reported in the previous catalytic test, producing syngas with an H_2/CO ratio of 1.2. All the above evidence the stability of the immobilized materials and their great potential against the DRM process.

Fig. 25. illustrates a comparison of carbon production between the first and second catalytic tests on mixed oxides structured in cordierite monoliths. The second catalytic test assessed the amount of carbon produced, yielding 0.5533, 0.375, and 0.3874 $g_C \cdot g_{Cat}^{-1} \cdot h^{-1}$ for 1SMO2, 1SMO3, and 1SMO4, respectively. The influence of Ce as a promoter is evident, as materials with higher Ce contents exhibit lower final coke production; as has been reported by other author.[23], [90] Notably, the materials subjected to a second catalytic test after recovery showed a slight increase in the final carbon obtained, which was lower in materials with higher promoter loads.

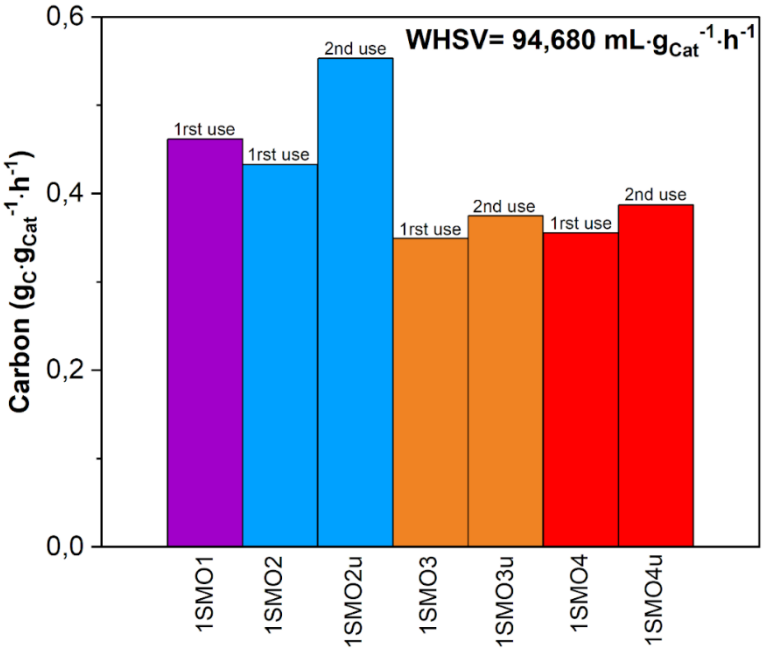

Fig. 25. Carbon production during the first and second catalytic tests on the mixed oxides structured in the cordierite monoliths.

SEM analysis, **Fig. 26**., was performed to study the surface morphology of the spent 1SMO2 catalyst after being reused for a second DRM process to understand the changes that these monolithic materials can undergo. In **Fig. 26 – A.**, cordierite walls covered by the mixed

oxide are observed, evidencing how a greater number of cracks were formed in the coating layer, apparently given the handling and the general conditions under which the oxide peels off. Surface of the monolith (see also **Fig. 26 - B.**). At a higher magnification (**Fig 26 - C.**), the carbonaceous structures formed on the surface after the second round of the reaction can be identified; where the carbon filament structures are clear, they are the same as those obtained when using the powder catalysts. This indicates that the carbon obtained during the DRM process does not vary if the structures are immobilized in the monoliths. Although a larger amount of carbon is formed on the monoliths than on the powdered catalyst, it does not obstruct the channels of the structure nor leads to catalyst deactivation.

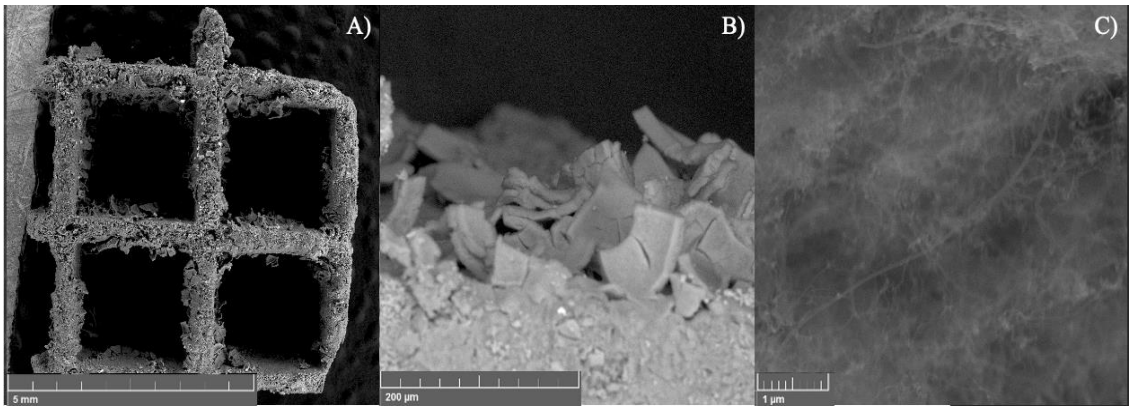

Fig. 26. SEM micrographs of the structured MO2 after being used for a DRM at 700ºC-8h, calcinated, and reused for a new reforming reaction.

5.4.4. Test for non-reduced immobilized catalysts with a higher load of catalyst

The synthesized mixed oxides were highly active during the DRM process. However, even with the addition of the promoter, significant carbon formation occurred owing to side reactions. Previous tests have found that using 25 mg of powdered catalyst in a fixed-bed reactor is suitable for studying catalytic performance under available laboratory conditions. Using larger amounts of catalyst leads to pressure drops due to high carbon formation. To address this, we proposed an evaluation using monoliths with a four-fold higher load (100 mg) of immobilized mixed oxides, reducing the WHSV fourfold.

Fig. 27. shows the results where the methane conversions are similar for all catalysts and are between 82 and 90%, values that, when compared with the powder catalysts and monoliths with 0.025 g loaded, are slightly higher and closer to the conversion value of thermodynamic equilibrium. The CO_2 conversion percentages between 79 and 85% after 8 h of reaction demonstrate, like all the previously evaluated catalysts, results that exceed the equilibrium conversion values. In the first hours of the reaction, the catalysts showed insignificant differences, but when approaching 8h of reaction, their differences decreased, differentiating by less than 7%. Regarding the percentages of selectivity of H_2 and CO, the results vary between 41–46% and 29–31%, respectively, after 8 h of reaction for all materials. H_2/CO ratios between 1.3 and 1.5 were obtained. Up until now, the materials that presented the highest values of H_2/CO.

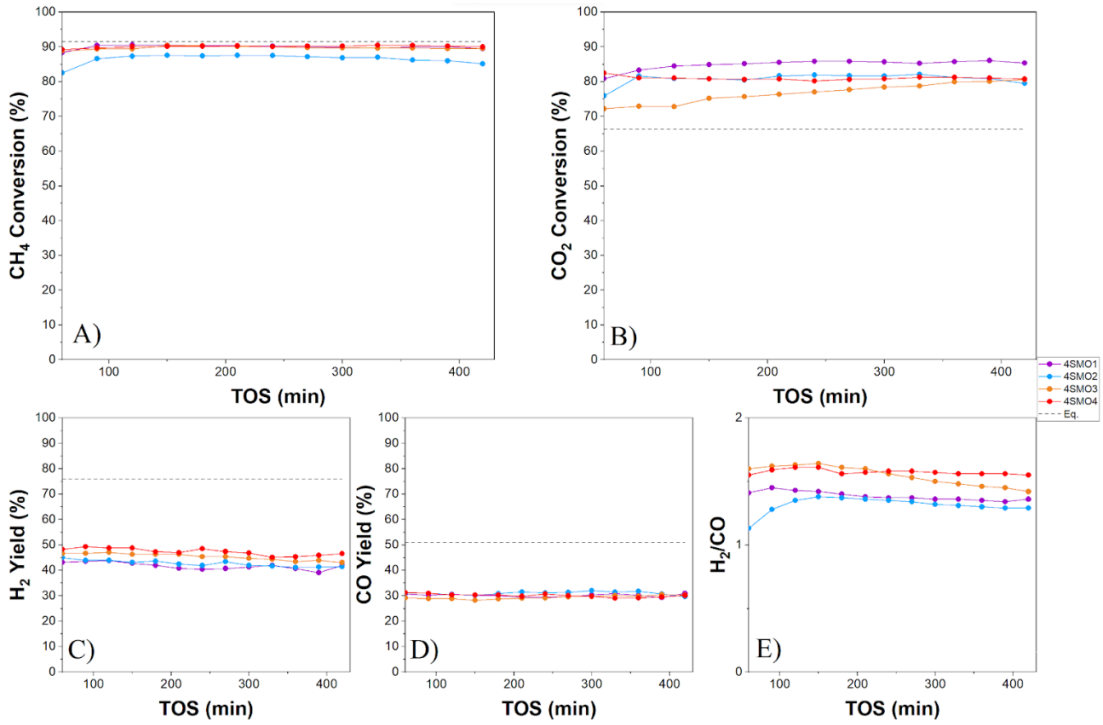

Fig. 27. Catalytic A) CH_4, B) CO_2 conversion; catalytic C) H_2, D) CO selectivity and E) H_2/CO vs. TOS for non-reduced catalysts structured in cordierite monoliths. Reaction conditions: 700ºC-8h WHSV = 23,679 $mL \cdot g_{Cat}^{-1} \cdot h^{-1}$.

The carbon amounts obtained for these catalysts after the DRM process were as follows: 0.1868 $g_C \cdot g_{Cat}^{-1} \cdot h^{-1}$ for 4SMO1, 0.1378 $g_C \cdot g_{Cat}^{-1} \cdot h^{-1}$ for 4SMO2, 0.1219 $g_C \cdot g_{Cat}^{-1} \cdot h^{-1}$ for 4SMO3, and 0.1171 $g_C \cdot g_{Cat}^{-1} \cdot h^{-1}$ for 4SMO4. **Fig. 28.** allows a graphical comparison of the final carbon obtained by the non-reduced powder catalysts, and non-reduced immobilized catalysts.

Notably, the largest amount of carbon was obtained with 0.025 g of loaded monoliths. This finding, combined with the similar catalytic performance among the materials, suggests that even with an increased amount of immobilized mixed oxide in the monoliths, only a limited fraction is directly exposed to the reaction flow. Nevertheless, this exposed fraction serves as the active site for catalyzing DRM and carbon formation reactions. Moreover, it became evident that the presence of Ce, as observed in all the tests, led to a reduction in the mass of coke formed as its concentration in the solids increased. This phenomenon is attributed to the role of the Ce^{4+}/Ce^{3+} redox pair in carbon gasification, as demonstrated by Daza et al.[28], [96], [97]

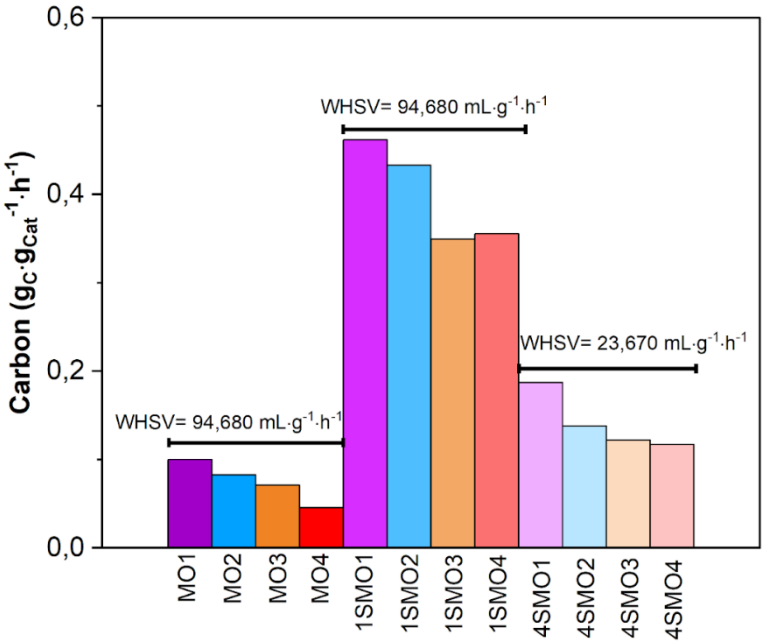

Fig. 28. Carbon production during catalytic tests on the non-reduced powder mixed oxides and non-reduced catalysts structured in the cordierite monoliths at several WHSV.

5.4.5. Tests for reduced immobilized catalysts with a higher load of catalysts.

The catalytic performance of powdered mixed oxides previously subjected to reduction with a flow of H_2 at 700°C for 1 h and then reacted at 600°C was evaluated. The results revealed significant coke production in all the materials, leading to blockage of the fixed-bed reactor system shortly after the reaction began. To address this issue, a new approach was proposed to test the stability of monolithic systems. This involved using a higher catalyst load, resulting in a lower WHSV while also conducting a prior reduction at 600°C. The goal was to establish more challenging conditions for the catalysts and assess their performances under these circumstances.

All catalysts presented more lasting stability under the reaction conditions than the reduced powdered catalysts (see **Fig. 29.**), where the only catalytic system that presented pressure drops (after 7h of reaction) was the one obtained with the non-promoted mixed oxide, evidencing its disadvantage compared to the promoted catalysts. This greater stability of the monolithic structures reveals their potential superiority, since even if they have a greater contact time between the catalyst and the reaction mixture [103], the formation of coke that causes pressure drops is not a main concern for these structures, as has been suggested by some authors. [15]

The Ce-promoted immobilized catalysts exhibited CH_4 conversion values between 71 and 74% after an 8h reaction, demonstrating their high activity even at 600°C. However, the CO_2 conversions are like those of reduced powdered mixed oxides, which are the lowest among all the systems evaluated. Regarding product selectivity, the immobilized materials showed

higher H_2 yield percentages than the reduced powdered catalysts, while the CO yield percentages were like those of the reduced powder catalysts. The H_2/CO ratios for these structured catalysts range between 1.7 and 2.0 after 8 h of reaction, indicating the strong influence of methane cracking at 600°C, which explains the high coke formation observed.[8], [9], [11]

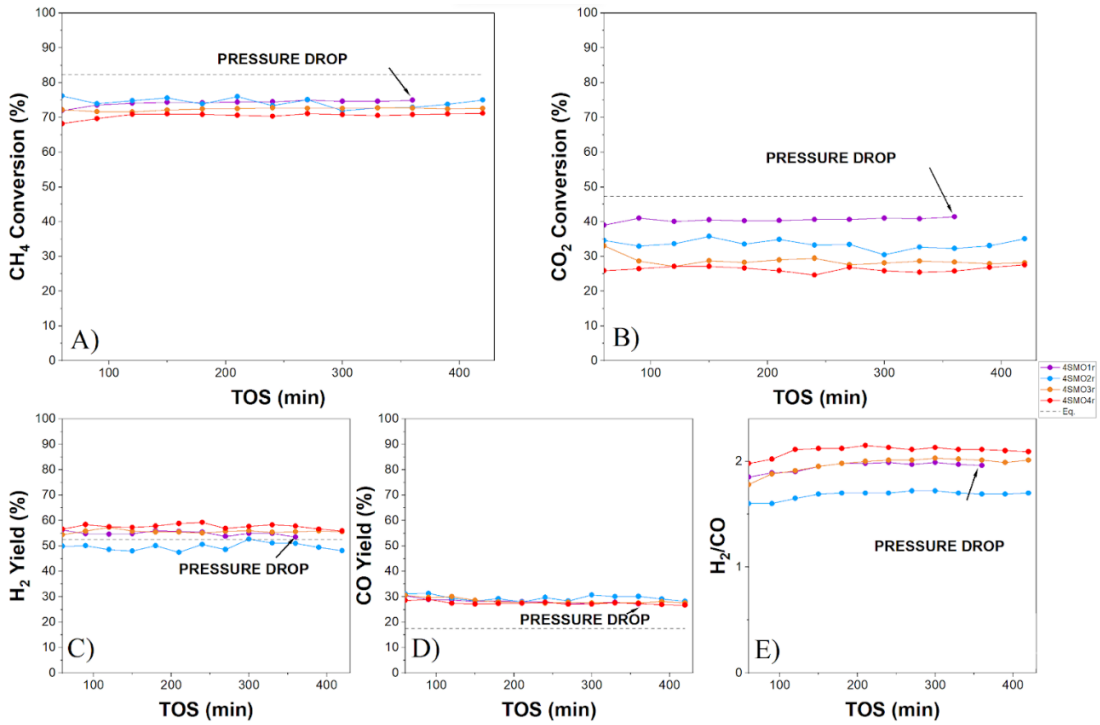

Fig. 29. Catalytic A) CH_4, B) CO_2 conversion; catalytic C) H_2, D) CO selectivity and E) H_2/CO vs. time on stream. For mixed oxides structured in cordierite monoliths, with the previous reduction with H_2 flow at 700ºC-1h. Reaction conditions: 600ºC-8h, 23679 $mL \cdot gCat^{-1} \cdot h_{rxn}^{-1}$.

Finally, after determining the amount of carbon obtained, the following results were calculated at the end of the reaction: 4SMO1 = 0.9932 $g_C \cdot g_{Cat}^{-1} \cdot h^{-1}$, 4SMO2 = 0.9116 $g_C \cdot g_{Cat}^{-1} \cdot h^{-1}$, 4SMO3 = 0.5937 $g_C \cdot g_{Cat}^{-1} \cdot h^{-1}$, and 4SMO4 = 0.5862 $g_C \cdot g_{Cat}^{-1} \cdot h^{-1}$. These high quantities are a consequence of several factors, including the greater availability of active sites in the catalyst due to the previous reduction, the higher quantity of catalyst used, and the larger area of continuous catalyst flow of reagents offered by the monolithic reactor.[8], [11], [15], [61], [65], [72]

Fig. 30. graphically compares these results with those obtained for the powder-reduced mixed oxides, clearly showing a significant increase in carbon obtained by the monolithic catalysts. Once again, the superiority of catalysts structured in monoliths is evident because, despite the high carbon formation, they are less prone to blockages and pressure drops.[104], [113], [149]

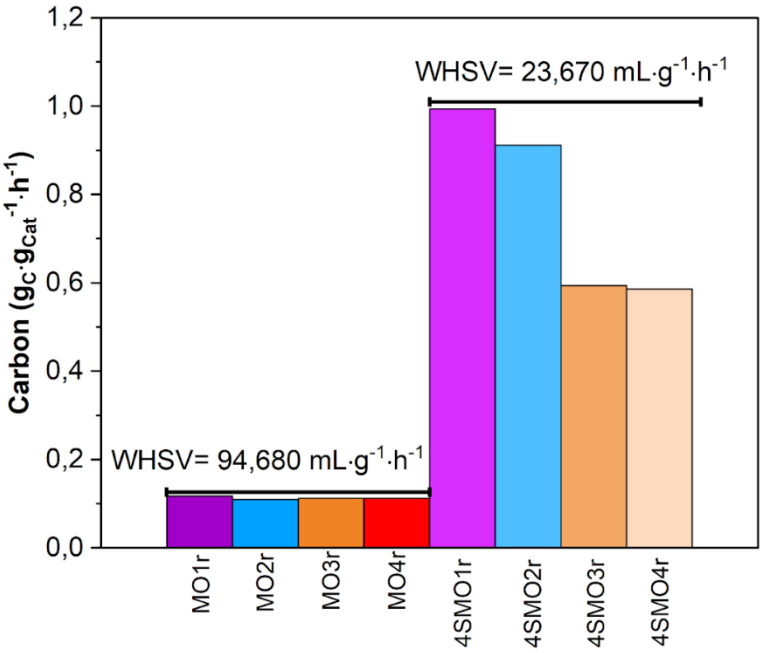

Fig. 30. Carbon production during catalytic tests on the reduced powder mixed oxides and reduced catalysts structured in the cordierite monoliths. Reaction at 600 °C.

5.4.6. Comparative final analysis

Considering the various reaction conditions used in the literature when studying the DRM process, comparing the catalytic activity and selectivity with other research papers is not an easy task. That is why in the present work, tables (**Table 5.** and **Table 7.**) of a bibliographical compendium were made, in which research that is like the one carried out in this thesis was chosen, in order to differentiate and identify contributions to the literature that can be offered. Additionally, to have a general idea of the performance of the catalysts obtained in this work, in the supplementary information section, a compendium table (**Table S1.**) is exposed with conversion values, yield, and H_2/CO ratio for all exposed catalysts in this text.

Starting with the powdered catalysts, in two of their papers Daza et al.[28], [95] studied catalysts derived from hydrotalcites, promoted with Ce and evaluated catalytically after a reduction pretreatment at 700ºC or in a range of 500 to 700ºC (see **Table 5.**); In these works, the authors obtained CH_4 and CO_2 conversions between 75-90% and greater than 80% respectively at 700ºC, mentioning that the increase in the Ce load promoted physicochemical characteristics of the materials and therefore their catalytic activity. After the catalytic test, Daza et al.[28] calculated the amount of coke obtained by the catalysts, obtaining values of 1.80, 3.20, 3.80 and 10.5 $g_C \cdot g_{Cat}^{-1} \cdot h^{-1}$ for materials with Al/Ce ratios 26.90, 9.40, 4.29, 1.78 respectively, evidencing an increase in carbon as the Ce load increases. Higher carbon formations than for the catalysts of the present work (see **Fig. 28.** and **Fig. 30.);** however, the comparison must consider variables such as: the absence of prior reduction, the lowest reaction temperature, and the variations in Ni, Mg, and Al content of the catalysts.
On the other hand, Ren et al.[88] show catalysts with similar characteristics that did not exceed CH_4 conversion values of 60% or CO_2 conversion values of 70%, but that demonstrate

their potential for reusability for a subsequent DRM process without significantly modifying their catalytic performance. Additionally, Lino et al.[23] and Kalai et al.[85] reported the catalytic performance of Ni/Mg/Al/Ce catalysts (see **Table 5.**) with CH_4 conversion values of 10-50% and CO_2 of 40-80%, along with H_2/CO close to 0.7. Comparing the above with the results of this work (see **Table S1.**), it can be seen that the CH_4 and CO_2 conversion values are within the ranges obtained by the aforementioned authors, even in the case in which the powder catalysts were not previously reduced, as well as H_2/CO ratio values very close to 1 were obtained with very little variation between them, highlighting that the promoting effect of Ce was not specifically evidenced in the physicochemical characteristics of the materials, but in the ability to reduce the formation of coke in the catalysts, taking into account the particular reaction conditions to which the catalysts were subjected.

Linen et al.[23] additionally, determined the carbon deposition rates, with which for catalysts with a load of 25%wt. Ni not promoted and promoted with Ce, they presented values a little higher than 0.35 and 0.25 $g_C \cdot h^{-1}$ respectively. Research that shows a greater stability against the formation of carbon when adding the promoter, as also exposed in the present work.

Now, considering the catalysts immobilized in monoliths, a clearer and more evident comparison can be seen by looking at **Table 7.** and **Table 2S.** with which it can be noted that the catalysts synthesized for this work have conversion, selectivity ranges and H_2/CO ratios close to or in some cases higher than those reported in the literature. Along with the above, although an extensive study of the coke obtained in immobilized catalysts has not been reported, it can be observed that the type of coke obtained presents similar characteristics to those reported by authors such as Luisetto et al.[103] and Chava et al.[128].

Since the reusability potential of structured catalysts, designed for DRM, was not found in the literature, the work developed in this investigation can be taken as a favorable contribution by exposing how the structured materials underwent a second DRM process under the same conditions with very good stability and minimal variation in their catalytic performance.

6. CONCLUSIONS

This research work has been oriented to the study of Ce-promoted Ni-Mg-Al mixed oxide catalysts evaluated as powdered or immobilized in cordierite monoliths catalysts, for DRM reaction. By the results obtained, and considering the proposed objectives, this work allows us to draw the following general conclusions:

1. The coprecipitation method for obtaining hydrotalcite precursors allows the simple obtaining of the solids and the joint obtaining, by slurry coating, of the solids immobilized in monoliths. From these conventional methods, the easy immobilization of the entire catalytic system (active phase, support, and promoter precursors) at once is exposed without the need to add steps to the process; only needing a final stage of calcination to complete the complete synthesis of powdered and immobilized oxides. In addition to exposing the non-necessity of using adherent species to achieve the adhesion of the mixed oxide to the surface of the cordierite monoliths.

2. The promoting effect of Ce on the physicochemical properties of the catalysts was verified, since an increase in the ceria content allows: i) Obtaining catalysts with a smaller crystallite size for solids with a Ce load greater than 6.52 wt .% , ii) promoting the reduction of Ni, avoiding the formation of very high stability phases and supporting the reduction thanks to the existence of the Ce^{3+}/Ce^{4+} redox pairs, iii) promote an in the CO_2 adsorption capacity, and iv) the formation of smaller Ni^0 particle sizes, highlighting the decreased particle size of the material with the highest Ce charge (MO4 = 5.20nm).

3. The approach to the immobilized mixed oxides show that: i) The methods for obtaining the mixed oxides supported on the cordierite monoliths, which involve a treatment at high temperatures, did not mean a change in the crystalline structure of the monoliths; and ii) the formation of a layer of mixed oxides over the surface of the monoliths, with an average thickness of 6.13μm for monoliths with ~25mg of immobilized mixed oxide and an average layer thickness of 9.87μm for monoliths with ~100mg of immobilized mixed oxide.

4. All catalysts were active in the DRM reaction, without a direct correlation to the Ce load on activity, but on stability, since Ce promotes more efficient coke gasification. It was possible to establish that materials with an amount of Ce of 6.52 wt.% in the catalysts, without previous reduction for the DRM process, express a high catalytic stability and drastically reduce the formation of C-deposits in comparison with the other solids with a lower load of Ce.

5. Regarding the influence of immobilizing the mixed oxides in the monolithic structures, a highly active catalytic performance was observed for the DRM, where there was no variation in the conversion of the reagents and a slight decrease in the selectivity of the synthesis gas products, but still keeping H_2/CO ratios close to 1.2 with monoliths used with a WHVS = 94,680 $mL \cdot g_{Cat}^{-1} \cdot h^{-1}$ and H_2/CO ratios between 1.2 and 2.0 (for catalytic tests with prior reduction of the material) with monoliths used with a WHVS = 23,670 $mL \cdot g_{Cat}^{-1} \cdot h^{-1}$.

6. The formation of carbonaceous deposits in the form of carbon filaments was verified. The results evidenced the superiority of monolithic structures to avoid pressure drops due to blocking with coke over powder catalyst systems used in fixed-bed reactors.

7. The inclusion of Ce diminished coke formation, particularly in immobilized catalysts. Higher WHSV values resulted in more coke production, with a stronger effect observed when the catalyst was reduced and the reaction conducted at 600°C, compared to non-reduced conditions at 700°C.
8. After reusing the catalysts immobilized in monoliths, following a first DRM test, carbon elimination through calcination, and a second DRM catalytic test, their catalytic performance and stability remained nearly identical to the initial test. This demonstrates their high stability, recovery capacity, and potential for scaling in an industrial environment.

7. PERSPECTIVES

The following is advised as a result of this research's conclusion and for upcoming studies:

1. Carry out a textural analysis of the solids to complement the characterization information.
2. Carry out longer stability experiments, to have more information on the stability os the catalysts.
3. Carry out a great number of experiments combining variables.
4. Explore other methods to immobilize the catalysts in the monoliths to improve the reproducibility of the obtained materials.

REFERENCES

[1] H. H. Cho, V. Strezov, and T. J. Evans, "A review on global warming potential, challenges and opportunities of renewable hydrogen production technologies," *Sustainable Materials and Technologies*, vol. 35, Apr. 2023, doi: 10.1016/j.susmat.2023.e00567.

[2] M. Tsangas, I. Papamichael, and A. A. Zorpas, "Sustainable Energy Planning in a New Situation," *Energies (Basel)*, vol. 16, no. 4, Feb. 2023, doi: 10.3390/en16041626.

[3] J. C. J. Bart, N. Palmeri, and S. Cavallaro, "Evolution of biodiesel and alternative diesel fuels," in *Biodiesel Science and Technology*, Elsevier, 2010, pp. 713–782. doi: 10.1533/9781845697761.713.

[4] T. J. Mazanec, R. Prasad, R. Odegard, C. Steyn, and E. T. Robinson, "Oxygen transport membranes for syngas production," in *Studies in Surface Science and Catalysis*, Elsevier Inc., 2001, pp. 147–152. doi: 10.1016/s0167-2991(01)80295-0.

[5] P. Gupta, L. G. Velazquez-Vargas, and L. S. Fan, "Syngas redox (SGR) process to produce hydrogen from coal derived syngas," *Energy and Fuels*, vol. 21, no. 5, pp. 2900–2908, Sep. 2007, doi: 10.1021/ef060512k.

[6] P. C. Munasinghe and S. K. Khanal, "Biomass-derived syngas fermentation into biofuels: Opportunities and challenges," *Bioresource Technology*, vol. 101, no. 13. pp. 5013–5022, Jul. 2010. doi: 10.1016/j.biortech.2009.12.098.

[7] D. J. Roddy, "A syngas network for reducing industrial carbon footprint and energy use," *Appl Therm Eng*, vol. 53, no. 2, pp. 299–304, 2013, doi: 10.1016/j.applthermaleng.2012.02.032.

[8] K. Wittich, M. Krämer, N. Bottke, and S. A. Schunk, "Catalytic Dry Reforming of Methane: Insights from Model Systems," *ChemCatChem*, vol. 12, no. 8. Wiley Blackwell, pp. 2130–2147, Apr. 20, 2020. doi: 10.1002/cctc.201902142.

[9] J. Gao, Z. Hou, H. Lou, and X. Zheng, *Dry (CO2) Reforming*, First Edit. Elsevier, 2011. doi: 10.1016/B978-0-444-53563-4.10007-0.

[10] S. Aouad *et al.*, "A Review on the Dry Reforming Processes for Hydrogen Production: Catalytic Materials and Technologies," in *Frontiers in Ceramic Science Catalytic Materials for Hydrogen Production and Electro-oxidation Reactions*, 2018, pp. 60–128. doi: 10.2174/9781681087580118020007.

[11] M. Usman, W. M. A. Wan Daud, and H. F. Abbas, "Dry reforming of methane: Influence of process parameters - A review," *Renewable and Sustainable Energy Reviews*, vol. 45. Elsevier Ltd, pp. 710–744, 2015. doi: 10.1016/j.rser.2015.02.026.

[12] A. Abdulrasheed, A. A. Jalil, Y. Gambo, M. Ibrahim, H. U. Hambali, and M. Y. Shahul Hamid, "A review on catalyst development for dry reforming of methane to syngas: Recent advances," *Renewable and Sustainable Energy Reviews*, vol. 108. Elsevier Ltd, pp. 175–193, Jul. 01, 2019. doi: 10.1016/j.rser.2019.03.054.

[13] L. S. Neiva, "A Study On The Characteristics Of The Reforming Of Methane: A Review," *Brazilian Journal of Petroleum and Gas*, pp. 119–127, Sep. 2010, doi: 10.5419/bjpg2010-0013.

[14] Y. H. Hu, "Advances in catalysts for CO2 reforming of methane," *ACS Symposium Series*, vol. 1056, pp. 155–174, 2010, doi: 10.1021/bk-2010-1056.ch010.

[15] O. Muraza and A. Galadima, "A review on coke management during dry reforming of methane," *Archives of Thermodynamics*, vol. 33, no. 4, pp. 23–40, 2014, doi: 10.1002/er.

[16] R. J. Zhang, G. F. Xia, M. F. Li, Y. Wu, H. Nie, and D. D. Li, "Effect of support on catalytic performance of Ni-based catayst in methane dry reforming," *Ranliao Huaxue Xuebao/Journal of Fuel Chemistry and Technology*, vol. 43, no. 11, pp. 1359–1365, 2015, doi: 10.1016/S1872-5813(15)30040-2.

[17] M. Chaghouri, C. Ciotonea, F. Cazier, L. H. Tidahy, C. Gennequin, and E. Abi-Aad, "Hydrogen production through dry reforming of biogas on hydrotalcite derived materials," in *2022 13th International Renewable Energy Congress, IREC 2022*, Institute of Electrical and Electronics Engineers Inc., 2022. doi: 10.1109/IREC56325.2022.10002063.
[18] C. E. Daza, A. Kiennemann, S. Moreno, and R. Molina, "Dry reforming of methane using Ni-Ce catalysts supported on a modified mineral clay," *Appl Catal A Gen*, vol. 364, no. 1–2, pp. 65–74, 2009, doi: 10.1016/j.apcata.2009.05.029.
[19] R. Guil-López, V. La Parola, M. A. Peña, and J. L. G. Fierro, "Evolution of the Ni-active centres into ex hydrotalcite oxide catalysts during the CO x-free hydrogen production by methane decomposition," in *International Journal of Hydrogen Energy*, Apr. 2012, pp. 7042–7055. doi: 10.1016/j.ijhydene.2011.11.083.
[20] A. Chatla, F. Abu-Rub, A. V. Prakash, G. Ibrahim, and N. O. Elbashir, "Highly stable and coke-resistant Zn-modified Ni-Mg-Al hydrotalcite derived catalyst for dry reforming of methane: Synergistic effect of Ni and Zn," *Fuel*, vol. 308, Jan. 2022, doi: 10.1016/j.fuel.2021.122042.
[21] W. Y. Kim, J. S. Jang, E. C. Ra, K. Y. Kim, E. H. Kim, and J. S. Lee, "Reduced perovskite LaNiO3 catalysts modified with Co and Mn for low coke formation in dry reforming of methane," *Appl Catal A Gen*, vol. 575, no. November 2018, pp. 198–203, 2019, doi: 10.1016/j.apcata.2019.02.029.
[22] X. Cai and Y. H. Hu, "Advances in catalytic conversion of methane and carbon dioxide to highly valuable products," *Energy Science and Engineering*, vol. 7, no. 1. John Wiley and Sons Ltd, pp. 4–29, Feb. 01, 2019. doi: 10.1002/ese3.278.
[23] A. V. P. Lino, E. M. Assaf, and J. M. Assaf, "Hydrotalcites derived catalysts for syngas production from biogas reforming: Effect of nickel and cerium load," *Catal Today*, vol. 289, pp. 78–88, 2017, doi: 10.1016/j.cattod.2016.08.022.
[24] O. H. Ojeda-Niño, F. Gracia, and C. Daza, "Role of Pr on Ni-Mg-Al Mixed Oxides Synthesized by Microwave-Assisted Self-Combustion for Dry Reforming of Methane," *Ind Eng Chem Res*, vol. 58, no. 19, pp. 7909–7921, May 2019, doi: 10.1021/acs.iecr.9b00557.
[25] S. Govender and H. B. Friedrich, "Monoliths: A review of the basics, preparation methods and their relevance to oxidation," *Catalysts*, vol. 7, no. 2. MDPI, Feb. 16, 2017. doi: 10.3390/catal7020062.
[26] J. L. Williams, "Monolith structures, materials, properties and uses," 2001.
[27] S. Govender and H. B. Friedrich, "Monoliths: A review of the basics, preparation methods and their relevance to oxidation," *Catalysts*, vol. 7, no. 2, 2017, doi: 10.3390/catal7020062.
[28] C. E. Daza, S. Moreno, and R. Molina, "Co-precipitated Ni-Mg-Al catalysts containing Ce for CO2 reforming of methane," *Int J Hydrogen Energy*, vol. 36, no. 6, pp. 3886–3894, Mar. 2011, doi: 10.1016/j.ijhydene.2010.12.082.
[29] J. Jiang, B. Ye, and J. Liu, "Research on the peak of CO2 emissions in the developing world: Current progress and future prospect," *Applied Energy*, vol. 235. Elsevier Ltd, pp. 186–203, Feb. 01, 2019. doi: 10.1016/j.apenergy.2018.10.089.
[30] W. F. Lamb *et al.*, "A review of trends and drivers of greenhouse gas emissions by sector from 1990 to 2018," *Environmental Research Letters*, vol. 16, no. 7. IOP Publishing Ltd, Jul. 01, 2021. doi: 10.1088/1748-9326/abee4e.
[31] G. Grassi *et al.*, "Reconciling global-model estimates and country reporting of anthropogenic forest CO2 sinks," *Nat Clim Chang*, vol. 8, no. 10, pp. 914–920, Oct. 2018, doi: 10.1038/s41558-018-0283-x.
[32] P. Friedlingstein *et al.*, "Global carbon budget 2019," *Earth Syst Sci Data*, vol. 11, no. 4, pp. 1783–1838, Dec. 2019, doi: 10.5194/essd-11-1783-2019.
[33] S. Kirschke *et al.*, "Three decades of global methane sources and sinks," *Nature Geoscience*, vol. 6, no. 10. pp. 813–823, Oct. 2013. doi: 10.1038/ngeo1955.

[34] M. Saunois *et al.*, "The global methane budget 2000-2017," *Earth Syst Sci Data*, vol. 12, no. 3, pp. 1561–1623, Jul. 2020, doi: 10.5194/essd-12-1561-2020.
[35] G. Janssens-Maenhout *et al.*, "EDGAR v4.3.2 Global Atlas of the three major Greenhouse Gas Emissions for the period 1970-2012", doi: 10.5194/essd-2017-79.
[36] H. Tian *et al.*, "A comprehensive quantification of global nitrous oxide sources and sinks," *Nature*, vol. 586, no. 7828, pp. 248–256, Oct. 2020, doi: 10.1038/s41586-020-2780-0.
[37] A. Kumar, P. Singh, P. Raizada, and C. M. Hussain, "Impact of COVID-19 on greenhouse gases emissions: A critical review," *Science of the Total Environment*, vol. 806. Elsevier B.V., Feb. 01, 2022. doi: 10.1016/j.scitotenv.2021.150349.
[38] H. Ritchie, M. Roser, and P. Rosado, "CO_2 and Greenhouse Gas EmissionsRetrieved," *Our World in Data*, 2022, Accessed: Jan. 30, 2023. [Online]. Available: https://ourworldindata.org/co2-and-other-greenhouse-gas-emissions
[39] J. G. J. Olivier and J. A. H. W. Peters, "TRENDS IN GLOBAL CO 2 AND TOTAL GREENHOUSE GAS EMISSIONS 2020 Report Trends in global CO2 and total greenhouse gas emissions: 2020 Report," 2020. [Online]. Available: www.pbl.nl/en.
[40] M. Roelfsema *et al.*, "Taking stock of national climate policies to evaluate implementation of the Paris Agreement," *Nat Commun*, vol. 11, no. 1, Dec. 2020, doi: 10.1038/s41467-020-15414-6.
[41] L. Aleluia Reis and M. Tavoni, "Glasgow to Paris—The impact of the Glasgow commitments for the Paris climate agreement," *iScience*, vol. 26, no. 2, p. 105933, Feb. 2023, doi: 10.1016/j.isci.2023.105933.
[42] Z. Yu, I. Lanre Ridwan, A. ur R. Irshad, M. Tanveer, and S. A. R. Khan, "Investigating the nexuses between transportation Infrastructure, renewable energy Sources, and economic Growth: Striving towards sustainable development," *Ain Shams Engineering Journal*, Mar. 2022, doi: 10.1016/j.asej.2022.101843.
[43] J. Hardoy and P. Romero Lankao, "Latin American cities and climate change: Challenges and options to mitigation and adaptation responses," *Current Opinion in Environmental Sustainability*, vol. 3, no. 3. pp. 158–163, May 2011. doi: 10.1016/j.cosust.2011.01.004.
[44] D. Delgado Pugley, "América Latina frente a la COP26 Posiciones y perspectivas," 2021.
[45] F. D. Meylan, V. Moreau, and S. Erkman, "CO2 utilization in the perspective of industrial ecology, an overview," *Journal of CO2 Utilization*, vol. 12, pp. 101–108, 2015, doi: 10.1016/j.jcou.2015.05.003.
[46] D. Cebrucean, V. Cebrucean, and I. Ionel, "CO2 capture and storage from fossil fuel power plants," *Energy Procedia*, vol. 63, no. ii, pp. 18–26, 2014, doi: 10.1016/j.egypro.2014.11.003.
[47] H. Yang *et al.*, "Progress in carbon dioxide separation and capture: A review," *Journal of Environmental Sciences*, vol. 20, no. 1, pp. 14–27, 2008, doi: 10.1016/S1001-0742(08)60002-9.
[48] M. Bui *et al.*, "Carbon capture and storage (CCS): The way forward," *Energy Environ Sci*, vol. 11, no. 5, pp. 1062–1176, 2018, doi: 10.1039/c7ee02342a.
[49] K. Kelektsoglou, "Carbon capture and storage: A review of mineral storage of CO2 in Greece," *Sustainability (Switzerland)*, vol. 10, no. 12, 2018, doi: 10.3390/su10124400.
[50] T. Shimizu, T. Hirama, H. Hosoda, K. Kitano, M. Inagaki, and K. Tejima, "A twin fluid-bed reactor for removal of CO2 from combustion processes," *Chemical Engineering Research and Design*, vol. 77, no. 1, pp. 62–68, 1999, doi: 10.1205/026387699525882.
[51] R. Ramezani, S. Mazinani, and R. Di Felice, *Characterization and kinetics of CO2 absorption in potassium carbonate solution promoted by 2-methylpiperazine*, vol. 6, no. 2. Elsevier B.V., 2018. doi: 10.1016/j.jece.2018.05.019.
[52] M. House and P. Brownsort, "Scottish Carbon Capture & Storage Ship transport of CO 2 for Enhanced Oil Recovery – Literature Survey," vol. 44, no. January, 2015, [Online]. Available: www.sccs.org.uk

[53] N. Dewangan *et al.*, “Recent progress on layered double hydroxide (LDH) derived metal-based catalysts for CO2 conversion to valuable chemicals,” *Catal Today*, vol. 356, pp. 490–513, Oct. 2020, doi: 10.1016/j.cattod.2020.06.020.
[54] K. Świrk, J. Grams, M. Motak, P. Da Costa, and T. Grzybek, “Understanding of tri-reforming of methane over Ni/Mg/Al hydrotalcite-derived catalyst for CO2utilization from flue gases from natural gas-fired power plants,” *Journal of CO2 Utilization*, vol. 42, Dec. 2020, doi: 10.1016/j.jcou.2020.101317.
[55] A. Iulianelli, S. Liguori, J. Wilcox, and A. Basile, “Advances on methane steam reforming to produce hydrogen through membrane reactors technology: A review,” *Catal Rev Sci Eng*, vol. 58, no. 1, pp. 1–35, Jan. 2016, doi: 10.1080/01614940.2015.1099882.
[56] D. P. Minh *et al.*, “Hydrogen production from biogas reforming: An overview of steam reforming, dry reforming, dual reforming, and tri-reforming of methane,” in *Hydrogen Supply Chain: Design, Deployment and Operation*, Elsevier, 2018, pp. 111–166. doi: 10.1016/B978-0-12-811197-0.00004-X.
[57] A. P. E. York, T. Xiao, and M. L. H. Green, “Brief overview of the partial oxidation of methane to synthesis gas,” 2003.
[58] E. le Saché and T. R. Reina, “Analysis of Dry Reforming as direct route for gas phase CO2 conversion. The past, the present and future of catalytic DRM technologies,” *Progress in Energy and Combustion Science*, vol. 89. Elsevier Ltd, Mar. 01, 2022. doi: 10.1016/j.pecs.2021.100970.
[59] M. K. Nikoo and N. A. S. Amin, “Thermodynamic analysis of carbon dioxide reforming of methane in view of solid carbon formation,” *Fuel Processing Technology*, vol. 92, no. 3, pp. 678–691, Mar. 2011, doi: 10.1016/j.fuproc.2010.11.027.
[60] S. Arora and R. Prasad, “An overview on dry reforming of methane: Strategies to reduce carbonaceous deactivation of catalysts,” *RSC Advances*, vol. 6, no. 110. Royal Society of Chemistry, pp. 108668–108688, 2016. doi: 10.1039/c6ra20450c.
[61] Y. Kathiraser, U. Oemar, E. T. Saw, Z. Li, and S. Kawi, “Kinetic and mechanistic aspects for CO2 reforming of methane over Ni based catalysts,” *Chemical Engineering Journal*, vol. 278, pp. 62–78, 2015, doi: 10.1016/j.cej.2014.11.143.
[62] M. C. J. Bradford and M. A. Vannice, “CO2 reforming of CH4,” *Catal Rev Sci Eng*, vol. 41, no. 1, pp. 1–42, 1999, doi: 10.1081/CR-100101948.
[63] M. Takht Ravanchi and S. Sahebdelfar, “Carbon dioxide capture and utilization in petrochemical industry: potentials and challenges,” *Appl Petrochem Res*, vol. 4, no. 1, pp. 63–77, May 2014, doi: 10.1007/s13203-014-0050-5.
[64] J. Xu and G. F. Froment, “Methane Steam Reforming, Methanation and Water-Gas Shift: 1. Intrinsic Kinetics,” *AIChE Journal*, vol. 35, no. 1, pp. 88–96, Jan. 1989.
[65] Y. A. Zhu, D. Chen, X. G. Zhou, and W. K. Yuan, “DFT studies of dry reforming of methane on Ni catalyst,” *Catal Today*, vol. 148, no. 3–4, pp. 260–267, Nov. 2009, doi: 10.1016/j.cattod.2009.08.022.
[66] M. C. J. Bradford and M. A. Vannice, “Catalytic reforming of methane with carbon dioxide over nickel catalysts II. Reaction kinetics,” *Appl Catal A Gen*, vol. 142, pp. 97–122, 1996.
[67] T. Osaki, T. Horiuchi, K. Suzuki, and T. Mori, “Suppression of carbon deposition in CO2-reforming of methane on metal sulfide catalysts,” *Catal Letters*, vol. 35, pp. 39–43, 1995.
[68] J. Wei and E. Iglesia, “Isotopic and kinetic assessment of the mechanism of reactions of CH 4 with CO2 or H2O to form synthesis gas and carbon on nickel catalysts,” *J Catal*, vol. 224, no. 2, pp. 370–383, 2004, doi: 10.1016/j.jcat.2004.02.032.
[69] Z. J. Zhao, C. C. Chiu, and J. Gong, “Molecular understandings on the activation of light hydrocarbons over heterogeneous catalysts,” *Chem Sci*, vol. 6, no. 8, pp. 4403–4425, Aug. 2015, doi: 10.1039/c5sc01227a.

[70] P. Djinović, J. Batista, and A. Pintar, “Efficient catalytic abatement of greenhouse gases: Methane reforming with CO2 using a novel and thermally stable Rh-CeO2 catalyst,” *Int J Hydrogen Energy*, vol. 37, no. 3, pp. 2699–2707, 2012, doi: 10.1016/j.ijhydene.2011.10.107.
[71] H. Y. Wang and E. Ruckenstein, “Carbon dioxide reforming of methane to synthesis gas over supported rhodium catalysts: The effect of support,” *Appl Catal A Gen*, vol. 204, no. 1, pp. 143–152, 2000, doi: 10.1016/S0926-860X(00)00547-0.
[72] N. A. K. Aramouni, J. G. Touma, B. A. Tarboush, J. Zeaiter, and M. N. Ahmad, “Catalyst design for dry reforming of methane: Analysis review,” *Renewable and Sustainable Energy Reviews*, vol. 82, no. December 2016, pp. 2570–2585, 2018, doi: 10.1016/j.rser.2017.09.076.
[73] N. Abdel Karim Aramouni, J. Zeaiter, W. Kwapinski, and M. N. Ahmad, “Thermodynamic analysis of methane dry reforming: Effect of the catalyst particle size on carbon formation,” *Energy Convers Manag*, vol. 150, pp. 614–622, 2017, doi: 10.1016/j.enconman.2017.08.056.
[74] J. Zhang, H. Wang, and A. K. Dalai, “Development of stable bimetallic catalysts for carbon dioxide reforming of methane,” *J Catal*, vol. 249, no. 2, pp. 300–310, 2007, doi: 10.1016/j.jcat.2007.05.004.
[75] J. R. Rostrup-Nielsen and J. H. Bak Hansen, “CO2-reforming of methane over transition metals,” *Journal of Catalysis*, vol. 144, no. 1. pp. 38–49, 1993. doi: 10.1006/jcat.1993.1312.
[76] T. P. Beebe, D. W. Goodman, B. D. Kay, and J. T. Yates, “Kinetics of the activated dissociative adsorption of methane on the low index planes of nickel single crystal surfaces,” *J Chem Phys*, vol. 87, no. 4, pp. 2305–2315, 1987, doi: 10.1063/1.453162.
[77] R. Dębek, M. Motak, T. Grzybek, M. E. Galvez, and P. Da Costa, “A short review on the catalytic activity of hydrotalcite-derived materials for dry reforming of methane,” *Catalysts*, vol. 7, no. 1. MDPI, Jan. 18, 2017. doi: 10.3390/catal7010032.
[78] S. Saeedi, X. T. Nguyen, F. Bossola, C. Evangelisti, and V. Dal Santo, “Methane Reforming Processes: Advances on Mono- and Bimetallic Ni-Based Catalysts Supported on Mg-Al Mixed Oxides,” *Catalysts*, vol. 13, no. 2. MDPI, Feb. 01, 2023. doi: 10.3390/catal13020379.
[79] D. Suescum-Morales, J. R. Jiménez, and J. M. Fernández-Rodríguez, “Review of the Application of Hydrotalcite as CO2 Sinks for Climate Change Mitigation,” *ChemEngineering*, vol. 6, no. 4. MDPI, Aug. 01, 2022. doi: 10.3390/chemengineering6040050.
[80] L. K. G. Bhatta, S. Subramanyam, M. D. Chengala, S. Olivera, and K. Venkatesh, “Progress in hydrotalcite like compounds and metal-based oxides for CO2 capture: A review,” *J Clean Prod*, vol. 103, pp. 171–196, 2015, doi: 10.1016/j.jclepro.2014.12.059.
[81] A. I. Tsyganok, T. Tsunoda, S. Hamakawa, K. Suzuki, K. Takehira, and T. Hayakawa, “Dry reforming of methane over catalysts derived from nickel-containing Mg-Al layered double hydroxides,” 2003. [Online]. Available: www.elsevier.com/locate/jcat
[82] R. Kumar and K. K. Pant, “Hydrotalcite-derived Ni-Zn-Mg-Al catalyst for Tri-reforming of methane: Effect of divalent to trivalent metal ratio and Ni loading,” *Fuel Processing Technology*, vol. 210, Dec. 2020, doi: 10.1016/j.fuproc.2020.106559.
[83] R. A. R. Ferreira, C. N. Ávila-Neto, F. B. Noronha, and C. E. Hori, “Study of LPG steam reform using Ni/Mg/Al hydrotalcite-type precursors,” *Int J Hydrogen Energy*, vol. 44, no. 45, pp. 24471–24484, Sep. 2019, doi: 10.1016/j.ijhydene.2019.07.193.
[84] R. Dębek, M. E. Galvez, F. Launay, M. Motak, T. Grzybek, and P. Da Costa, “Low temperature dry methane reforming over Ce, Zr and CeZr promoted Ni–Mg–Al hydrotalcite-derived catalysts,” *Int J Hydrogen Energy*, vol. 41, no. 27, pp. 11616–11623, Jul. 2016, doi: 10.1016/j.ijhydene.2016.02.074.
[85] D. Y. Kalai, K. Stangeland, W. M. Tucho, Y. Jin, and Z. Yu, “Biogas reforming on hydrotalcite-derived Ni-Mg-Al catalysts: The effect of Ni loading and Ce promotion,”

Journal of CO2 Utilization, vol. 33, pp. 189–200, Oct. 2019, doi: 10.1016/j.jcou.2019.05.011.

[86] W. N. Manan, W. N. R. Wan Isahak, and Z. Yaakob, "CeO2-Based Heterogeneous Catalysts in Dry Reforming Methane and Steam Reforming Methane: A Short Review," *Catalysts*, vol. 12, no. 5. MDPI, May 01, 2022. doi: 10.3390/catal12050452.

[87] L. P. Teh, H. D. Setiabudi, S. N. Timmiati, M. A. A. Aziz, N. H. R. Annuar, and N. N. Ruslan, "Recent progress in ceria-based catalysts for the dry reforming of methane: A review," *Chem Eng Sci*, vol. 242, Oct. 2021, doi: 10.1016/j.ces.2021.116606.

[88] H. P. Ren *et al.*, "Insights into CeO2-modified Ni-Mg-Al oxides for pressurized carbon dioxide reforming of methane," *Chemical Engineering Journal*, vol. 259, pp. 581–593, Jan. 2015, doi: 10.1016/j.cej.2014.08.029.

[89] R. Di Monte and J. Kašpar, "Heterogeneous environmental catalysis - A gentle art: CeO 2-ZrO2 mixed oxides as a case history," in *Catalysis Today*, Feb. 2005, pp. 27–35. doi: 10.1016/j.cattod.2004.11.005.

[90] J. Abou Rached *et al.*, "Ni based catalysts promoted with cerium used in the steam reforming of toluene for hydrogen production," *Int J Hydrogen Energy*, vol. 42, no. 17, pp. 12829–12840, Apr. 2017, doi: 10.1016/j.ijhydene.2016.10.053.

[91] R. Dębek, M. Motak, M. E. Galvez, P. Da Costa, and T. Grzybek, "Catalytic activity of hydrotalcite-derived catalysts in the dry reforming of methane: on the effect of Ce promotion and feed gas composition," *Reaction Kinetics, Mechanisms and Catalysis*, vol. 121, no. 1, pp. 185–208, Jun. 2017, doi: 10.1007/s11144-017-1167-1.

[92] F. Rahbar Shamskar, F. Meshkani, and M. Rezaei, "Preparation and characterization of ultrasound-assisted co-precipitated nanocrystalline La-, Ce-, Zr -promoted Ni-Al2O3 catalysts for dry reforming reaction," *Journal of CO2 Utilization*, vol. 22, pp. 124–134, Dec. 2017, doi: 10.1016/j.jcou.2017.09.014.

[93] R. Y. Chein and W. Y. Fung, "Syngas production via dry reforming of methane over CeO2 modified Ni/Al2O3 catalysts," *Int J Hydrogen Energy*, vol. 44, no. 28, pp. 14303–14315, May 2019, doi: 10.1016/j.ijhydene.2019.01.113.

[94] M. Khajenoori, M. Rezaei, and F. Meshkani, "Dry reforming over CeO2-promoted Ni/MgO nano-catalyst: Effect of Ni loading and CH4/CO2 molar ratio," *Journal of Industrial and Engineering Chemistry*, vol. 21, pp. 717–722, Jan. 2015, doi: 10.1016/j.jiec.2014.03.043.

[95] C. E. Daza, J. Gallego, J. A. Moreno, F. Mondragón, S. Moreno, and R. Molina, "CO2 reforming of methane over Ni/Mg/Al/Ce mixed oxides," *Catal Today*, vol. 133–135, no. 1–4, pp. 357–366, 2008, doi: 10.1016/j.cattod.2007.12.081.

[96] C. E. Daza, J. Gallego, F. Mondragón, S. Moreno, and R. Molina, "High stability of Ce-promoted Ni/Mg-Al catalysts derived from hydrotalcites in dry reforming of methane," *Fuel*, vol. 89, no. 3, pp. 592–603, Mar. 2010, doi: 10.1016/j.fuel.2009.10.010.

[97] C. E. Daza, C. R. Cabrera, S. Moreno, and R. Molina, "Syngas production from CO2 reforming of methane using Ce-doped Ni-catalysts obtained from hydrotalcites by reconstruction method," *Appl Catal A Gen*, vol. 378, no. 2, pp. 125–133, Apr. 2010, doi: 10.1016/j.apcata.2010.01.037.

[98] C. E. Daza, S. Moreno, and R. Molina, "Ce - Promoted catalyst from hydrotalcites for CO2 reforming of methane: Calcination temperature effect," *Quim Nova*, vol. 35, no. 7, pp. 1325–1328, 2012, doi: 10.1590/S0100-40422012000700008.

[99] R. Dębek *et al.*, "Ni-containing Ce-promoted hydrotalcite derived materials as catalysts for methane reforming with carbon dioxide at low temperature - On the effect of basicity," *Catal Today*, vol. 257, no. P1, pp. 59–65, Nov. 2015, doi: 10.1016/j.cattod.2015.03.017.

[100] G. A. Tafete and N. G. Habtu, "Reactor configuration, operations and structural catalyst design in process intensification of catalytic reactors: A review," *Chemical Engineering and Processing - Process Intensification*, vol. 184. Elsevier B.V., Feb. 01, 2023. doi: 10.1016/j.cep.2023.109290.

[101] V. Tomašić and F. Jović, “State-of-the-art in the monolithic catalysts/reactors,” *Appl Catal A Gen*, vol. 311, no. 1–2, pp. 112–121, Sep. 2006, doi: 10.1016/j.apcata.2006.06.013.
[102] R. M. Heck, S. Gulati, and R. J. Farrauto, “The application of monoliths for gas phase catalytic reactions,” 2001.
[103] I. Luisetto *et al.*, “Ni supported on γ-Al2O3promoted by Ru for the dry reforming of methane in packed and monolithic reactors,” *Fuel Processing Technology*, vol. 158, pp. 130–140, 2017, doi: 10.1016/j.fuproc.2016.12.015.
[104] F. Agueniou *et al.*, “3D-printing of metallic honeycomb monoliths as a doorway to a new generation of catalytic devices: the Ni-based catalysts in methane dry reforming showcase,” *Catal Commun*, vol. 148, no. October 2020, p. 106181, 2021, doi: 10.1016/j.catcom.2020.106181.
[105] H. Liu *et al.*, “Catalytic performance of novel Ni catalysts supported on SiC monolithic foam in carbon dioxide reforming of methane to synthesis gas,” *Catal Commun*, vol. 9, no. 1, pp. 51–54, 2008, doi: 10.1016/j.catcom.2007.05.002.
[106] J. Chen, H. Yang, N. Wang, Z. Ring, and T. Dabros, “Mathematical modeling of monolith catalysts and reactors for gas phase reactions,” *Applied Catalysis A: General*, vol. 345, no. 1. pp. 1–11, Jul. 31, 2008. doi: 10.1016/j.apcata.2008.04.010.
[107] I. Cornejo, P. Nikrityuk, C. Lange, and R. E. Hayes, “Influence of upstream turbulence on the pressure drop inside a monolith,” *Chemical Engineering and Processing - Process Intensification*, vol. 147, Jan. 2020, doi: 10.1016/j.cep.2019.107735.
[108] M. Tu, R. Ratnakar, and V. Balakotaiah, “Reduced order models with local property dependent transfer coefficients for real time simulations of monolith reactors,” *Chemical Engineering Journal*, vol. 383, Mar. 2020, doi: 10.1016/j.cej.2019.123074.
[109] O. Deutschmann, R. Schwiedernoch, L. I. Maier, and D. Chatterjee, “Natural Gas Conversion in Monolithic Catalysts: Interaction of Chemical Reactions and Transport Phenomena,” *Stud Surf Sci Catal*, pp. 251–258, 2001.
[110] T. A. Nijhuis, A. E. W. Beers, T. Vergunst, I. Hoek, F. Kapteijn, and J. A. Moulijn, “Preparation of monolithic catalysts,” *Catalysis Reviews - Science and Engineering*, vol. 43, no. 4. pp. 345–380, Nov. 2001. doi: 10.1081/CR-120001807.
[111] C. Agrafiotis and A. Tsetsekou, “Effect of processing parameters on the properties of γ-alumina washcoats deposited on ceramic honeycombs,” *J Mater Sci*, vol. 35, no. 4, pp. 951–960, 2000, doi: 10.1023/A:1004762827623.
[112] M. Valentini, G. Groppi, C. Cristiani, M. Levi, E. Tronconi, and P. Forzatti, “The deposition of γ-Al2O3 layers on ceramic and metallic supports for the preparation of structured catalysts,” *Catal Today*, vol. 69, no. 1–4, pp. 307–314, 2001, doi: 10.1016/S0920-5861(01)00383-2.
[113] L. Villegas, F. Masset, and N. Guilhaume, “Wet impregnation of alumina-washcoated monoliths: Effect of the drying procedure on Ni distribution and on autothermal reforming activity,” *Appl Catal A Gen*, vol. 320, pp. 43–55, Mar. 2007, doi: 10.1016/j.apcata.2006.12.011.
[114] A. C. C. Chang and K. Y. Lee, “Biogas reforming by the honeycomb reactor for hydrogen production,” *Int J Hydrogen Energy*, vol. 41, no. 7, pp. 4358–4365, Feb. 2016, doi: 10.1016/j.ijhydene.2015.09.018.
[115] A. Leba and R. Yıldırım, “Determining most effective structural form of nickel-cobalt catalysts for dry reforming of methane,” *Int J Hydrogen Energy*, 2020, doi: 10.1016/j.ijhydene.2019.12.020.
[116] P. Oñativia and R. De Gaona, “Catalysts for the dry reforming of methane and method for the preparation.” pp. 5–10, 2016.
[117] H. L. Huynh and Z. Yu, “CO2 Methanation on Hydrotalcite-Derived Catalysts and Structured Reactors: A Review,” *Energy Technology*, vol. 8, no. 5. Wiley-VCH Verlag, May 01, 2020. doi: 10.1002/ente.201901475.

[118] X. Du, D. Zhang, L. Shi, R. Gao, and J. Zhang, “Coke- and sintering-resistant monolithic catalysts derived from in situ supported hydrotalcite-like films on Al wires for dry reforming of methane,” *Nanoscale*, vol. 5, no. 7, pp. 2659–2663, 2013, doi: 10.1039/c3nr33921a.
[119] F. Agueniou *et al.*, “Ultrathin washcoat and very low loading monolithic catalyst with outstanding activity and stability in dry reforming of methane,” *Nanomaterials*, vol. 10, no. 3, 2020, doi: 10.3390/nano10030445.
[120] M. J. Ledoux and C. Pham-Huu, “Silicon carbide a novel catalyst support for heterogeneous catalysis,” *Cattech*, vol. 5, no. 4, pp. 226–246, 2001, doi: 10.1023/A:1014092930183.
[121] X. Gao *et al.*, “Carbon nanofibers decorated SiC foam monoliths as the support of anti-sintering Ni catalyst for methane dry reforming,” *Int J Hydrogen Energy*, vol. 42, no. 26, pp. 16547–16556, 2017, doi: 10.1016/j.ijhydene.2017.05.164.
[122] O. Daoura *et al.*, “One-pot prepared mesoporous silica SBA-15-like monoliths with embedded Ni particles as selective and stable catalysts for methane dry reforming,” *Appl Catal B*, vol. 280, no. May 2020, p. 119417, 2021, doi: 10.1016/j.apcatb.2020.119417.
[123] E. Soghrati, M. Kazemeini, A. M. Rashidi, and K. Jafari Jozani, “Preparation and characterization of Co-Mo catalyst supported on CNT coated cordierite monoliths utilized for naphta HDS process,” *Procedia Eng*, vol. 42, no. August, pp. 1484–1492, 2012, doi: 10.1016/j.proeng.2012.07.541.
[124] F. Agueniou *et al.*, “Supplementary Materials: Ultrathin washcoat and very low loading monolithic catalyst with outstanding activity and stability in dry reforming of methane,” *Nanomaterials*, vol. 10, no. 3, 2020, doi: 10.3390/nano10030445.
[125] S. O. Soloviev, A. Y. Kapran, S. N. Orlyk, and E. V. Gubareni, “Carbon dioxide reforming of methane on monolithic Ni/Al2O 3-based catalysts,” *Journal of Natural Gas Chemistry*, vol. 20, no. 2, pp. 184–190, Mar. 2011, doi: 10.1016/S1003-9953(10)60149-1.
[126] P. Pornruangsakun, S. Tungkamani, T. Ratana, M. Phongaksorn, and T. Sornchamni, “Investigation of Coke Formation in Dry Methane Reforming over Nickel-based Monolithic Catalysts,” *The International Journal of Advanced Culture Technology*, vol. 3, no. 1, pp. 31–38, Jun. 2015, doi: 10.17703/ijact.2015.3.1.31.
[127] F. Agueniou *et al.*, “Honeycomb monolithic design to enhance the performance of Ni-based catalysts for dry reforming of methane,” *Catal Today*, 2020, doi: 10.1016/j.cattod.2020.07.030.
[128] R. Chava, D. Purbia, B. Roy, V. M. Janardhanan, A. Bahurudeen, and S. Appari, “Effect of Calcination Time on the Catalytic Activity of Ni/γ-Al2O3 Cordierite Monolith for Dry Reforming of Biogas,” *Int J Hydrogen Energy*, vol. 46, no. 9, pp. 6341–6357, Feb. 2021, doi: 10.1016/j.ijhydene.2020.11.125.
[129] R. Chava, A. V. D. Bhaskar, B. Roy, and S. Appari, “Reforming of model biogas using Ni/CeO2/γ-Al2O3 monolith catalyst,” *Mater Today Proc*, vol. 72, pp. 134–139, Jan. 2023, doi: 10.1016/j.matpr.2022.06.234.
[130] C. Wang, T. Wang, L. Ma, Y. Gao, and C. Wu, “Steam reforming of biomass raw fuel gas over NiO-MgO solid solution cordierite monolith catalyst,” *Energy Convers Manag*, vol. 51, no. 3, pp. 446–451, Mar. 2010, doi: 10.1016/j.enconman.2009.10.006.
[131] A. Vita, C. Italiano, M. A. Ashraf, L. Pino, and S. Specchia, “Syngas production by steam and oxy-steam reforming of biogas on monolith-supported CeO2-based catalysts,” *Int J Hydrogen Energy*, vol. 43, no. 26, pp. 11731–11744, Jun. 2018, doi: 10.1016/j.ijhydene.2017.11.140.
[132] Y. Zhu *et al.*, “Optimization of the washcoat slurry for hydrotalcite-based lnt catalyst,” *Catalysts*, vol. 9, no. 8, Aug. 2019, doi: 10.3390/CATAL9080696.
[133] C. Daza, A. Kiennemann, S. Moreno, and R. Molina, “Stability of Ni-Ce catalysts supported over Al-PVA modified mineral clay in dry reforming of methane,” *Energy and Fuels*, vol. 23, no. 7, pp. 3497–3509, 2009, doi: 10.1021/ef9000874.
[134] S. S. Miri, F. Meshkani, A. Rastegarpanah, and M. Rezaei, “Influence of Fe, La, Zr, Ce, and Ca on the catalytic performance and coke formation in dry reforming of methane over

Ni/MgO.Al2O3 catalyst," *Chem Eng Sci*, vol. 250, Mar. 2022, doi: 10.1016/j.ces.2021.116956.
[135] S. Yu, Y. Hu, H. Cui, Z. Cheng, and Z. Zhou, "Ni-based catalysts supported on MgAl2O4 with different properties for combined steam and CO2 reforming of methane," *Chem Eng Sci*, vol. 232, Mar. 2021, doi: 10.1016/j.ces.2020.116379.
[136] F. Meng, Z. Li, J. Liu, X. Cui, and H. Zheng, "Effect of promoter Ce on the structure and catalytic performance of Ni/Al2O3 catalyst for CO methanation in slurry-bed reactor," *J Nat Gas Sci Eng*, vol. 23, pp. 250–258, Mar. 2015, doi: 10.1016/j.jngse.2015.01.041.
[137] Z. Alipour, M. Rezaei, and F. Meshkani, "Effect of Ni loadings on the activity and coke formation of MgO-modified Ni/Al2O3 nanocatalyst in dry reforming of methane," *Journal of Energy Chemistry*, vol. 23, no. 5, pp. 633–638, 2014, doi: 10.1016/S2095-4956(14)60194-7.
[138] M. Boaro, S. Colussi, and A. Trovarelli, "Ceria-based materials in hydrogenation and reforming reactions for CO 2 valorization," *Frontiers in Chemistry*, vol. 7. Frontiers Media S.A., Feb. 01, 2019. doi: 10.3389/fchem.2019.00028.
[139] L. P. Matte *et al.*, "Influence of the CeO2 Support on the Reduction Properties of Cu/CeO2 and Ni/CeO2 Nanoparticles," *Journal of Physical Chemistry C*, vol. 119, no. 47, pp. 26459–26470, Nov. 2015, doi: 10.1021/acs.jpcc.5b07654.
[140] J. I. Di Cosimo, V. K. Díez, M. Xu, E. Iglesia, and C. R. Apesteguía, "Structure and Surface and Catalytic Properties of Mg-Al Basic Oxides," 1998.
[141] A. Cárdenas-Arenas *et al.*, "Isotopic and in situ DRIFTS study of the CO2 methanation mechanism using Ni/CeO2 and Ni/Al2O3 catalysts," *Appl Catal B*, vol. 265, May 2020, doi: 10.1016/j.apcatb.2019.118538.
[142] Z. Yu, D. Chen, M. Rønning, T. Vrålstad, E. Ochoa-Fernández, and A. Holmen, "Large-scale synthesis of carbon nanofibers on Ni-Fe-Al hydrotalcite derived catalysts. I. Preparation and characterization of the Ni-Fe-Al hydrotalcites and their derived catalysts," *Appl Catal A Gen*, vol. 338, no. 1–2, pp. 136–146, Apr. 2008, doi: 10.1016/j.apcata.2008.01.003.
[143] C. Lv, H. Chen, M. Hu, T. Ai, and H. Fu, "Nano-oxides washcoat for enhanced catalytic oxidation activity toward the perovskite-based monolithic catalyst," *Environmental Science and Pollution Research*, vol. 28, no. 28, pp. 37142–37157, Jul. 2021, doi: 10.1007/s11356-021-13354-2.
[144] S. L. Kharatyan, H. A. Chatilyan, and K. V Manukyan, "Kinetics and Mechanism of Nickel Oxide Reduction by Methane," *J Phys Chem*, vol. 123, pp. 21513–21521, 2019, doi: https://doi.org/10.1021/acs.jpcc.9b04506.
[145] C. Jensen and M. S. Duyar, "Thermodynamic Analysis of Dry Reforming of Methane for Valorization of Landfill Gas and Natural Gas," *Energy Technology*, vol. 9, no. 7, Jul. 2021, doi: 10.1002/ente.202100106.
[146] R. Dębek, M. Motak, M. E. Galvez, T. Grzybek, and P. Da Costa, "Influence of Ce/Zr molar ratio on catalytic performance of hydrotalcite-derived catalysts at low temperature CO2 methane reforming," *Int J Hydrogen Energy*, vol. 42, no. 37, pp. 23556–23567, Sep. 2017, doi: 10.1016/j.ijhydene.2016.12.121.
[147] X. Feng, J. Feng, and W. Li, "Insight into MgO promoter with low concentration for the carbon-deposition resistance of Ni-based catalysts in the CO2 reforming of CH4," *Cuihua Xuebao/Chinese Journal of Catalysis*, vol. 39, no. 1, pp. 88–98, Jan. 2018, doi: 10.1016/S1872-2067(17)62928-0.
[148] J. Ashok and S. Kawi, "Steam reforming of toluene as a biomass tar model compound over CeO 2 promoted Ni/CaOeAl2O3 catalytic systems," *Int J Hydrogen Energy*, vol. 38, no. 32, pp. 13938–13949, Oct. 2013, doi: 10.1016/j.ijhydene.2013.08.029.

[149] S. Katheria, G. Deo, and D. Kunzru, “Washcoating of Ni/MgAl2O4 Catalyst on FeCralloy Monoliths for Steam Reforming of Methane,” *Energy and Fuels*, vol. 31, no. 3, pp. 3143–3153, Mar. 2017, doi: 10.1021/acs.energyfuels.6b03423.
[150] D. Ugues, S. Specchia, and G. Saracco, “Optimal Microstructural Design of a Catalytic Premixed FeCrAlloy Fiber Burner for Methane Combustion,” *Ind Eng Chem Res*, vol. 43, no. 9, pp. 1990–1998, Apr. 2004, doi: 10.1021/ie034202q.
[151] N. de Miguel, J. Manzanedo, J. Thormann, P. Pfeifer, and P. L. Arias, “Ni catalyst coating on Fecralloy ® Microchanneled foils and testing for Methane steam reforming,” *Chem Eng Technol*, vol. 33, no. 1, pp. 155–166, Jan. 2010, doi: 10.1002/ceat.200900439.
[152] Z. Ma, P. Perreault, D. C. Pelegrin, D. C. Boffito, and G. S. Patience, “Thermodynamically unconstrained forced concentration cycling of methane catalytic partial oxidation over CeO2 FeCralloy catalysts,” *Chemical Engineering Journal*, vol. 380, Jan. 2020, doi: 10.1016/j.cej.2019.122470.
[153] V. N. Rogozhnikov *et al.*, “Structured composite catalyst Pd/Ce0.75Zr0.25O2-x/θ-Al2O3/FeCrAlloy for complete oxidation of methane,” *Mater Lett*, vol. 310, Mar. 2022, doi: 10.1016/j.matlet.2021.131481.
[154] C. Y. Chou, J. A. Loiland, and R. F. Lobo, “Reverse water-gas shift iron catalyst derived from magnetite,” *Catalysts*, vol. 9, no. 9, Sep. 2019, doi: 10.3390/catal9090773.
[155] M. Jafarbegloo, A. Tarlani, A. W. Mesbah, and S. Sahebdelfar, “Thermodynamic analysis of carbon dioxide reforming of methane and its practical relevance,” *Int J Hydrogen Energy*, vol. 40, no. 6, pp. 2445–2451, Feb. 2015, doi: 10.1016/j.ijhydene.2014.12.103.

SUPPLEMENTARY INFORMATION

Table 1S. Detailed gas-chromatography methodology for CO_2-methanation reactants and products measurements.

Equipment	Agilent 7890A gas chromatograph
Columns	HP-Plot-U (bonded, divinylbenzene/ethylene glycol dimethacrylate coated onto a fused silica capillary) HP-Plot-Molesieve (fused silica).
Carrier	High purity N_2
Flow	15 mL.min^{-1} (11.15 psi) HP-Plot-U 13.81 mL.mi^{-1} (11.15 psi) HP-Plot-Molesieve.
Temperature program	FID: 30 °C-300 °C, 10°C.min^{-1}, H_2 40 mL.min^{-1}, air 400 mL-min^{-1} TCD: 30 °C-300 °C, 10°C.min^{-1}, He: 6mL. min^{-1}
Total program	30 min

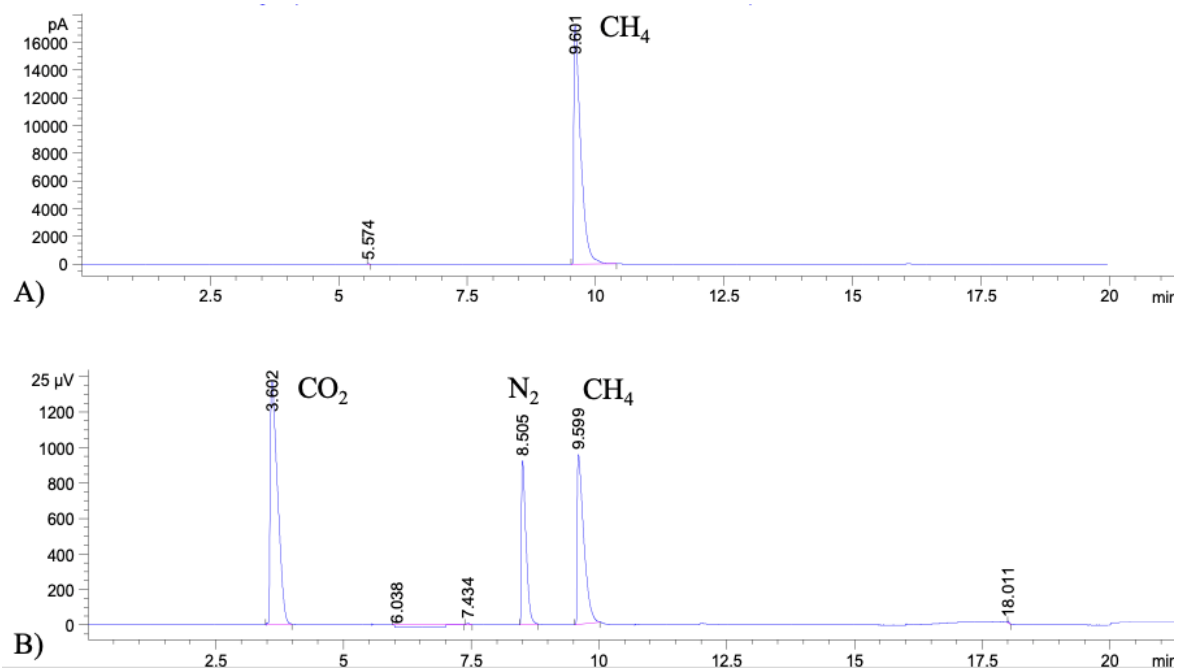

Fig. 1S. Selected chromatograms showed as examples of the reactants and products in bypass process. A) FID, B) TCD.

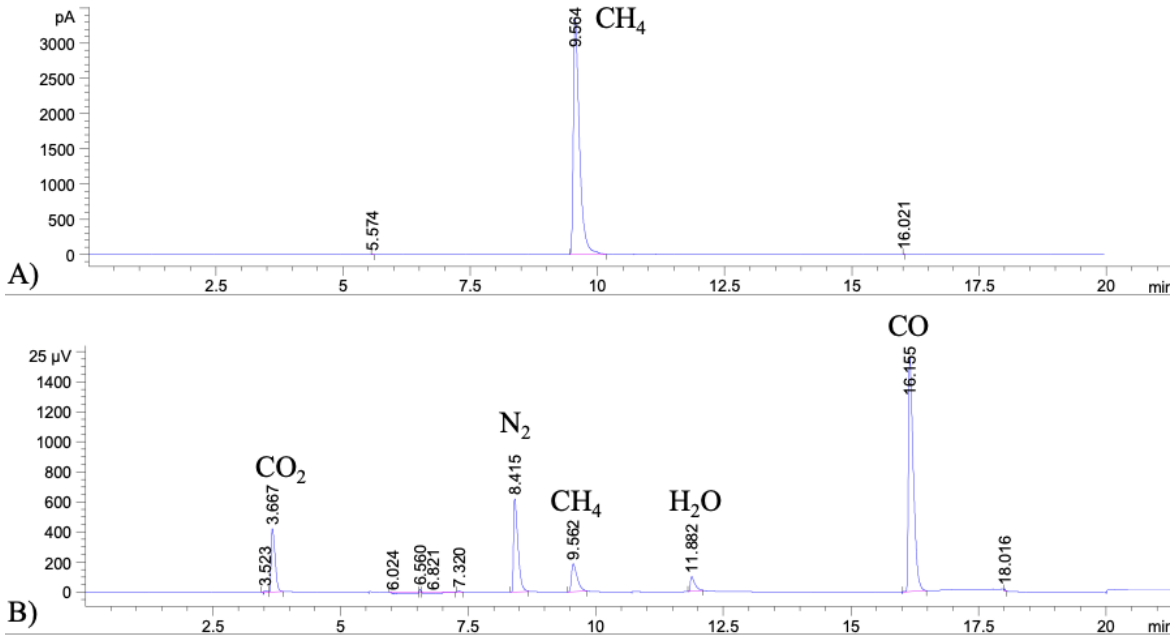

Fig. 2S. Selected chromatograms showed as examples of the reactants and products in DRM. A) FID, B) TCD.

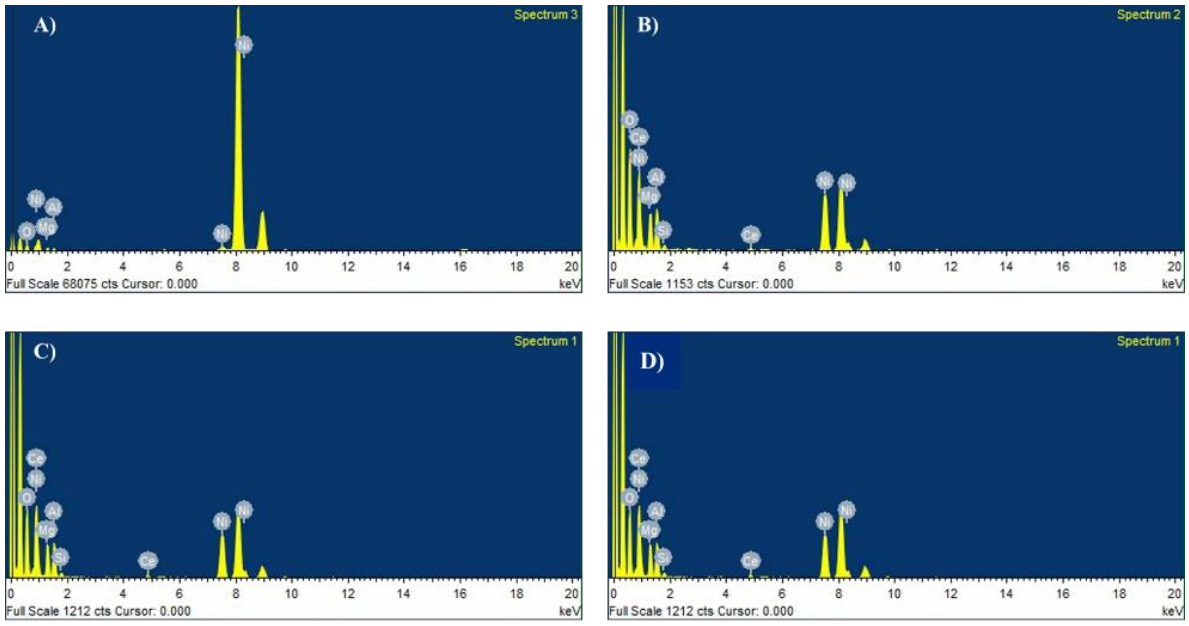

Fig. 3S. EDX of the mixed oxides A) MO1, B) MO2, C) MO3 and D) MO4.

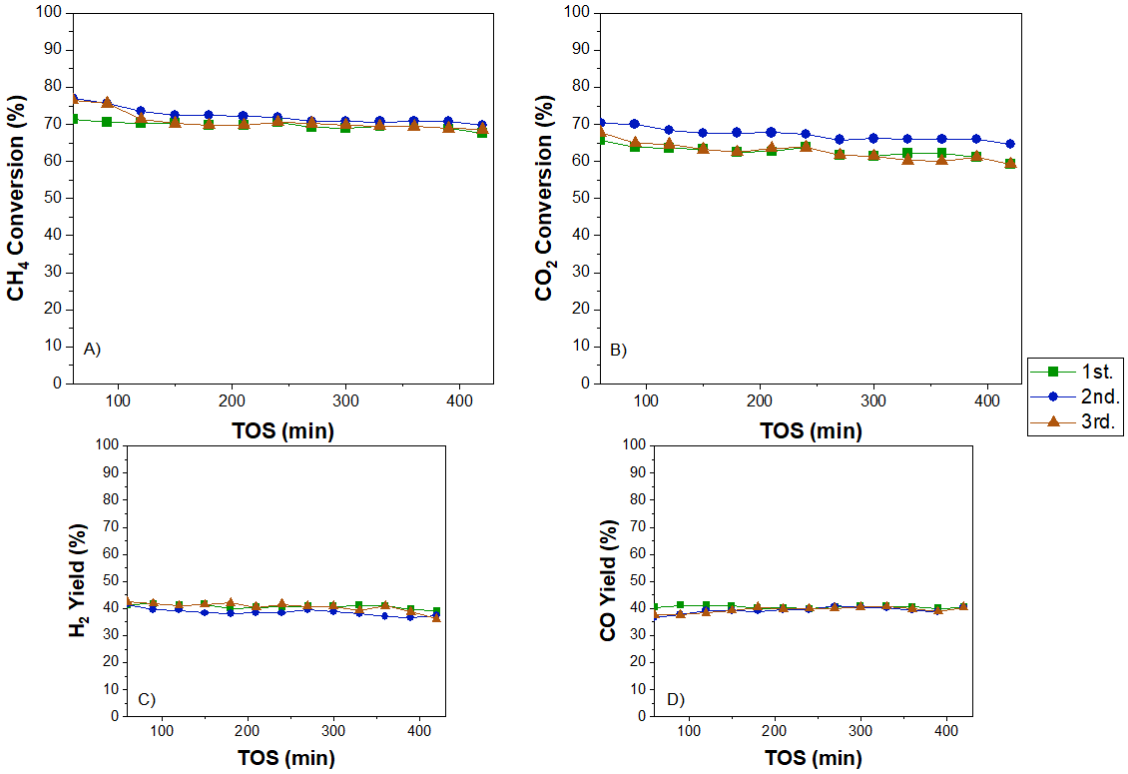

Fig. 4S. Catalytic A) CH_4, B) CO_2 conversion; catalytic C) H_2, and D) CO selectivity vs. time on stream. For MO4 powder catalysts, with no previous reduction. Reaction conditions: 700ºC-8h, 94680 $mL \cdot gCat^{-1} \cdot h_{rxn}^{-1}$. Example of triplicate.

Table 2S. Catalytic test results for the synthesized materials. [a] reaction at 700ºC-8h, [b] reaction at 600ºC-8h, CH_4/CO_2.

MATERIAL	CONVERSION (%)				YIELD (%)				H_2/CO RATIO	
	CH_4		CO_2		H_2		CO		1h of reaction	8h of reaction
	$1h_{rxn}$	$8h_{rxn}$	$1h_{rxn}$	$8h_{rxn}$	$1h_{rxn}$	$8h_{rxn}$	$1h_{rxn}$	$8h_{rxn}$		
POWDER 94680 mL·gCat^{-1}·h$_{rxn}^{-1}$										
MO1 [a]	77.5	74.5	71.8	69.0	44.5	36.9	36.5	34.2	1.2	1.0
MO2 [a]	85.4	76.8	77.0	71.3	49.6	41.6	33.2	36.9	1.5	1.1
MO3 [a]	76.9	69.7	70.2	64.7	41.6	37.5	36.7	40.5	1.1	0.9
MO4 [a]	72.9	68.8	72.4	68.4	41.3	39.9	40.3	41.5	1.0	0.9
MO1$_r$ [b]	62.8	-	22.8	-	64.5	-	36.4	-	1.7	-
MO2$_r$ [b]	66.0	-	38.2	-	48.7	-	30.9	-	1.5	-
MO3$_r$ [b]	70.9	-	47.5	-	46.7	-	30.3	-	1.5	-
MO4$_r$ [b]	67.7	-	46.3	-	47.1	-	34.7	-	1.3	-
IMMOBILIZED MIXED OXIDES 94680 mL·gCat^{-1}·h$_{rxn}^{-1}$										
1SMO1 [a]	86.8	85.0	90.1	87.9	27.2	27.7	22.7	22.2	1.2	1.2
1SMO2 [a]	84.1	85.3	78.2	81.6	28.1	27.7	22.2	22.3	1.2	1.2
1SMO3 [a]	86.9	88.2	81.9	85.7	27.4	26.6	21.8	21.7	1.2	1.2
1SMO4 [a]	86.7	86.2	81.9	83.2	27.7	26.9	21.6	21.8	1.2	1.2
1SMO2u [a]	86.1	85.8	81.6	81.3	27.9	27.7	22.9	22.3	1.2	1.2
1SMO3u [a]	85.7	84.6	78.7	79.9	27.8	26.5	21.3	21.8	1.2	1.2
1SMO4u [a]	85.7	88.0	79.8	86.1	28.2	27.4	22.0	21.6	1.2	1.2
IMMOBILIZED MIXED OXIDES 23679 mL·gCat^{-1}·h$_{rxn}^{-1}$										
4SMO1 [a]	88.3	89.4	80.8	85.4	43.2	42.0	30.7	31.0	1.4	1.3
4SMO2 [a]	82.5	85.1	75.9	79.5	45.0	41.5	31.0	29.7	1.1	1.2
4SMO3 [a]	88.8	89.5	72.1	80.5	46.6	43.1	29.2	30.3	1.6	1.4
4SMO4 [a]	89.2	90.0	82.4	80.7	48.3	46.5	31.2	30.1	1.5	1.5
4SMO1$_r$ [b]	72.0	-	39.0	-	56.2	-	30.4	-	1.8	-
4SMO2$_r$ [b]	76.1	74.9	34.6	35.1	49.9	48.1	31.1	28.2	1.6	1.7
4SMO3$_r$ [b]	72.2	72.6	33.0	28.1	54.4	55.6	30.6	27.6	1.7	2.0
4SMO4$_r$ [b]	68.1	71.2	25.9	27.5	56.6	55.9	28.5	26.7	1.9	2.0